2016

The Development Of A Miniature Spatial Heterodyne Raman Spectrometer For Applications In Planetary Exploration And Other Extreme Environments

Patrick Doyle Barnett
University of South Carolina

The Development of a Miniature Spatial Heterodyne Raman Spectrometer for Applications in Planetary Exploration and Other Extreme Environments

by

Patrick Doyle Barnett

Bachelor of Science
University of Central Missouri, 2011

Submitted in Partial Fulfillment of the Requirements

For the Degree of Doctor of Philosophy in

Chemistry

College of Arts and Sciences

University of South Carolina

2016

Accepted by:

S. Michael Angel, Major Professor

John L. Ferry, Committee Chair

Michael L. Myrick, Committee Member

Alan W. Decho, Committee Member

Cheryl L. Addy, Vice Provost and Dean of the Graduate School

ACKNOWLEDGEMENTS

There are many to whom I owe much for helping me achieve this milestone in my career. First, I would like to thank my committee members: Dr. Ferry, Dr. Myrick, and Dr. Decho for all their time spent reading my work and enduring my presentations, and for constantly challenging me to think about scientific problems differently. I would like to thank my undergraduate research advisors, Dr. Scott McKay and Dr. Gija Geme, for providing me with my first research experience and without whom I might not have decided to pursue my doctorate. I would also like to thank my fellow lab members: Dr. Nirmal Lamsal, for always helping me figure out what was going wrong with my spectrometer; Dr. Joe Bonvallet, for teaching me most of what I know about LIBS; Dr. Alicia Strange for being a constant sounding board for Raman and SHS-related problems; and Ashley Allen for stepping up to fill gaps left by back-to-back graduations of senior lab members.

I could not have reached this point in my career without the constant love and support of my parents, John and Nancy Barnett. They urged me from a young age to question everything, and instilled a love of learning. They have always encouraged me to pursue the field of study that I love, even when that pursuit took me half a continent away from them.

Finally, I would like to thank my advisor, Dr. Angel. The lessons I have learned in my time with Dr. Angel are far too many to ever possibly enumerate. There have been so many times in these few years that he has said something completely off the cuff that

has entirely changed the way I think about something. I have become spoiled having an advisor who is always willing to sit down and talk about any scientific idea, even if it's completely unrelated to our work, simply because the idea is cool. So thank you for enduring my somewhat contrarian nature, for constantly teach me things, even when you weren't trying to teach me something, and for always encouraging me to pursue research avenues that interest me most.

ABSTRACT

Space exploration is arguably one of the most important endeavors our species has ever undertaken. Rapid advances in rocketry and robotics in recent years has allowed for positioning of complex scientific instruments on other planets with a precision that was previously thought impossible. This, along with the need for more sophisticated chemical measurements to achieve the goals of new, more ambitious missions and recent advances in in-situ and remote spectroscopic techniques, has led to a boom in the use of spectroscopic instruments for space exploration. However, future missions to the moons of Jupiter and Saturn, along with other planetary bodies of interest, will require even more sophisticated spectrometers that are smaller, lighter, more energy efficient, and more robust. This work describes the development of one such spectrometer that has the potential to meets these needs, a miniature spatial heterodyne Raman spectrometer (SHRS). The SHRS is capable of high spectral resolution, large spectral range, very high light throughput (~ 200x larger than conventional spectrometers), and is capable of being miniaturized to the millimeter scale, orders of magnitude smaller than conventional Raman spectrometers. The ultimate goal of this project is the development of a millimeter-scale, deep-UV Raman spectrometer for eventual inclusion on a planetary lander. The work described here focuses on the miniaturization of the SHRS, and the optical problems and solutions associated with designing a new spectrometer of such small size while maintaining a performance level that is equivalent to spectrometers orders of magnitude larger.

TABLE OF CONTENTS

LIST OF TABLES

LIST OF FIGURES

CHAPTER 1

INTRODUCTION

1.1 IMPORTANCE OF SPACE EXPLORATION

Space exploration is not only scientifically interesting, but also essential to the continuation of human civilization. Human civilization currently exists in a precarious position. Global-scale extinction events have occurred several times in the history of the Earth and we are not free of this danger. Asteroid impacts, supervolcanos, pandemics, nuclear or biological warfare, near-Earth supernova resulting in a gamma-ray burst directed at Earth, and the eventual increase in solar luminosity are just a few examples of possible events that could wipe out human civilization. Statistically, a global-scale extinction event will eventually take place on Earth again, it's just a matter of time. Surveys of academic experts on various global catastrophic risks estimate 10-20% chance of a global-scale catastrophic event occurring within this century.[1,2] Although there are some catastrophic events that could potentially be overcome technologically (e.g., diverting the path of an asteroid to avoid impact), most potential events are outside the scope of current technology. Astronomer and astrophysicist Carl Sagan famously said, "All civilization become either space-faring or extinct." Human populations existing on only one planet means that our civilization can be completely wiped out by a global catastrophic event. Colonization of other celestial bodies would add redundancy to the existential future of human civilization, ensuring continuation even in the case of a global catastrophe on Earth

Reducing existential risk to human civilization is not the only non-research reason to push further space exploration. Resources on Earth are finite and will eventually be exhausted, especially as more rare elements (e.g., gold, platinum, tellurium, neodymium) are becoming more commonly used in technological development. However, resources for space-faring civilizations are essentially unlimited. Consider platinum as an example: annual supply of platinum from mining and recycling is ~ 200 metric tons.[3] Platinum content in LL Chondrites, a class of near-Earth asteroids of which several hundred have been identified, has been estimated to be as high as 43,000 metric tons for a 1 km diameter asteroid, a relatively small asteroid.[4]

1.2 SPACE EXPLORATION EFFORTS

Human excursion into space beyond low-Earth orbit has not occurred since the last lunar landing in 1972. Space exploration is a costly endeavor, which is made even more costly by inclusion of human astronauts. The potential for loss of human life requires stringent safety protocols and extensive testing for every mission. Life support systems, food, water, waste management, radiation protection, and return fuel increase complexity and cost of missions. Scientific instrumentation on robotic landers has helped compensate for the lack of *in situ* observations and sample collection by human explorers. While it is still important that human explorers investigate celestial bodies when possible, the vastly cheaper and less complex robotic lander/rover missions can identify the best locations to place human scientists for further investigation.

Satellites have orbited or performed fly-bys of all planets and most large moons in the solar system. While the images taken and measurements performed has vastly increased our understanding of our neighbors in the solar system, we have only begun to

scratch the surface of what can be learned. Currently, the most advanced planetary exploration satellite in operation is NASA's Mars Reconnaissance Orbiter (MRO). The MRO is capable of various types of high-resolution imaging, near-IR imaging to obtain mineralogical information about surface features, UV imaging for climate tracking, visible and IR spectrometers to find residues of minerals that form in the presence of water, an instrument for temperature, humidity, and dust content depth profiling of the Martian atmosphere, Radar designed to detect sub-surface solid or liquid water, and radio communications Doppler shift monitoring to study the gravitation field of Mars.[5,6,7,8]

However, even with such advanced data collection capabilities, there is a limit to how much information can be obtained from orbit, making surface-based missions necessary. Surface missions to other planets began in the mid-1970's during the space race between USSR and USA. Landers were sent to Venus on various missions by both countries with suites of instruments including, but not limited to, UV, visible, and IR photometers and spectrometers, nephelometers, mass spectrometers, gamma-ray spectrometers, gas chromatographs, x-ray fluorescence spectrometers, anemometer, penetrometers, and hydrometers.[9] During the same period both countries sent landers to Mars with many of the same instruments that were used on Venus. The data obtained in these missions lead to an explosion of new information about the planets, however, the decline of the USSR and wind-down of the Cold War lead to a period of stagnation in surface-based planetary exploration.

The late 1990's began a new wave of surface-based planetary exploration with NASA's Sojourner rover, the first successful Mars rover. Sojourner carried a variety of cameras and an alpha proton x-ray spectrometer (APXS) for determination of

composition of mineral samples.[10] The success of Sojourner was followed by NASA's twin Mars rovers Spirit and Opportunity in 2004, each weighing in at 16x the dry mass of Sojourner. The rovers carried a variety of cameras, miniature thermal emission spectrometers, Mössbauer spectrometer, APXS, microscopic imager, and a rock abrasion tool to investigate sub-surface samples.[11] The rovers were planned to operate for 90 sols (solar days) but Spirit remained operational for 2623 sols while Opportunity is still operation at over 4500 sols at the time of writing.[11,12] The twin rovers were followed in 2012 by Curiosity, 5x the mass and a large increase in the scientific payload. Curiosity carries a variety of cameras, a standoff laser-induced breakdown spectrometer (LIBS) capable of elemental analysis up to 7 m away, APXS, microscopic imager, x-ray powder diffraction (XRD) spectrometer, x-ray fluorescence (XRF) spectrometer, quadrupole mass-spectrometer, gas chromatograph, tunable laser spectrometer, and dynamic albedo of neutrons instrument to detect hydrogen or liquid and solid water.[13] Curiosity not only set a new standard for complexity of scientific payload but also demonstrated for the first time that a 900 kg, car-sized rover could be set down gently on the surface of another planet. Previous planetary landers involved a much harder landing, slowed by parachutes to a few m/s before impact, requiring the payload to be very rugged and often resulting in damage to sensitive instruments. Curiosity, due to its size and mass, was lowered gently to the ground to a very specific, predefined landing spot from a retro-rocket-suspended sky-crane in a fully automated process. The gentle touchdown and high-precision landing of Curiosity has demonstrated that it is possible to precisely position highly complex scientific instruments on other planets which has further increased interest in *in situ* scientific exploration of other celestial bodies within our solar system.

1.3 OPTICAL SPECTROSCOPY IN PLANETARY EXPLORATION

Optical spectroscopy is a relative new-comer to *in situ* planetary exploration, even though there are features shared across many types of spectroscopy that are useful for the goals of planetary exploration. Spectroscopy can provide elemental and/or structural chemical information and even map the locations of chemical components in a sample. In general, spectroscopy is fast, nondestructive, often does not require contact with the sample or sample preparation in a relatively small package size with low power consumption. The ChemCam of the Curiosity rover is a good example of the benefits of the application of spectroscopy to *in situ* planetary exploration. The ChemCam is a standoff LIBS spectrometer capable of determining the elemental composition of samples up to 7 m from the rover in ambient light conditions, mounted on a mast capable of 360° of rotation, allowing samples to be investigated regardless of the direction the rover is pointed. The ChemCam interrogates a sample area of a few hundred micrometers in size at a repetition rate of 1-10 Hz, allowing for rapid profiling of the elemental composition of a sample in an essentially non-destructive manner (only picograms to nanograms of material is removed per shot).[14]

1.4 RAMAN SPECTROSCOPY IN PLANETARY EXPLORATION

Raman spectroscopy has not yet been used in a planetary exploration mission but would be a useful addition and provide complimentary chemical information. Raman spectroscopy is a vibrational technique and provides structural chemical information. Rama spectroscopy requires no sample preparation, no sample contact and can be used in a standoff configuration, nondestructive, capable of providing qualitative and quantitative chemical identification, fast, capable of identifying minerals, water, ice, and biomarkers

with the same instrument, relatively small package size and low power consumption, capable of measurements in ambient light conditions, and capable of mapping location of chemicals in a sample.[15] Some other techniques that have been used for mineralogical analysis in planetary exploration such as thermal emission spectroscopy and near-IR reflectance spectroscopy produce spectra with broad spectral features that can easily overlap, introducing ambiguity in sample identification.[16] Raman, however, produces spectra with sharp narrow spectral features that are well separated, providing sample identification with less ambiguity.[15] Polycyclic aromatic hydrocarbons (PAHs), which permeate the solar system on planets, moons, and even comets and have been hypothesized to be essential for the development of simple lifeforms, have been shown be identifiable with Raman spectroscopy.[17] The combination of Raman spectroscopy with microscopy, commonly known as microRaman, has been shown capable of mapping microfossils (generally, fossils < 4 mm) in mineral samples, which may be useful for identifying and studying simple lifeforms on other planets.[18] Furthermore, Raman spectroscopy is complementary to techniques that are currently being used in planetary exploration missions such as LIBS and APXS.[19] As of writing two Raman spectrometers are planned for the next Mars rover in 2020: a standoff Raman spectrometer with a range up to 12 m designed by the group that designed the ChemCam called the SuperCam and a UV Raman microscopic imager called SHERLOC.[20,21]

1.5 THE SPATIAL HETERODYNE RAMAN SPECTROMETER

This work focuses on the development of a miniature spatial heterodyne Raman spectrometer (SHRS) for space exploration. The SHRS is a dispersion-based interferometer which has many features that are beneficial for space exploration

applications: high resolution, large spectral range, wide acceptance angle, and high throughput in a package orders of magnitude smaller than conventional Raman spectrometers.[22] The SHRS can be constructed in a monolithic fashion, in which all optical components are physically connected by spacing prisms and optical adhesive, resulting in a single piece that is impervious to alignment drift or external vibrations, which are typically severe problems with many interferometers.[23] Unlike more conventional dispersive spectrometers, the SHRS does not require small slits or long focal-length optics and thus is capable of a high light throughput with a very small package size. Furthermore, spectral resolution of the SHRS is not strongly tied to the size of the entrance aperture like it is with conventional dispersive spectrometers, allowing for a high resolution and high light throughput at the same time. Finally, the large entrance aperture of the SHRS coupled with the wide field-of-view allow for interrogation of a large swath of sample simultaneously. This feature is particularly useful for deep-UV Raman measurements, in which Raman signal intensity is greatly increased but photodegradation of samples is a strong possibility with a tightly focused laser.[24] The large field-of-view of the SHRS allows for the excitation laser to be defocused to lower irradiance while maintaining radiant flux, thus significantly increasing the amount of Raman scattered light that can be collected by the spectrometer.

1.6 DISSERTATION OUTLINE

Chapter 2 lays the theoretical background for the general spatial heterodyne spectrometer (SHS) design, further explanation of Raman spectroscopy and underlying theory, combination of the general SHS with Raman spectroscopy to form the SHRS, and the theoretical limits for miniaturization of the SHRS.

Chapter 3 describes the methods of recovery of spectral information from the interferograms generated by the SHRS, including a discussion of a method that is not commonly used that can help to improve spectral results with difficult-to-correct optical alignment errors.

Chapter 4 describes the use of a standard cell phone camera as a detector for Raman measurements with a millimeter-scale SHRS. Cell phone cameras, while much higher quality than in the past, still use low-quality optical components, low sensitivity, uncooled array detectors, and high-noise analogue to digital converters. However, cell phone cameras are orders of magnitude smaller than scientific grade array detectors and orders of magnitude lower cost. The high light throughput of the SHRS design can overcome the deficiencies of the cell phone camera and successfully recover Raman spectra of a variety of samples.

Chapter 5 describes the implementation of spatial filtering within the SHRS, using the inherent dispersive nature of the optical components to filter out unwanted background light, improving signal-to-noise of the recovered spectra and opening the potential for measurements in ambient light conditions without the pulsed lasers and gated detectors typically required for Raman measurements in ambient light.

Lastly, Chapter 6 describes the use of a miniature SHRS for measurements of standoff LIBS at distances up to 20 m. The wide field-of-view of the SHRS relaxes the laser-pointing stability requirements for standoff LIBS which usually requires very precise alignment between the laser spot on the sample and the collection telescope. Furthermore, the high throughput of the SHRS allowed acquisition of LIBS spectra at

distances of 20 m with no collection optics, a feat which would be impossible with a conventional, slit-based, dispersive spectrometer.

REFERENCES

(1) N. Bostrom. “Existential Risk Prevention as Global Priority”. Global Policy. 2013. 4(1): 15-31.

(2) A. Sandberg, N. Bostrum. “Global Catastrophic Risks Survey”. 2008. Technical Report #2008-1, Future of Humanity Institute, Oxford University: pp. 1-5.

(3) SFA (Oxford) Platinum Quarterly prepared for World Platinum Investment Council. September 8, 2016. www.platinuminvestment.com/supply-and-demand/platinum-quarterly. Accessed October 22, 2016.

(4) B.R. Blair. “The Role of Near-Earth Asteroids in Long-Term Platinum Supply”. Paper presented at the Second Space Resources Roundtable, Colorado School of Mines, November 8-10, 2000. Boulder, CO.

(5) NASA Jet Propulsion Laboratory Mars Reconnaissance Orbiter website: mars.nasa.gov/mro, Accessed October 22, 2016.

(6) S. Murchie *et al.* “Compact reconnaissance Imaging Spectrometer for Mars (CRISM) on Mars Reconnaissance Orbiter (MRO)”. J. Geophys. Res. 2007. 112(E5): E05S03

(7) M.C. Malin *et al.* “Context Camera Investigation on board the Mars Reconnaissance Orbiter”. J. Geophys. Res. 2007. 112(E5): E05S04

(8) A.S. McEwen *et al.* “Mars Reconnaissance Orbiter’s High Resolution Imaging Science Experiment (HiRISE)”. J. Geophys. Res. 2007. 112(E5): E05S02.

(9) National Space Science Data Center. “Chronology of Venus Exploration”. NASA Goddard Space Center. Available at nssdc.gsfc.nasa.gov/planetary/chronology_venus.html. Accessed October 23, 2016.

(10) NASA Jet Propulsion Laboratory. “Mars Pathfinder / Sojourner Rover”. Available at jpl.nasa.gov/missions/mars-pathfinder-sojourner-rover/. Accessed October 23, 2016.

(11) NASA Jet Propulsion Laboratory. “Mars Exploration Rover – Spirit”. Available at jpl.nasa.gov/missions/mars-exploration-rover-spirit-mer/. Accessed October 23, 2016.

(12) NASA Jet Propulsion Laboratory. “Mars Exploration Rover – Opportunity”. Available at jpl.nasa.gov/missions/mars-exploration-rover-opportunity-mer/. Accessed October 23, 2016.

(13) NASA Jet Propulsion Laboratory. “Mars Science Laboratory Curiosity Rover”. Available at jpl.nasa.gov/missions/mars-science-laboratory-curiosity-rover-msl/. Accessed October 23, 2016.

(14) R.C. Wiens, S. Maurice *et al.* “The ChemCam instrument suite on the Mars Science Laboratory rover *Curiosity:* Remote sensing by laser-induced plasmas”. Geochem. News. 2011. 145.

(15) S.M. Angel, N.R. Gomer, S.K. Sharma, C. McKay. “Remote Raman Spectroscopy for Planetary Exploration: A Review”. Appl. Spectrosc. 2012. 66(2): 137-150.

(16) L.A. Haskin, A. Wang, K.M. Rockow, B.L. Jolliff, R.L. Korotev, K.M. Viskupic. “Raman spectroscopy for mineral identification and quantification for in situ surface analysis: A point count method”. J. Geophys. Res. 1997. 102(E8): 19293-19306.

(17) E. Cloutis, P. Szymanski, D. Applin, D. Goltz. “Identification and discrimination of polycyclic aromatic hydrocarbons using Raman spectroscopy”. Icarus. 2016. 274: 211-230.

(18) N. Ferralis, E.D. Matys, A.H. Knoll, C. Hallmann, R.E. Summons. “Rapid, direct and non-destructive assessment of fossil organic matter via microRaman spectroscopy”. Carbon. 2016. 108: 440-449.

(19) P.J. Gasda, T.E. Acosta-Maeda, P. G. Lucey, A.K. Misra, S.K. Sharma, G.J. Taylor. “Next Generation Laser-Based Standoff Spectroscopy Techniques for Mars Exploration”. Appl. Spectrosc. 2015. 69(2): 173-192.

(20) S.M. Clegg, R.C. Wiens, S. Maurice, O. Gasnault, S.K. Sharma, A.K. Misra, R. Newell, O. Forni, J. Lasue, R.B. Anderson, K.L. Nowak-Lovato, T. Fouchet, S.M. Angel, F. Rull, J.R. Johnson. “Remote Geochemical and Mineralogical Analysis with SuperCam for the Mars 2020 Rover”. 46th Lunar and Planetary Science Conference. The Woodlands, Texas, March 16-20, 2015.

(21) L.W. Beegle, R. Bhartia, L. DeFlores, M. Darrach, R.D. Kidd, W. Abbey, S. Asher, A. Burton, S. Clegg, P.G. Conrad, K. Edgett, B. Ehlmann, F. Langenhorst, M. Fries, W. Hug, K Nealson, J. Popp, P. Sobron, A. Steele, R. Wiens, K. Willifor. “SHERLOC: Scanning Habitable Environments with Raman & Luminescence for Organics & Chemicals, an Investigation for 2020”. 45th Lunar and Planetary Science Conference. The Woodlands, Texas, March 17-21, 2014.

(22) N.R. Gomer, C.M. Gordon, P. Lucey, S.K. Sharma, J.C. Carter, S.M. Angel. “Raman Spectroscopy Using a Spatial Heterodyne Spectrometer: Proof of Concept”. Appl. Spectrosc. 2011. 65(8): 849-857.

(23) J.M. Harlander, F.L. Roesler, J.G. Cardon, C.R. Englert, R.R. Conway. "SHIMMER: a spatial heterodyne spectrometer for remote sensing of Earth's middle atmosphere". Appl. Opt. 2002. 41(7): 1343-1352.

(24) N. Lamsal, S.M. Angel. "Deep-Ultraviolet Raman Measurements Using a Spatial Heterodyne Raman Spectrometere (SHRS)". Appl. Spectrosc. 2015. 69(5): 525-534.

CHAPTER 2

THEORETICAL BACKGROUND

2.1 INTRODUCTION

The spatial heterodyne spectrometer (SHS) has many features that, when combined, provide an interesting package for a variety of spectroscopy applications. The SHS is non-scanning; the entire spectrum is collected simultanesouly with no moving parts. The SHS has a compact size, high resolution, large spectral range, and high light throughput. By comparison, dispersive spectrometers require long focal length optics and very narrow slits to achieve high resolution, thus increasing size and decreasing light throughput. Interferometers, however, do not share this requirement.[1] Unlike some interferometers, the SHS does not require high-precision optics. Fourier transform spectroscopy (FTS) systems such as the Fabry-Perot interferometer require optical flatness of roughly $\lambda/100$ whereas SHS systems require optical flatness of $\lambda/10$ or less.[2] FTS systems such as the Michelson interferometer enjoy a multiplex advantage in which signal-to-noise is increased with respect to other systems because all wavelengths are detected by a single detector. The SHS does not enjoy the full multiplex advantage of the Michelson interferometer because the interferogram is spread across many detector elements. The SHS does gain a partial multiplex advantage over dispersive spectrometers due to photon flux at each detector element being greater than those experienced by dispersive systems, as a result of the high light throughput of the SHS. Dispersive spectrometers are limited in throughput because they require narrow slits to achieve high

resolution. FTS systems do not require narrow slits, and as such, have etendue, typically 200 times greater than that of dispersive spectrometers.[2] The SHS has the same throughput advantage as FTS systems. Because of this higher throughput, interferometers, including the SHS, can achieve sensitivities two orders of magnitude greater than those of conventional dispersive spectrometers.[1] FTS systems, including the SHS, have acceptance angles much greater than those of dispersive spectrometers. The acceptance angle of a basic SHS design is ~ 1°. Acceptance angle can be increased further through the use of field-widening prisms. Field-widening in FTS systems is difficult, requiring complex systems to achieve. Field-widening in the SHS, however, does not change the basic design of the system, other than the addition of field-widening prisms between the beamsplitter and the gratings, which can increase acceptance angle up to 10°.[2] In some FTS systems, such as the Michelson interferometer, the interferogram is collected as a function of time so variation in source intensity can introduce artifacts into the spectrum, known as scintillation noise. However, the SHS is immune to scintillation noise because every spectral element is measured simultaneously.[2] Finally, the SHS can be constructed in a monolithic design which removes the requirement that optical elements of the interferometer be held to arcsecond angular tolerances and sub-wavelength linear tolerances and results in a very rugged spectrometer that is immune to the effects of external vibrations which are problematic for most interferometers.[1]

2.2 THEORY

The earliest description of the spatial heterodyne spectrometer (SHS) was given by Dohi and Suzuki in 1970.[3] The SHS is most easily understood as the familiar Michelson interferometer but the return mirrors are replaced by stationary diffraction

gratings. As shown in Figure 2.1, collimated light enters the system and is diverted to the diffraction gratings by a 50/50 beamsplitter. Light is diffracted by the gratings, inducing a wavelength-specific wavefront tilt. The diffracted light then recombines back through the beamsplitter, resulting in a crossing of the wavefronts from each arm of the interferometer. The crossing of the wavefronts induces a spatial phase shift, which allows interference to occur resulting in the formation of a Fizeau fringe pattern of alternating light and dark fringes. The generalized diffraction grating equation can be simplified to describe the SHS.[2]

$$\frac{m}{d} = 2\sigma_0 \sin\theta_L \qquad \text{Eqn. 2.1}$$

Where *m* is the diffraction order, *1/d* is the diffraction grating groove density, σ_0 is the wavenumber of light which diffracts along the same optical path as the input light, thus satisfying the Littrow condition for the diffraction gratings at the grating tilt, θ_L. The light that satisfies the Littrow condition, σ_0, has no wavefront tilt and thus does not form a fringe pattern. The spatial fringe frequency generated by the SHS is given:

$$f_x = 4(\sigma - \sigma_0)\tan\theta_L \qquad \text{Eqn. 2.2}$$

Where σ is the wavenumber corresponding to any wavelength of light other than the Littrow wavelength. Equation 2.2 shows that the spatial fringe frequency of all wavelengths of light other than the Littrow wavelength are heterodyned about the Littrow wavelength, thus a spatial frequency of zero does not correspond to zero wavenumbers but rather to the Littrow wavenumber, σ_0. Heterodyning of the fringe pattern allows recovery of fringes from a high wavenumber source with a relatively small number of

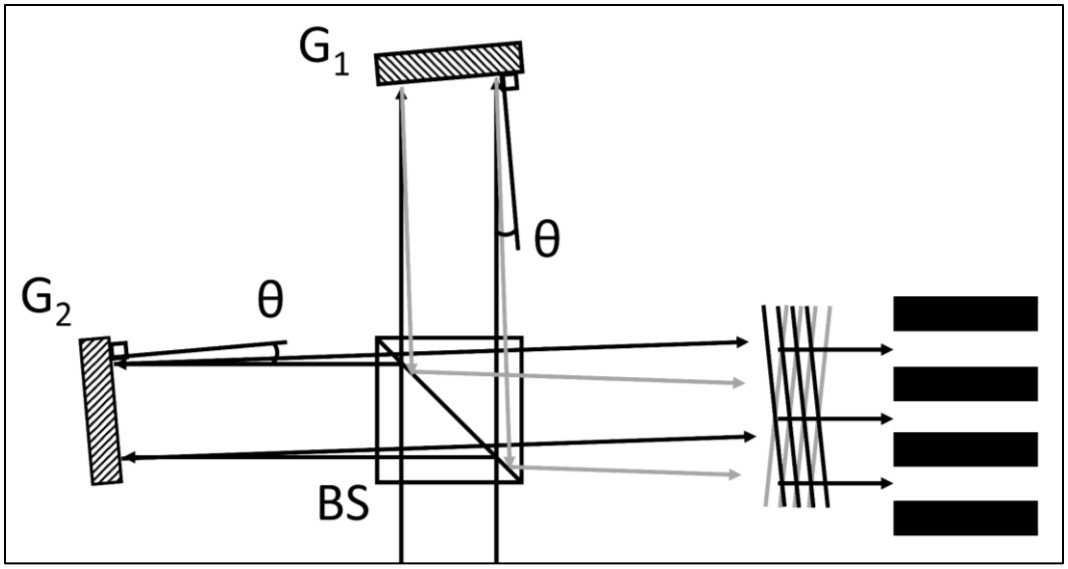

Figure 2.1: Schematic diagram of the basic spatial heterodyne spectrometer design. BS is the cube beamsplitter. G_1 and G_2 are the diffraction gratings. θ is the tilt of the diffraction gratings.

detector elements. The one-dimensional Fizeau fringe pattern formed by the SHS is described by Equation 2.3.[3]

$$I_{(x)} = \int_0^\infty B_{(\sigma)}(1 + \cos(2\pi \cdot 4 \tan\theta_L\,(\sigma - \sigma_0)x))\; d\sigma \qquad \text{Eqn. 2.3}$$

Where $B_{(\sigma)}$ is the input spectrum and x is position along the axis that lies in the dispersion plane of the diffraction gratings, orthogonal to the optical axis. The Fourier transform of $I_{(x)}$ will recover the input spectrum.[2] Essentially, the SHS encodes the path difference scanned by a conventional Fourier transform interferometer on an array detector with no moving parts.[4] The output of the SHS is trasmitted to the detector by high-quality imaging optics which image the plane of the surface of the diffraction gratings onto the detector.[4] The limiting resolving power of the SHS, R_0, at the detector corresponds to the grating resolution limit.[2]

$$R_0 = 4W\sigma_0 \sin\theta_L \qquad \text{Eqn. 2.4}$$

Where W is the width of the gratings. Spectral resolution, $\Delta\sigma$, is a function of wavenumber and related to resolving power.[5]

$$R = \frac{\sigma}{\Delta\sigma} \qquad \text{Eqn. 2.5}$$

The Nyquist criterion requires that sampling frequency be twice that of the highest frequency sampled to avoid aliasing.[6] For an array detector with N detector elements in along the dispersion plane of the diffraction gratings the maximum number of spectral elements that can be recovered without aliasing is $N/2$.[4] Thus, the number of spectral elements recovered is independent of resolution, unlike conventional Fourier transform spectroscopy (FTS) systems in which samples required is typically twice the resolving

power.[4] The collection solid-angle of the SHS is the same as conventional FTS systems.[4,7]

$$\Omega = \frac{2\pi}{R} \qquad \text{Eqn. 2.6}$$

Where Ω_m is the collection solid angle. Etendue, or optical throughput, of a spectrometer is a measure of how much sample light can pass through the system and is strongly related to sensitivity.

$$E = A\Omega \qquad \text{Eqn. 2.7}$$

Where E is etendue of the spectrometer and A is the area of the entrance aperture. Etendue of FTS and SHS systems are typically 200 times that of conventional, slit-based, dispersive spectrometers.[2] This high throughput results in sensitivities that are typically 100 times that of conventional spectrometers.[1] The field-of-view, and thereby etendue, of conventional FTS and SHS systems can be increased by two orders of magnitude through the implementation of field-widening methods within the spectrometer design.[8] Unlike FTS systems, which require complex systems for field-widening, the SHS can be field-widened with no moving parts.[2] The simplest manner in which to field-widen the SHS is to place refractory wedge prisms of the appropriate apex angle between the beamsplitter and gratings.[2] The apex angle of field-widening prisms is chosen such that the image of the gratings is geometrically rotated to appear normal to the optical axis.[2] Field-widening prism apex angle and rotational position are chosen according to Equation 2.8 and Equation 2.9.[4]

$$2(n^2 - 1)\tan\gamma = n^2 \tan\theta_L \qquad \text{Eqn. 2.8}$$

$$n \sin\left(\frac{\alpha}{2}\right) = \sin\gamma \qquad \text{Eqn. 2.9}$$

Where *n* is the refractive index of the prism material, γ is the angle between the prism normal and the optical axis, and α is the apex angle of the prism. There exists an upper limit on the capabilities of field-widening, depending upon the magnitude of the Littrow angle, though this is not before large gains are achieved. Prism spherical abberations limit systems with small Littrow while prism astigmatism limits systems with a large Littrow.[9] The above discussion of field-widening in the SHS assumes that dispersion effects introduced by the prisms is negligible. However, for systems designed with a broad spectral range or systems designed to operate in the ultraviolet spectral region where dispersion is large, achromatic field-widening prisms are required.[4] To achieve this two prisms of different composition and different apex angles are placed in front of the grating with the apex angles pointing in opposite directions.[4]

Investigation of Equation 2.2 shows that spatial fringe frequency is identical for +σ and –σ, which will result in a spectrum which is folded about σ_0, leading to ambiguity determining wavenumbers of spectral features.[4] This can be alleviated by introducing a small vertical tilt to one of the gratings which breaks the symmetry of Equation 2.3, introducing a spatial phase shift along the axis orthogonal to the dispersion plane of the diffraction gratings, resulting in a new intensity function at the detector.[8]

$$I_{(x,y)} = \int_0^\infty B_{(\sigma)}(1 + \cos(2\pi \cdot 4 \tan\theta_L\,(\sigma - \sigma_0)x + 2\alpha\sigma y))\; d\sigma \qquad \text{Eqn. 2.10}$$

Where α is the angle of the vertical grating tilt. As can be seen in Equation 2.10, the vertical tilt of the diffraction grating results in an additional term which corresponds to the spatial frequency in the *y*-axis of the detector. It should be noted that unlike the frequency term corresponding to fringes distributed in the *x*-axis of the detector, the

frequency term in the *y*-axis is not heterodyned. With this type of setup the Fizeau fringes corresponding to wavenumbers higher than the Littrow wavenumber are rotated in one direction in the plane of the detector while the Fizeau fringes corresponding to wavenumbers lower than Littrow are rotated in the opposite direction to produce a cross-hatched interference pattern.[9] A two-dimensional Fourier transform of the cross-hatched interference pattern recovers the spectral features above and below Littrow without ambiguity. An added benefit of operating in this two dimension SHS format is an increase in the spectral range by a factor of two.[8]

2.3 RAMAN SPECTROSCOPY

Raman scattering is a type of scattering theoretically predicted by A. Smekal in 1923 and observed experimentally by C. V. Raman and K. S. Krishnan in 1928.[10] Raman scattering involves a change in wavenumber of the incident radiation (e.g., the gain or loss of a vibrational quantum) and thus is said to be inelastic.[11] As shown in Figure 2.2, increase in wavenumber by a vibrational quantum is known as a Stokes shift and decrease in wavenumber by a vibrational quantum it is known as an anti-Stokes shift.[11] It should be noted that the arrows in Figure 2.2 should not be interpreted as distinct absorption and emission processes but rather as one process.[12] For a vibrational mode to Raman active it must follow two selection rules: 1) the change in vibrational state (Δv) must be ± 1 and 2) there must be a change in polarizability.[13]A disadvantage of Raman spectroscopy is that Raman scattering is extremely weak. A typical cross-section for absorption is ~ 10^{-17} $cm^2 \cdot sr^{-1}$ while the cross-section for a strong Raman scatterer is ~ 10^{-29} $cm^2 \cdot sr^{-1}$.[11] Scattering scales with the fourth power of wavenumber (σ^4), thus excitation lasers of a shorter wavelength will produce more Raman photons than excitation lasers of longer

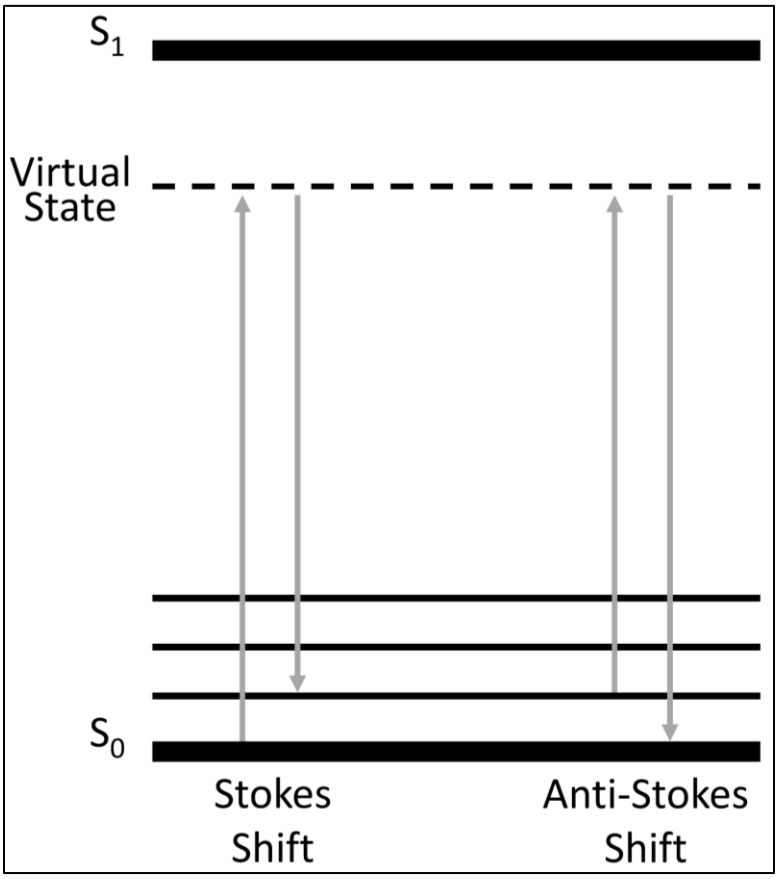

Figure 2.2: Jablonski energy level diagram for Raman scattering.

wavelength. Changing the excitation wavelength to the UV region can help to compensate for these low scattering cross-sections. The relative intensity of Raman scattering compared to other processes (i.e., fluorescence) can cause the Raman signal to be easily overwhelmed. There are three main ways in which this can be prevented: 1) filters can be employed to block out photons from other processes, 2) the excitation wavelength can be changed to a different region which reduces or prevents other wavelength-dependent processes from occurring (e.g., deep UV or IR excitation prevent fluorescence), 3) a pulsed laser and gated detection can block out processes that occur slower than scattering (e.g., fluorescence occurs on the timescale of $\geq 10^{-9}$ second while Raman scattering occurs on the timescale of $\leq 10^{-12}$ second). The theoretical number of Raman photons detected for a particular sample can be determined.[14]

$$S = (P\beta DK)(A\Omega TQ) \qquad \text{Eqn. 2.11}$$

Where S is Raman signal (photoelectrons pulse^{-1}), P is laser power (photons pulse^{-1} cm^{-2}), β is Raman cross-section for a particular Raman band of a particular sample (cm^2 molecule^{-1} sr^{-1}), D is number density of sample (molecule cm^{-3}), K is sample path length (cm), A is area viewed by the collection optics and spectrometer (cm^2), Ω is collection solid angle of the collection optics and spectrometer (sr), T is transmission of the optics (unitless), and Q is quantum efficiency of the detector (e$^-$ photon^{-1}). The variables in the first set of parenthesis relate to laser and sample while the variables in the second set of parenthesis related to collection optics and detector. Equation 2.11 is stated in terms of a pulsed laser but can be adapted to continuous wave lasers by changing variables in terms of pulse^{-1} to second^{-1}.

2.4 SPATIAL HETERODYNE RAMAN SPECTROMETER

The SHS design was first applied to Raman spectroscopy by Gomer *et al.* and was differentiated from the general SHS with the designation spatial heterodyne Raman spectrometer (SHRS).[15] The low scattering efficiency of Raman makes the high sensitivity of the SHS design especially appealing. An advantage of the SHRS over conventional Raman spectrometers is the lack of an entrance slit, allowing a much larger sample area to be interrogated at one time without loss of resolution or throughput.[15-17] Increasing the excitation laser spot size reduces irradiance at the sample without the necessity of reducing radiant flux of the laser.[11] Equation 2.11 indicates that the number of Raman photons generated is independent of excitation laser spot size, but a slit-based spectrometer is limited to a small area viewed (*A=slit width * slit height*) while the SHRS has a significantly larger entrance aperture, the size of which is only limited to a size small enough to prevent off-axis rays from degrading the interferogram. The ability to use a large laser spot size is especially useful with samples that would otherwise undergo photodegradation by a tightly focused laser, which can be problematic with deep-UV laser excitation.

At the time of publication of this work the SHRS has been applied to a variety of Raman spectroscopy applications. A variety of solid and liquid Raman samples have been investigated with both visible and UV excitation in both benchtop and standoff configurations.[15,16,18] The lack of moving parts within the SHS design has allowed it to be paired with a gated laser (both visible and deep-UV excitation) and gated detector which allows measurements of Raman sample in ambient light conditions.[19] The large entrance aperture and high sensitivity of the SHRS allowed for one-dimensional imaging of

pharmaceutical samples in a transmission Raman configuration.[17] The SHRS has also been employed in a two-dimensional configuration in which one diffraction grating is tilted vertically to produce a cross-hatched fringe pattern which doubles the spectral range and removes the ambiguity of spectral feature assignment.[15,20]

2.5 MINIATURIZATION OF THE SHRS

The SHRS is particularly well suited to miniaturization, even while maintaining a high resolution and large spectral range. The footprint of the SHRS is limited by the size of the optical components themselves because the diffraction gratings can be placed essentially arbitrarily close to the beamsplitter. Thus, the overall package size of the SHRS can be reduced by reducing the size of the optical components and moving the optical components closer to each other. The diffraction gratings used in the SHRS have a fundamental lower limit for miniaturization which is determined by the angular extent of the Airy disc. The minimum diffraction angle that can be resolved by an optical element can be determined through the Rayleigh criterion.[21]

$$\sin\theta_{min} = 1.220\,\frac{\lambda}{D} \qquad \text{Eqn. 2.12}$$

Where θ_{min} is the minimum diffraction angle that can be resolved by an optical element of diameter *D* at wavelength λ. The theoretical maximum groove density corresponds to a groove spacing of half the wavelength of light to be diffracted. This maximum groove density cannot be employed in the SHRS, however, because it would result in a diffraction angle of 90°, essentially preventing the diffracted light from even leaving the surface of the diffraction gratings. For a given resolution and groove density, the Rayleigh criterion can be used to determine the minimum grating size that can be employed. Table 2.1 shows the minimum grating widths and angular resolutions of

various excitation wavelengths at various groove densities while maintaining 5 cm^{-1} resolution. The excitation wavelengths were chosen because they are commonly found in lasers and are demonstrative of deep UV, visible, and near IR. The groove densities for each excitation wavelength were chosen because they are roughly 90%, 50%, and 10% of the maximum groove density. The Littrow angle was calculated with Equation 2.1 such that the corresponding excitation wavelength would be the Littrow wavenumber. The minimum grating width was calculated using Equation 2.4 reduced by a factor of 2. The factor of 2 reduction is done because Equation 2.4 is the diffraction limited resolving power for a 2-grating SHS. If resolution is fixed, the equation can be rearranged to find diffraction limited grating width at that resolution.

Throughput is an important consideration for any spectrometer as it directly relates to sensitivity which is especially important in Raman spectroscopy due to the low signal intensities and high backgrounds. The Kaiser Holospec f/1.8i is one of the highest throughputs of commercially available Raman spectrometers at the time of publication, thus it is useful for comparison of the SHRS design to one of the best commercially available Raman spectrometers. The collection solid angle and resolution of a slit-based spectrometer are given in the following equations.[11]

$$\Omega = \frac{\pi/4}{\left(\frac{F}{n}\right)^2} \qquad \text{Eqn. 2.13}$$

$$\Delta\sigma = 2R_d W \qquad \text{Eqn. 2.14}$$

Where R_d is the reciprocal linear dispersion and W is slit width. The Holospec is f/1.8 so the solid angle is 0.242 sr. The grating commonly used in the Holospec for Raman excitation at 532 nm has R_d = 2.4 cm^{-1} $pixel^{-1}$. Assuming a camera with 20 μm pixel pitch

results in R_d = 0.12 cm^{-1} μm^{-1} thus requiring a slit no wider than 20.8 μm to achieve a spectral resolution of 5 cm^{-1}. The slit of the Holospec is ~ 0.8 cm long. Applying Equation 2.7 results in an etendue of $4.0x10^{-4}$ cm^2 sr. A SHRS with the same spectral resolution and 300 groove/mm diffraction gratings would require diffraction gratings ~ 6.3 mm wide. The solid angle of the SHRS, found with Equation 2.6, is 0.0017 sr and, if we assume area viewed is the 80% clear aperture of a beamsplitter the same size as the diffraction gratings, the etendue is $3.3x10^{-4}$ cm^2 sr. The throughput of the Holospec is slightly higher but this particular SHRS would be > 3000x smaller while maintaining the same resolution and spectral range.

As the SHRS becomes smaller and smaller it will become more practical to switch to a monolithic design in which the diffraction gratings are mounted directly to wedge spacing prisms which are in-turn mounted directly to the beamsplitter. This reduces the difficulties associated with obtaining and implementing optomechanics of sufficient stability and precision to properly orient and stabilize miniature optical components. The monolithic SHRS design has the added benefit of reduced sensitivity to external vibrations because every optical component experiences the same external vibrations equally and simultaneously. However, it is currently unknown as to whether a monolithic design completely removes sensitivity to external vibration or simply reduces it. The extent of vibrational stability is of particular interest when designing systems to operate outside of a controlled laboratory environment.

Table 2.1: Minimum diffraction grating widths at various excitation wavelengths and various diffraction grating groove densities with a constant 5 cm^{-1} resolution.

Excitation Wavelength (nm)	Groove Density (groove/mm)	Littrow Angle (degrees)	Minimum Grating Width (mm)
785	2300	64.52	0.55
	1300	30.68	0.98
	260	5.86	4.9
532	3400	64.74	0.55
	1900	30.36	0.99
	380	5.80	4.9
244	7400	64.53	0.55
	4100	30.01	1.0
	820	5.74	5.0

REFERENCES

(1) J.M. Harlander, F.L. Roesler, C.R. Englert, J.G. Cardon, R.R. Conway, C.M. Brown, J. Wimperis. “Robust monolithic ultraviolet interferometer for the SHIMMER instrument on STPSat-1”. Appl. Opt. 2003. 42(15): 2829-2834.

(2) J.M. Harlander, F.L. Roesler. “Spatial heterodyne spectroscopy: a novel interferometric technique for ground-based and space astronomy”. Proc. SPIE. 1990. 1235: 622-633.

(3) T. Dohi, T. Suzuki. “Attainment of High Resolution Holographic Fourier Transform Spectroscopy”. Appl. Opt. 1971. 10(5): 1137-1140.

(4) J.M. Harlander. Spatial Heterodyne Spectroscopy: Interferometric Performance at Any Wavelength without Scanning. [Ph.D. Dissertation]. Madison, WI: University of Wisconsin-Madison, 1991.

(5) W. Harris, F. Roesler, B.J. Lotfi, E. Mierkiewicz, J. Corliss, R. Oliversen, T. Neef. “Applications of spatial heterodyne spectroscopy for remote sensing of diffuse UV-vis emission line sources in the solar system”. J. Electron. Spectrosc. Relat. Phenom. 2005. 144-147: 973-977.

(6) H. Nyquist. “Certain Topics in Telegraph Transmission Theory”. AIEE Trans. 1928. 617-644.

(7) W.H. Steel. “Interferometers without Collimation for Fourier Spectroscopy”. J. Opt. Soc. Am. 1964. 54(2): 151-156.

(8) J.M. Harlander, R.J. Reynolds, F.L. Roesler. “Spatial Heterodyne Spectroscopy for the Exploration of Diffuse Interstellar Emission Lines at Far-UV Wavelengths”. Astrophys. J. 1992. 396: 730-740.

(9) J.M. Harlander, F.L. Roesler, J.G. Cardon, C.R. Englert, R.R. Conway. “SHIMMER: a spatial heterodyne spectrometer for remote sensing of Earth's middle atmosphere”. Appl. Opt. 2002. 41(7): 1343-1352.

(10) C.V. Raman. “A New Type of Secondary Radiation”. Nature. 1928. 121: 501-502.

(11) J.D. Ingle Jr., S.R. Crouch. Spectrochemical Analysis, 1st ed. Prentice Hall: Englewood Cliffs, NJ, 1988.

(12) J.L. McHale. Molecular Spectroscopy, 1st ed. Prentice Hall: Upper Saddle River, NJ, 1999.

(13) J.R. Ferraro, K. Nakamoto. Introductory Raman Spectroscopy. Academic Press: San Diego, CA, 1994.

(14) S.M. Angel, N.R. Gomer. "Remote Raman Spectroscopy for Planetary Exploration: A Review". Appl. Spectrosc. 2012. 66(2): 137-150.

(15) N.R. Gomer, C.M. Gordon, P. Lucey, S.K. Sharma, J.C. Carter, S.M. Angel. "Raman Spectroscopy Using a Spatial Heterodyne Spectrometer: Proof of Concept". Appl. Spectrosc. 2011. 65(8): 849-857.

(16) N. Lamsal, S.M. Angel. "Deep-Ultraviolet Raman Measurements Using a Spatial Heterodyne Raman Spectrometere (SHRS)". Appl. Spectrosc. 2015. 69(5): 525-534.

(17) K.A. Strange, K.C. Paul, S.M. Angel. "Transmission Raman Measurements using a Spatial Heterodyne Raman Spectrometer (SHRS)". Appl. Spectrosc. Published online before print June 30, 2016. doi: 10.1177/0003702816654156.

(18) G. Hu, W. Xiong, H. Shi, Z. Li, J. Shen, X. Fang. "Raman spectroscopic detection for liquid and solid targets using a spatial heterodyne spectrometer". J. Raman Spectrosc. 2016. 47: 289-298.

(19) N. Lamsal, S.M. Angel, S.K. Sharma, T.E. Acosta. "Visible and UV Standoff Raman Measurements in Ambient Light Conditions Using a Gated Spatial Heterodyne Raman Spectrometer". 46th Lunar and Planetary Science Conference. The Woodlands, Texas, March 16-20, 2015.

(20) G. Hu, W. Xiong, H. Shi, Z. Li, J. Shen, X. Fang. "Raman spectroscopic detection using a two-dimensional spatial heterodyne spectrometer". Opt. Eng. 2015. 54(11): 114101.

(21) G.O. Reynolds, J.B. DeVelis, G.B. Parrent Jr., B.J. Thompson. The New Physical Optics Notebook: Tutorials in Fourier Optics; SPIE-The International Society for Optical Engineering: Bellingham, WA and American Institute of Physics: New York, NY, 1989.

CHAPTER 3

IMPROVING SPECTRAL RESULTS THROUGH ROW-BY-ROW FOURIER TRANSFORM OF SPATIAL HETERODYNE RAMAN SPECTROMETER INTERFEROGRAMS

3.1 INTRODUCTION

The spatial heterodyne Raman spectrometer (SHRS) is a dispersive interferometer, which generates a two-dimensional spatial interference Fizeau fringe pattern, capturing the entire interferogram simultaneously with an array detector. The design of the SHRS has been described in great detail previously,[1-12] however a brief explanation is necessary to more easily understand the techniques described in this work. The SHRS (shown in Figure 3.1) is similar to the Michelson interferometer, with a central beamsplitter which splits incoming light into two coherent beams that strike stationary diffraction gratings rather than the scanned mirror and stationary mirror as used in a Michelson interferometer. The diffraction gratings induce a wavelength-specific wavefront tilt. Diffracted light from each interferometer arm recombines through the beamsplitter, causing a crossing of the wavefronts from each arm, inducing a wavenumber dependent spatial phase shift along the dispersion plane, which generates interference resulting in a Fizeau fringe pattern. The faces of the gratings are imaged onto an array detector, which captures the fringe pattern. There is one wavelength of light, called the Littrow wavelength, which leaves the gratings along the incident axis, thus has no wavefront tilt which prevents wavefront crossing from the two arms of the

interferometer and generates no spatial interference pattern. All other wavelengths are heterodyned about the Littrow wavelength, which allows the entire spectral range to be captured with a relatively small number of detector elements and without scanning the diffraction gratings. The spatial fringe frequency generated is given by Equation 3.1:

$$f = 4(\sigma - \sigma_L)\tan\theta_L \qquad \text{Eqn. 3.1}$$

Where f is the spatial fringe frequency on the detector, σ_L is the Littrow wavelength in wavenumbers, σ is any other wavelength in wavenumbers, and θ_L is the angle of rotation of the diffraction gratings. Equation 1 indicates that wavelengths longer and shorter than Littrow will produce degenerate fringe patterns, resulting in ambiguity in the discrimination of whether a spectral feature is above or below Littrow. This can be overcome by tilting one of the diffraction gratings vertically, which induces a spatial phase shift in the axis orthogonal to the dispersion plane of the gratings, causing the fringes resulting from spectral features at wavelengths longer than Littrow to be rotated in one direction and the fringes resulting from spectral features at wavelengths shorter than Littrow to be rotated in the opposite direction.[7]

In the SHRS small optical misalignments can induce large errors in the generated fringe pattern. These optical misalignments can often be difficult to correct in the instrument, requiring large, high-precision optical mounts and extremely careful alignment. Certain types of optical misalignments result in wavelength-dependent and wavelength-independent rotations of the fringe pattern on the detector. It is possible to correct these types of misalignments mechanically by careful initial alignment with a strong emission source (e.g., Hg vapor lamp) followed by careful tweaking with a high Raman-cross-section sample (e.g., sulfur), which is helpful for final alignment due to the

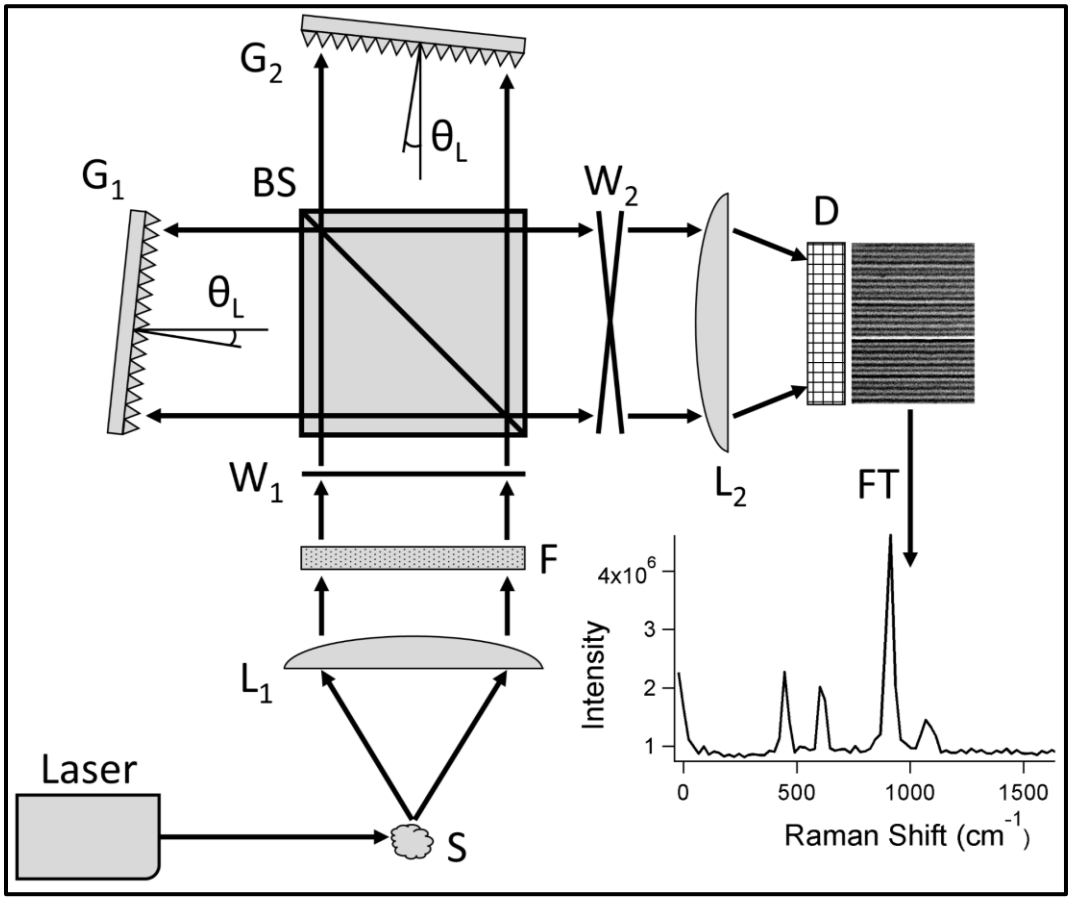

Figure 3.1: Schematic diagram of the SHRS: S = sample, L_1 = collimating lens, F = laser rejection filters, W_1 = the plane wave of the sample light entering the SHRS, BS = cube beamsplitter, G_1 = G_2 = diffraction grating, θ_L = diffraction grating rotation angle, W_2 = crossed wavefronts from each arm of the interferometer, L_2 = imaging lens, D = array detector.

significantly shorter coherence length of Raman bands. There are still types of optical misalignments that cannot be easily detected until the final spectrum is obtained, as we will show in this work, which significantly increases the difficulty in obtaining a proper optical alignment. However, it is possible to correct the effects of these types of fringe misalignments with relatively simple and computationally efficient post-processing.

Recovery of the spectrum from the fringe pattern generated by the SHRS has been reported using three different methods: 1) applying a two-dimensional fast Fourier transform (FFT) to the fringe image to produce a 2D spectrum which is then summed or averaged to recover the 1D spectrum,[1] 2) summing the columns of the array detector to produce a one-dimensional interferogram, or fringe cross section, then applying the FFT to produce a 1D spectrum,[2-6] and 3) applying a one-dimensional FFT to each row of the fringe pattern to recover a spectrum for each row which are then averaged together to recover the final spectrum.[8] The first and second methods of applying the FFT to the interferogram generated by the SHRS has been discussed at length in the literature, however the third method has only briefly been described in the literature with no accompanying discussion of the benefits of the method. We have found that the effects of fringe rotation in the plane of the detector caused by a vertical tilt of the dispersive elements of the SHRS or rotation of the dispersive elements about the optical axis can be corrected in post-processing by applying the FFT in this third manner. If the fringe pattern is rotated on the plane of the detector, the column-sum method, denoted above as the second method, will not produce an interferogram that accurately represents the fringe pattern, and if the rotation of the fringe pattern is great enough, a useful one-dimensional interferogram cannot be recovered by this method. Furthermore, even a

small rotation of the fringes on the detector will result in a decreased signal-to-noise ratio (SNR) when the column-sum FFT method is employed. The 2D FFT is capable of recovering the spectrum when the fringes are rotated on the detector, and is particularly useful for certain configurations of the SHRS in which a cross-hatched interferogram, composed of both clockwise rotated fringes and counter-clockwise rotated fringes, is formed. However, if this type of cross-hatched interferogram is not generated, the 2D FFT distributes the noise of a y-axis Fourier transform into the 2D spectrum unnecessarily which increases the noise in the final spectrum. We have found that if the Fourier transform is applied to each row of the fringe image individually as described in the third method above, the output spectrum of each row is not significantly different than if the fringe pattern were not rotated. This is due to the fact that the fringe modulation within a given row of pixels does not change significantly with rotation of the fringes because, relative to that row of pixels, rotation is equivalent to the 1D interference pattern being shifted left or right without significant alteration to the spatial frequency of the fringes or depth of modulation. Shifting the 1D interference pattern left or right within a given row of pixels does not significantly affect the output of the Fourier transform because the sine/cosine waves that are fit by the Fourier transform are not a function of absolute position within the input vector. Thus, the spectrum can be recovered from a rotated fringe pattern without the unnecessary noise added by a 2D FFT.

3.2 EXPERIMENTAL

Two different SHRS setups were used for the data shown, an SHRS with 25 mm optics, hereafter referred to as the large SHRS, and an SHRS with miniature 2.5 mm optics, hereafter referred to as the miniature SHRS. Both setups have been described

elsewhere,[5,12] however a brief description of each system is provided here. The large SHRS was constructed using a 25 mm cube beamsplitter (CM1-BS013, Thorlabs Inc., Newton, New Jersey, USA), and two 25 mm square 150 grooves/mm diffraction gratings. A high quality imaging lens (105 mm focal length, f/2.8 AF Micro-Nikkor, Nikon Corp., Tokyo, Japan) was used to image the faces of the diffraction gratings onto a liquid nitrogen cooled 1340x1300 element CCD (VersArray, Princeton Instruments, Trenton, New Jersey, USA). The diffraction gratings were held in four-axis grating mounts (DGM-1, Newport Corp., Irvine, California, USA) to allow precision adjustment of grating pitch, yaw, roll, and z-axis translation with 50 microradian angular sensitivity. A 532 nm CW laser (Millenia Pro 2s, Spectra-Physics, Santa Clara, California, USA) was used for Raman excitation. Raman scattered light was collected and collimated using a 25 mm diameter f/2 achromatic lens (49766, Edmund Optics, Barrington, New Jersey, USA). Scattered laser light was rejected using a combination of a 532 nm razor-edge long-pass filter (LP03-532RE-25, Semrock, Rochester, New York, USA) and a 532 nm notch filter (SuperNotch Plus, Kaiser Optical Systems Inc., Ann Arbor, Michigan, USA) placed in the collimated beam in front of the SHRS.

The miniature SHRS was constructed with a 5 mm cube beamsplitter (BS007, Thorlabs Inc., Newton, New Jersey, USA) and two 25 mm square 300 grooves/mm diffraction gratings (GR25-0305, Thorlabs Inc., Newton, New Jersey, USA) which were masked to allow only a 2.5 mm wide area to be illuminated, effectively acting as 2.5 mm gratings. A high quality imaging lens (80-200 mm focal length f/4.5-5.6 D, Nikon Corp., Tokyo, Japan) was used to image the faces of the diffraction gratings onto a CCD (Pixis 400, Princeton Instruments, Trenton, New Jersey, USA) which was thermoelectrically

cooled to -70 °C. A 532 nm CW laser (MLL-III-532, Opto Engine LLC, Midvale, Utah, USA) was used for Raman excitation. The laser power was set to ~ 100 mW and focused onto the sample using a 25 mm diameter, f/16 lens, providing a focused laser spot a few hundred micrometers in diameter. A 25 mm diameter f/2 lens was used to collect and collimate the scattered light from the sample into the SHRS. Two 532 nm razor-edge long-pass filters (LP03-532RE-25, Semrock, Rochester, New York, USA) were used to reject scattered laser light. The Littrow wavelength was set to the laser wavelength, 532 nm, for both systems. Powder samples of high-purity sulfur (J.T. Baker Chemical, item number: 4088-1) and potassium perchlorate (Sigma-Aldrich, ≥ 99% purity, item number: 241830 were pressed into compact pellets using a 10 ton pellet press. All data was processed with MATLAB and spectra were prepared for figures using Igor Pro.

3.3 RESULTS & DISCUSSION

Figure 3.2 shows a Raman fringe image that was measured with the miniature SHRS for a sulfur sample. It is necessary to mention that with the 25 mm diameter f/2 collection lens ~99% of the collected light was lost due to the small size of the diffraction gratings, however the optical efficiency is not germane to the studies described in this work as the sample light impingent upon the gratings was sufficient to recover strong spectra. Figure 3.2a shows a typical manner in which SHRS fringe images have been processed to recover the Raman spectrum. The fringe image is column-summed to produce a 1D interferogram, or fringe cross section, to which the FFT is applied to recover the spectrum. This method has some obvious deficiencies; such as if the fringe pattern is rotated, it would produce a distorted 1D interferogram upon column-summation. Rotated fringes will widen the fringe modulation, resulting in an inaccurate

interferogram, which will in turn result in a distorted spectrum. It may be possible to shift the rows to re-align a rotated fringe pattern, however this is either extremely tedious if done manually or complex if done using a computer program. Figure 3.2b shows another way to correct for fringe rotation in post-processing by simply applying the FFT in a different manner. In this case the Fourier transform is applied to every row of pixels individually to produce row-specific spectra, which are then summed to recover the final spectrum. Note: in Figure 3.2b only 5 row interferograms are shown for simplicity. The individual row interferograms are not significantly different when the fringe pattern is rotated than when the fringe pattern is not rotated. Upon Fourier transformation, the row-specific spectra are not significantly different from each other in terms of spectral feature location within the Fourier domain. Thus, upon summation of the row-specific spectra the spectral peaks are not shifted and the spectrum is not distorted. The row-by-row FFT method can also be used to correct other types of fringe displacement, such as wavy or curved fringes.

Figure 3.3 shows a comparison of three different methods of applying the Fourier transform to a Raman fringe image, collected with the miniature SHRS, where the fringes were intentionally rotated by about 8°. One diffraction grating of the miniature SHRS was tilted vertically to induce a spatial phase shift orthogonal to the diffraction grating dispersion plane, causing the fringe pattern to be rotated on the detector as shown in the fringe image of potassium perchlorate Raman in Figure 3.3a. The SHRS, like other interferometers, is very sensitive to alignment and only a very slight vertical tilt was required to induce the significant fringe rotation observed here. Figure 3.3b shows the intensity cross-section that is produced by column summation of the rotated fringe image,

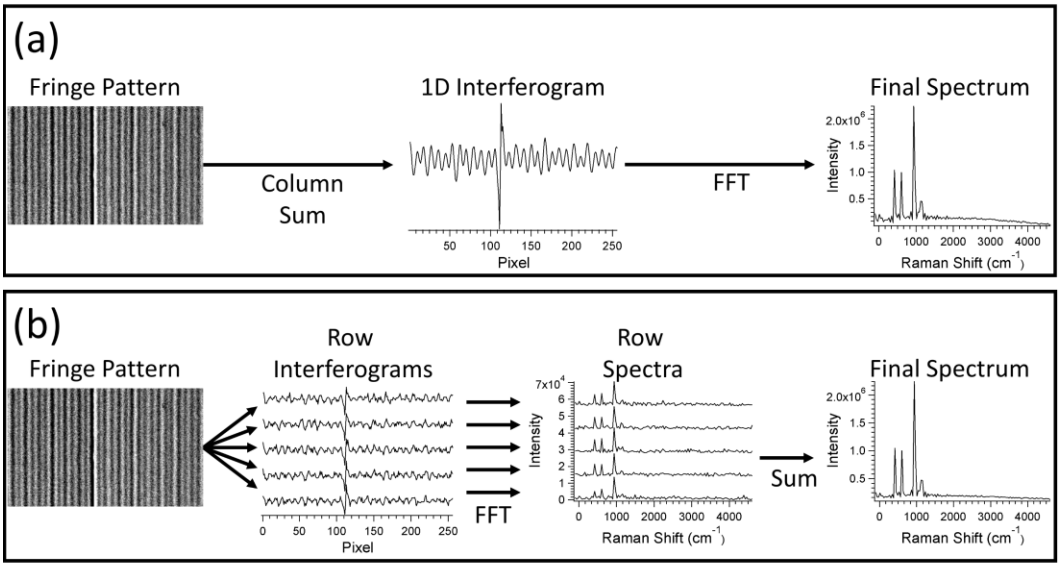

Figure 3.2: Comparison of column-sum Fourier transform and row-by-row Fourier transform. (a) Typically the fringe pattern generated by the SHS is column summed to produce a one-dimensional interferogram which is Fourier transformed to recover the spectrum. (b) The row-by-row FT involves performing the FT over each row of the 2D fringe pattern individually to produce a spectrum for each row which are then summed to recover the final spectrum.

and shows no evidence of interference fringes. The sharp drop in intensity around the~ 500 pixel point is due to a vertical strip of dead pixels near the middle of the fringe image. The FFT of the column sum is shown in Figure 3.3c and, as expected, no Raman spectral features of perchlorate are observed.

It is possible to recover a spectrum from the rotated fringe pattern shown in Figure 3.3a by applying a 2D FFT. The 2D FFT is shown in Figure 3.3d, and can be considered to be the combination of the FFT along the x-axis of the image with the FFT along the y-axis of the image, resulting in a 2D Raman spectrum. As shown in Figure 3.3d, the spectral intensity in the 2D Raman spectrum generated by the 2D FFT is localized to only a few rows while all other rows contain noise, distributed by the FFT along the x-axis and y-axis of the fringe image. The y-axis position of peaks within the 2D spectrum generated by the 2D FFT relates information about direction and magnitude of fringe rotation, and as described in previously published SHRS papers, this information can be used to unambiguously determine Raman bands both above and below the Littrow wavenumber.[2-4] Figure 3.3e shows the Raman spectrum that is obtained by summing all rows of the 2D FFT image. The Raman spectrum is recovered with a SNR of ~71, determined as the ratio of the baseline subtracted peak intensity to the standard deviation of a region of the baseline in which no peaks are present, a great improvement over the spectrum shown in Figure 3.3c. As shown in Figure 3.3f, the SNR is further improved to ~156 by summing only the rows of the 2D spectrum in which the spectral features are most prominent.

The largest SNR improvement is obtained by applying the FFT to each row of the fringe image in Figure 3.3a individually to produce the 2D Raman spectrum shown in

Figure 3.3g, where each row corresponds to the Raman spectrum of each row of the fringe image. Unlike the 2D FFT, spectral features can be observed in every row of the 2D spectrum of the row-by-row FFT in Figure 3.3g, removing the necessity of selecting rows in which spectral features are located. The final Raman spectrum is recovered by summing each row of the 2D row-by-row FFT spectrum, as shown in Figure 3.3h. The SNR of the row-by-row FT in Figure 3.3h is ~310, significantly greater than even the best spectrum produced by the 2D FFT for this data. As discussed above, the 2D FFT is the combination of the FFT along the x-axis of the image and the FFT along the y-axis of the image. Essentially, the row-by-row FFT is only half of the 2D FFT process, allowing the relevant spectral information to be recovered from the fringe images generated by the SHRS without the noise of the y-axis FFT being distributed into the 2D spectrum, which allows the row-by-row FFT to achieve a higher SNR. Unlike the 2D FFT method, the row-by-row FFT process does not remove the degeneracy for bands above and below the Littrow wavenumber (see Equation 3.1), which is important if there is an interest in measuring bands above and below Littrow simultaneously (*e.g.*, measuring both Stokes and anti-Stokes Raman bands when Littrow is set to the excitation wavelength or doubling the spectral range).

The discussion of Figure 3.3 is related to fringe rotation caused by a vertical tilt of a diffraction grating in the interferometer. A vertical tilt of the diffraction grating introduces a spatial phase shift along the axis orthogonal to the dispersion plane of the diffraction grating. That is to say, the phase shift at the top of the grating will be slightly different than the phase shift at the middle of the grating or bottom of the grating. Thus each point on the detector is a combination of the y-axis phase shift due to the tilt of the

grating and the x-axis phase shift due to the wavefront tilt induced by diffraction. As the y-axis phase shift is independent of wavelength and is the same at a given point for each wavelength, the degree of fringe rotation is the same for each wavelength, thus the fringe rotation is wavelength independent. It is also possible to have a wavelength dependent fringe rotation, caused by the grating being rotated so that the grooves of one grating are not perfectly parallel to the grooves of the other grating. When the dispersion planes of the diffraction gratings are not perfectly parallel to each other, that is to say the gratings are not perfectly level with respect to each other, each wavelength of light has its own specific, diffraction-induced x-axis phase shift due to the tilt of the wavefront, as above. However, because the dispersion planes are not parallel to each other, this also induces a wavelength-specific y-axis component to the phase shift at a given point. That is to say, if one grating's dispersion plane lies perfectly in the xz-plane, where z is the optical axis, and the other grating's dispersion plane is slightly rotated about the z-axis such that it forms an angle with the xz-plane, the wavelength-specific diffraction along the dispersion plane of the first grating will have only a x-axis phase component because there is no phase change along the y-axis (assuming the grating surface is perfectly normal to the optical axis), however the wavelength specific diffraction along the dispersion plane of the second grating will have both a x-axis phase component and a y-axis phase component simultaneously, even if the second grating's surface is normal to the optical axis. Thus each wavelength of light leaving the second grating will have its own unique y-axis phase component leading to the rotation of the fringe pattern to be wavelength specific where the fringes resulting from one wavelength have a different rotation angle on the detector than the fringes resulting from a different wavelength. The angular

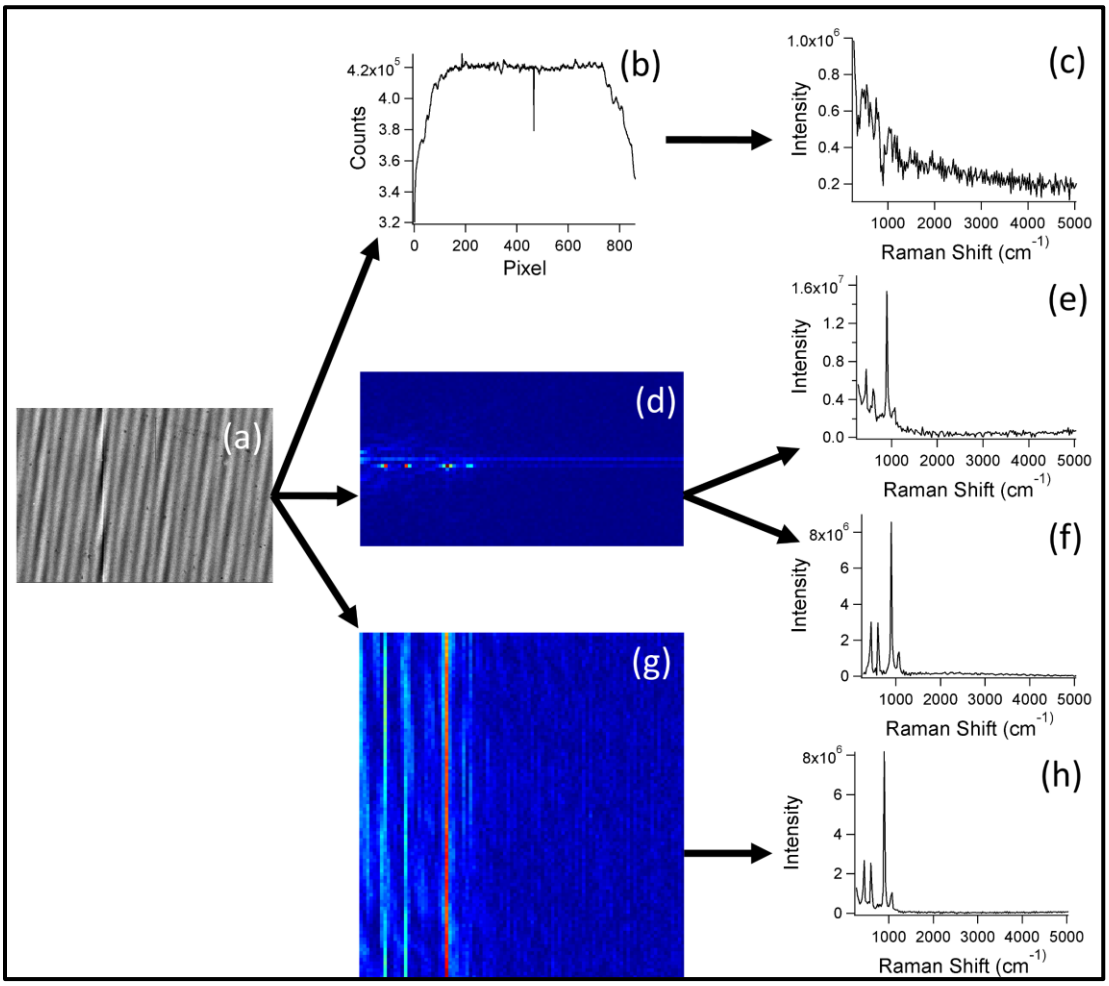

Figure 3.3: Comparison of three different methods of applying the Fourier transform with rotated fringes. (a) Intentionally rotated potassium perchlorate Raman fringe pattern. (b) The typical column sum interferogram. (c) The Fourier transform of the column sum interferogram. (d) A heat map of 2D FFT 2D spectrum zoomed in so that the relatively narrow peaks can be more easily seen. (e) The spectrum obtained by a column sum of the 2D FFT. (f) The spectrum obtained by selecting only the row of the 2D spectrum in which the spectral bands are the most intense. (g) A heat map of the row-by-row FFT 2D spectrum. (h) The spectrum obtained by the column sum of the 2D spectrum generated by the row-by-row FFT. Note: images are not scaled the same.

mismatch between the dispersion planes of the diffraction gratings required for this to negatively affect the final spectrum is small enough that it cannot be easily detected by eye. Ideally this can be avoided by careful alignment using high precision four-axis grating mounts in the SHRS, but in practice small misalignments are difficult to avoid. However, it is possible to correct for the problem of dispersion plane angular mismatch with the row-by-row FFT.

Figure 3.4a shows the Raman spectrum of potassium perchlorate, collected with the large SHRS, using the typical sum-column FFT method, but with the diffraction gratings slightly misaligned intentionally to induce a wavelength-dependent fringe rotation. The relative band intensity does not conform to that which we would expect to find with potassium perchlorate and there are significant band artifacts, such as the relatively strong band shoulder located on the low-wavenumber side of the 941 cm^{-1} band which is not expected.[13] Specifically, the lower wavenumber bands have a much higher intensity relative to the higher wavenumber bands. This is an indication that the high spatial frequency fringes were rotated on the detector, causing their intensity in the 1D interferogram to be reduced, resulting in a lower spectral intensity. In Figure 3.4a, the full-width half-maximum (FWHM) of the 941 cm^{-1} perchlorate band is 10 cm^{-1} and the SNR is ~110. Figure 3.4b shows the Raman spectrum using the same approach, but in this case the diffraction grating was carefully re-aligned so there was no observable wavelength-dependent fringe rotation in the Raman fringe image. As expected, this spectrum shows a significantly improved signal-to-noise ratio of ~364, and a relative band intensity more similar to that which we would expect for potassium perchlorate and a FWHM of the 941 cm^{-1} band of ~9 cm^{-1}. Also, the artifact appearing on the 941 cm^{-1}

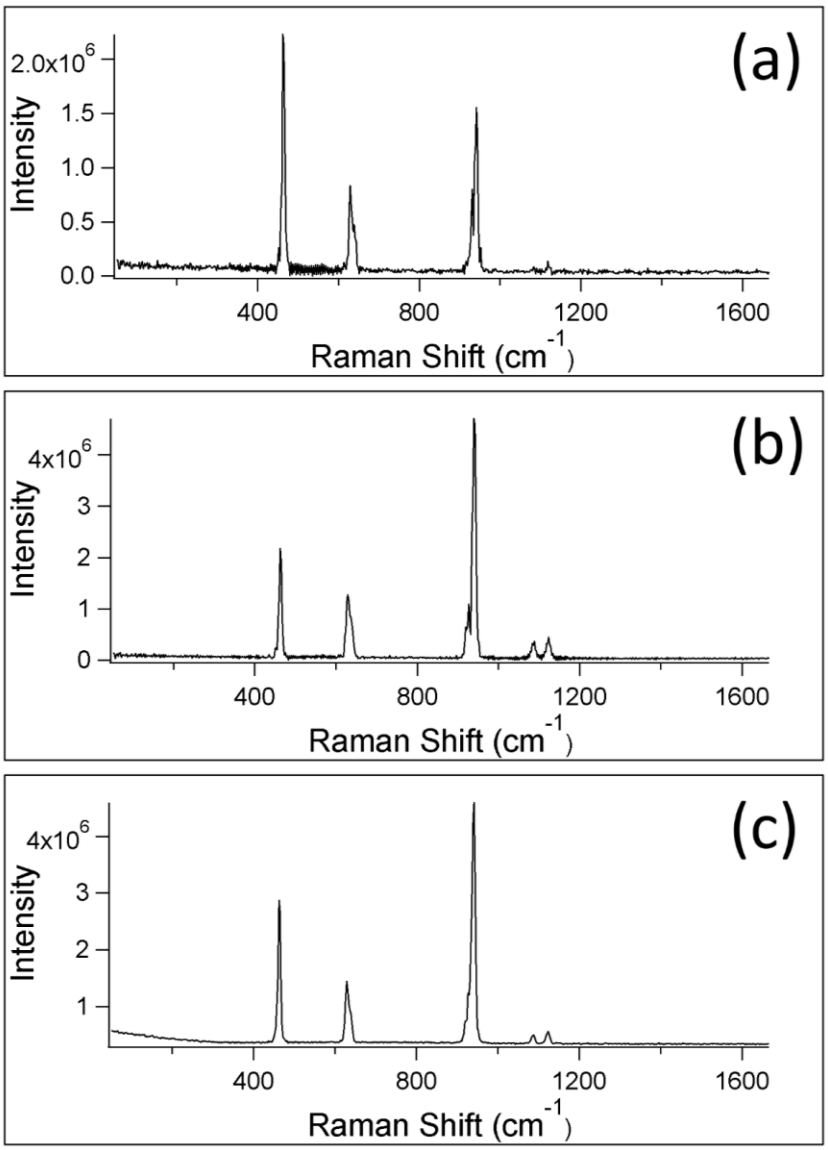

Figure 3.4: Comparison of spectral results when one diffraction gratings is rotated about the optical axis. (a) The typical column-summed FT applied to potassium perchlorate Raman with the diffraction gratings rotated slightly about the optical axis so the grooves are not exactly parallel, which induces a small wavelength-dependent fringe rotation, distorting relative peak intensities, and reducing overall peak intensity. (b) The sum-column FFT of potassium perchlorate after 4-axis grating mounts were used to adjust the grating rotation to remove the wavelength-dependent fringe rotation. (c) The row-by-row FFT of the potassium perchlorate Raman data with the gratings imperfectly aligned as in (a).

band is greatly reduced.

Figure 3.4c shows the Raman spectrum produced using the row-by-row FFT method, obtained with the same intentionally misaligned fringe image to produce the spectra in Figure 3.4a. The SNR of the row-by-row FFT produced Raman spectrum shown in Figure 3.4c, ~761, higher than the spectra in Figures 3.4a-b, and the relative intensity are as expected for potassium perchlorate with 9 cm^{-1} band resolution. Also, there are no spectral artifacts or unexpected band shoulders. The 2 to 7 fold increase in SNR shows that the row-by-row FFT method provides improved SNR over the column-sum method even when there is no visually observable misalignment in the interferometer.

3.4 CONCLUSIONS

Very slight misalignment of the diffraction gratings in the SHRS spectrometer can lead to both wavelength independent and wavelength dependent fringe rotation in the Raman fringe images, which can lead to decreased SNR and band artifacts in the resulting Raman spectra. These effects can be minimized by proper application of the FFT to the fringe images. Application of a 2D FFT to the Raman fringe image is useful to recover the Raman spectrum for the case of wavelength independent fringe rotation in the Raman fringe image and provides higher SNR than applying the FFT to a fringe cross section that is generated by summing all the rows in the fringe image. However, applying the FFT to each row of the Raman fringe image separately, then summing the resulting Raman spectra provides higher SNR and fewer spectral artifacts than the 2D FFT method, for the case of both wavelength independent and wavelength-dependent fringe rotation.

REFERENCES

(1) R.J. Bartula, J.B. Ghandhi, S.T. Sanders, E.J. Mierkiewicz, F.L. Roesler, J.M. Harlander. "OH absorption spectroscopy in a flame using spatial heterodyne spectroscopy". Appl. Opt. 2007. 46(36): 8635-8640.

(2) N.R. Gomer, C.M. Gordon, P. Lucey, S.K. Sharma, J.C. Carter, S.M. Angel. "Raman Spectroscopy Using a Spatial Heterodyne Spectrometer: Proof of Concept". Appl. Spectrosc. 2011. 65(8): 849–857.

(3) N. Lamsal, S.M. Angel. "Deep-Ultraviolet Raman Measurements Using a Spatial Heterodyne Raman Spectrometer (SHRS)". Appl. Spectrosc. 2015. 69(5): 525–534.

(4) N. Lamsal, S.K. Sharma, T.E. Acosta, S.M. Angel. "Ultraviolet Stand-off Raman Measurements Using a Gated Spatial Heterodyne Raman Spectrometer". Appl. Spectrosc. 2016. 70(4): 666-675.

(5) K.A. Strange, K.C. Paul, S.M. Angel. "Transmission Raman Measurements using a Spatial Heterodyne Raman Spectrometer (SHRS)". Appl. Spectrosc. Published online before print June 30, 2016. doi: 10.1177/0003702816654156.

(6) P.D. Barnett, N. Lamsal, S.M. Angel. "Standoff LIBS using a Miniature Wide Field of View Spatial Heterodyne Spectrometer with Sub-Microsteradian Collection Optics". Appl. Spectrosc. Paper in press 2016.

(7) J.M. Harlander. Spatial Heterodyne Spectroscopy: Interferometric Performance at Any Wavelength without Scanning. [Ph.D. Dissertation]. Madison, Wisconsin: University of Wisconsin-Madison, 1991.

(8) G. Hu, W. Xiong, H. Shi, Z. Li, J. Shen, X. Fang. "Raman spectroscopic detection for liquid and solid targets using a spatial heterodyne spectrometer". J. Raman Spectrosc. 2015. 47(3): 289-298.

(9) J.M. Harlander, F.L. Roesler, R.J. Reynolds, K. Jaehnig, W.A. Sanders. "Differential, Field-Widened Spatial Heterodyne Spectrometer for Investigations at High Spectral Resolution of the Diffuse Far Ultraviolet 1548 Å Emission Line from the Interstellar Medium". Proc. SPIE. 1993. 2006: 139-148.

(10) J.M. Harlander, F.L. Roesler, S. Chakrabarti. "Spatial Heterodyne Spectroscopy: A Novel Interferometric Technique for the FUV". In: O.H.W. Siegmund; H.S. Hudson, editors. EUV, X-Ray, and Gamma-Ray Instrumentation for Astronomy. Proc. SPIE. 1990. 1344: 120-131.

(11) I.B. Gornushkin, B.W. Smith, U. Panne, N. Omenetto. “Laser-Induced Breakdown Spectroscopy Combined with Spatial Heterodyne Spectroscopy”. Appl. Spectrosc. 2014. 68(9): 1076-1084.

(12) P.D. Barnett, S.M. Angel. “Miniature Spatial Heterodyne Raman Spectrometer with a Cell Phone Camera Detector”. Appl. Spectrosc. Published online before print August 29, 2016. doi: 10.1177/0003702816665127

(13) N. Krishnamurthy. “Raman Spectrum of Crystalline Potassium Perchlorate”. Proceedings of the Indian Academy of Sciences – Section A. 1965. 61(2): 118-121.

CHAPTER 4

MINIATURE SPATIAL HETERODYNE RAMAN SPECTROMETER WITH A CELL PHONE CAMERA DETECTOR

4.1 INTRODUCTION

The spatial heterodyne Raman spectrometer (SHRS) is a dispersive-based interferometer, which has high throughput, a large field-of-view, high resolution, and large spectral range, in a small form factor which can be miniaturized to the millimeter scale. The SHRS described here is orders of magnitude smaller than CCDs typically employed with Raman spectrometers, which has prompted the exploration of smaller form-factor detectors. Cell phones have become ubiquitous with continuously improving optics and camera sensors in a small package, with tens of megapixels commonly available on millimeter-sized sensor chips, at the time of publication. The spectral range of the SHRS is limited by the spectral resolution and the number of detector elements in the dispersion plane of the diffraction gratings. The high pixel density of the small sensor chips used in cell phones allows for a high resolution SHRS while maintaining a large spectral range. However, unlike the high quality CCDs typically used with Raman spectrometers, CMOS sensors typically employed in most cell phone cameras are not cooled which increases thermal noise significantly, have noisier analogue-to-digital converters further increasing noise, and are only 8-bit or 10-bit instead of the 16-bit typical of scientific quality CCDs. Thus, cell phone sensors have significantly lower sensitivity and significantly higher noise. The high throughput and multiplex advantage

of the SHRS can overcome the inherently more noisy sensor typically employed in cell phone cameras.

The operation of the SHRS has been described in detail elsewhere,[1-10] however a brief overview is necessary. The SHRS is similar in design to the Michelson interferometer, commonly used for FT-IR measurements, however, rather than a scanning mirror and stationary mirror, the SHRS has two stationary diffraction gratings, G_1 and G_2 in Figure 4.1. The diffraction gratings are tilted such that one wavelength, the Littrow wavelength, satisfies the Littrow condition and diffracts along the same optical path as the input light, θ_L in Figure 4.1. All other wavelengths of light diffract at wavelength-specific angles, inducing a wavelength-specific wavefront tilt. When the tilted wavefronts recombine through the beamsplitter, the crossed wavefronts, W_2 in Figure 4.1, from each diffraction grating induces a spatial phase shift along the dispersion plane of the gratings, causing interference to occur, thus producing a set of Fizeau fringes. The plane of the diffraction gratings is imaged with a lens, L_2 in Figure 4.1, onto an array detector, D in Figure 4.1. The Fourier transform of these fringes recovers the spectrum. During spectral acquisition the gratings are not scanned and there are no moving parts. The resolving power of the SHRS is determined by the number of grooves of the diffraction grating illuminated, and is not a strong function of the entrance aperture size. Thus very small diffraction gratings can be used while maintaining high resolution and high light throughput. This allows the SHRS to be miniaturized to the millimeter scale while maintaining high resolution and a large spectral range.

Recent years have seen a surge in the application of cell phone cameras for scientific imaging including molecule and nanoparticle imaging,[11,12] medical applications

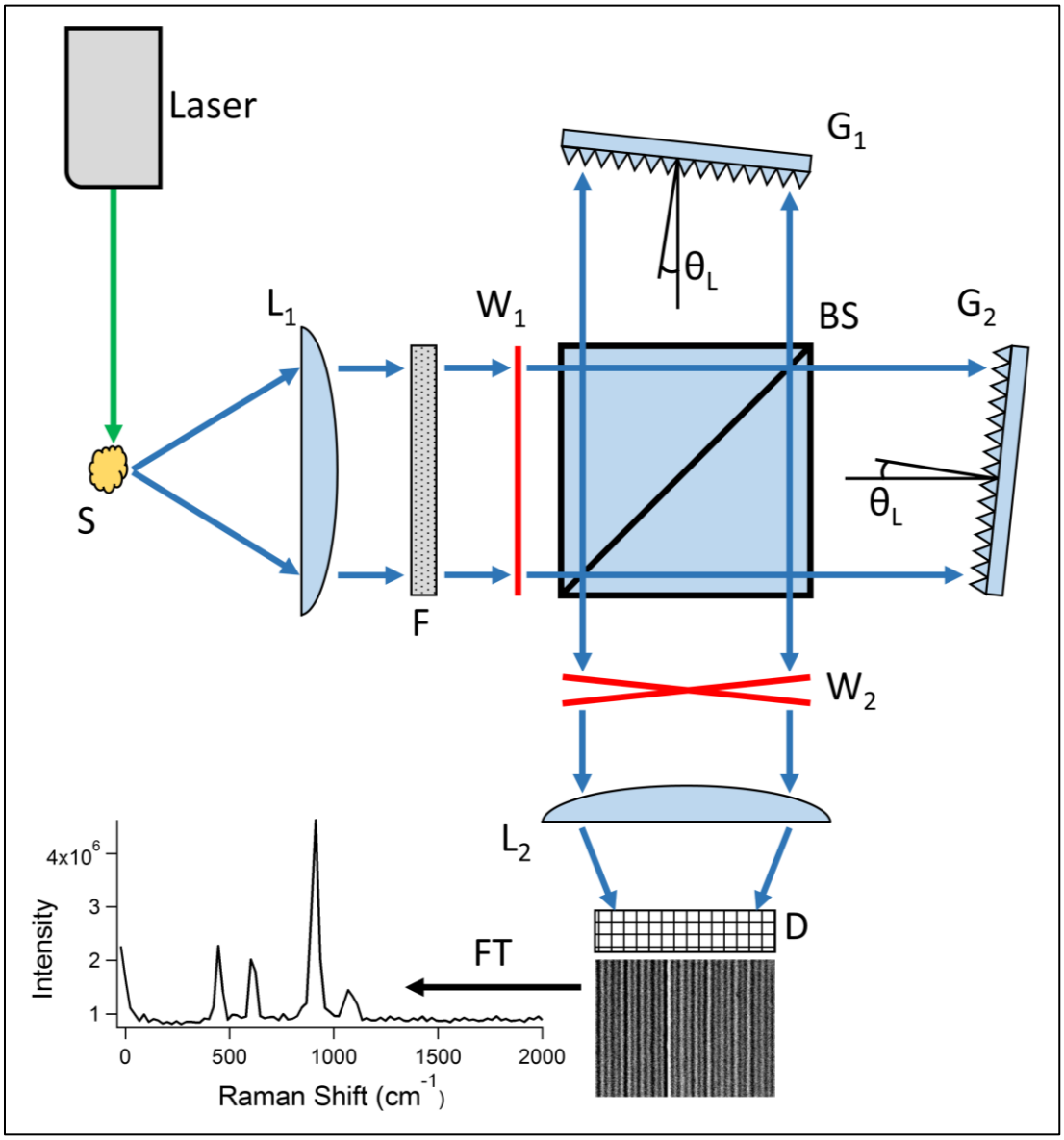

Figure 4.1: Schematic diagram of the SHRS. S is the sample to be analyzed, L1 is a collection lens which collimates collected Raman scattered light into the SHRS, F is a laser rejection filter, W1 is the incoming wavefront of light, BS is a cube beamsplitter, G1 and G2 are diffraction gratings, θ_L is the grating tilt angle which satisfies the Littrow condition for a specific wavelength, W2 is the crossed wavefronts from each arm of the interferometer, L2 is a high-quality imaging lens which images the plane of the diffraction grating onto an array detector, D. An example fringe pattern is shown below the array detector, D, and the Fourier transform of the fringe pattern recovers the spectrum, which is shown to the left of the fringe pattern.

including detection of various cancers,[13-18] atmospheric measurement,[19] measurements of food and beverages,[20] explosives detection,[21] and absorption and fluorescence spectroscopy.[22] Despite these numerous applications of cell phone technology to scientific study, including some forms of spectroscopy, the authors are unaware of any peer-reviewed published work employing a cell phone camera as a detector for Raman spectroscopy.

This chapter describes experiments performed with a millimeter-sized SHRS and a standard cell phone camera as a detector with no intermediate optics other than the optics built into the cell phone. The experiments were also repeated using the same miniature SHRS, with high quality imaging optics, and a high-quality CCD to function as a comparison to a more typical spectrometer setup.

4.2 EXPERIMENTAL

The SHRS was constructed using a 5 mm cube beamsplitter (Model #: BS007, Thorlabs Inc., Newton, New Jersey, USA) and 25.4 mm square 300 grooves/mm diffraction gratings (Model #: GR25-0305, Thorlabs Inc., Newton, New Jersey, USA) which were masked with black anodized aluminum foil placed over the grating to allow only a 2.5 mm wide hexagonal area to be illuminated. This provides a system resolving power of ~ 1070 as described in detail below. The distance between the diffraction gratings and beamsplitter was limited by the commercially available mechanical mounts used, ~ 30 mm from the surface of the grating to the nearest face of the beamsplitter. Sample light was collected with a 25.4 mm diameter f/2 lens (L_1 in Figure 4.1) placed one focal length from the sample to collimate collected light into the SHRS. Stray laser light and Rayleigh scattered light were blocked using two 532 nm razor-edge, long-pass

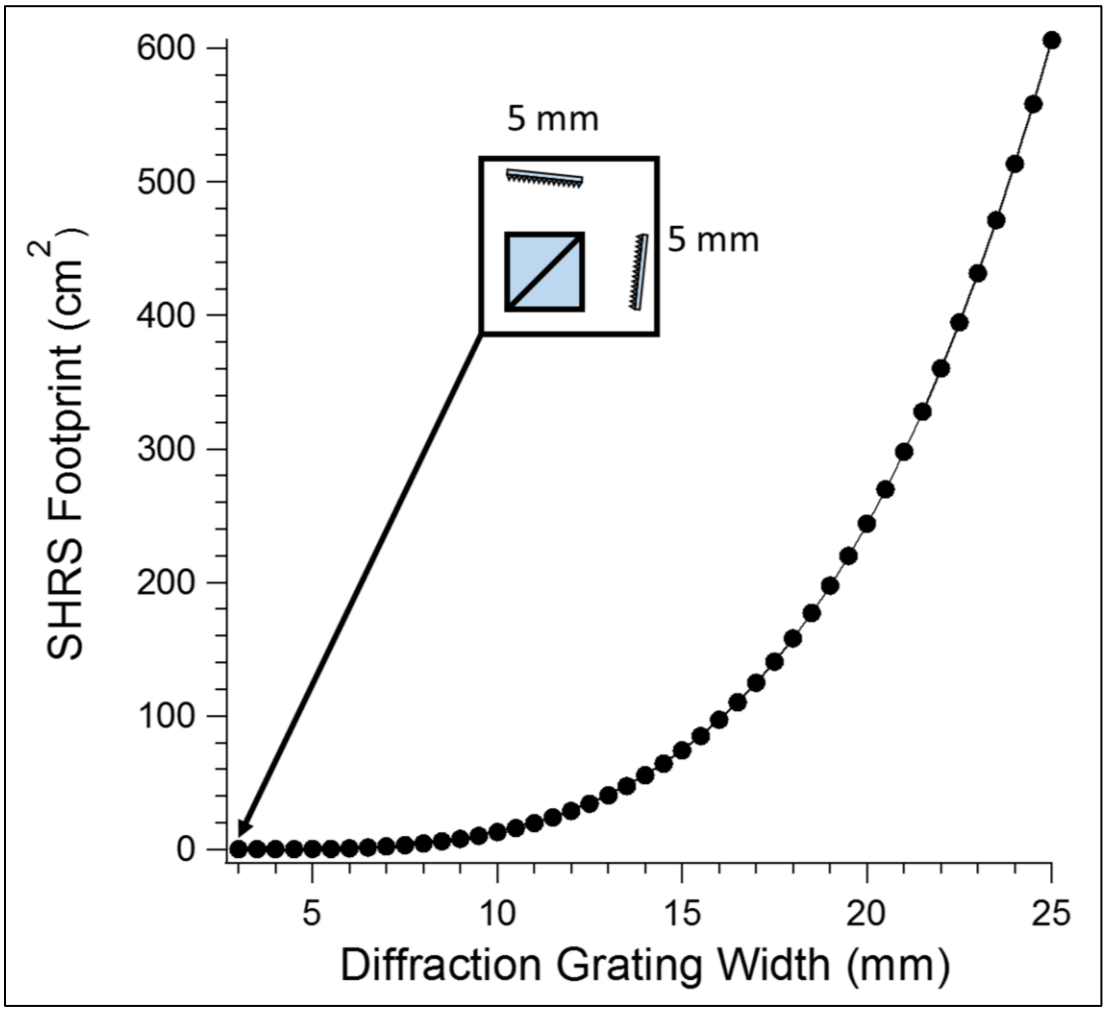

Figure 4.2: As the diffraction gratings of the SHRS are decreased in size the gratings can be placed closer to the beamsplitter without overlap from adjacent diffraction orders, which can degrade interferogram quality, thus decreasing the footprint of the system. The inset diagram shows the 5x5 mm footprint of the smallest footprint point on the plot.

filters (Semrock LP03-532RE-25, Rochester, New York, USA) placed in the collimated beam in front of the SHRS (F in Figure 1(a)), tilted to allow > 50 cm^{-1} Raman shifted light to pass into the SHRS.

The cell phone used was a standard LG G4 (LG Electronics, Youngdungpo-gu, Seoul, Korea) which has f/1.8 optics, a 5312x2988 pixel sensor with 1.12 μm pixel pitch, exposure times ranging from 1/6000 s to 30 s, and is capable of saving images in a RAW format. The optics of the cell phone camera have a short enough focal length to allow the face of the gratings to be imaged with the cell phone placed ~ 25 mm from the Beamsplitter, giving ~ 0.08 magnification, estimated by the number of pixels of the cell phone illuminated and the 1.12 μm pixel pitch. The imaging lens used to couple the SHRS to the CCD was a Nikon 80-200 f/4.5-5.6 D (Nikon Corporation, Tokyo, Japan) set up to image the plane of the grating face onto the CCD with ~ 2.6 magnification, estimated in the same manner as the cell phone, to illuminate as many pixels a possible, thus providing a larger spectral range. The CCD used was a Pixis 400 (Princeton Instruments, Trenton, New Jersey, USA) which has a 1340x400 pixel sensor with 20 μm pixel pitch, thermoelectrically cooled to -70 ºC. The CCD output was 16-bit, providing a total of 65,536 possible different values for each pixel.

A 532 nm variable-power CW laser with a maximum power of 300 mW (Model #: MLL-III-532, Opto Engine LLC, Midvale, Utah, USA) was used for sample excitation. The laser was set to ~ 100 mW and focused onto the samples using a 25.4 mm diameter f/16 lens giving a spot size on the sample of several hundred microns. The collection solid angle of the SHRS, according to Equation 4.1, is ~5.9×10^{-3} sr, giving an angular field of view of the SHRS of about 2.1°.

$$\Omega = \frac{2\pi}{R} \qquad \text{Eqn. 4.1}$$

Powder samples of high-purity sulfur (J.T. Baker Chemical, item number: 4088-1), potassium perchlorate (Sigma-Aldrich, ≥ 99% purity, item number: 241830), sodium sulfate (EM Science, item number: SX0761-1), and ammonium nitrate (Sigma-Aldrich, 99.999% purity, item number: 256064) were pressed into pellets using a 10 ton pellet press. This provided compact samples without need for sample containment.

4.3 RESULTS & DISCUSSION

The SHRS can be miniaturized by reducing the widths of the beamsplitter and diffraction gratings which allows the gratings to be placed closer to the beamsplitter. The distance between the diffraction grating and the beamsplitter is theoretically limited by the distance at which adjacent diffraction orders overlap the diffraction order of interest on the detector. Overlap of adjacent diffraction orders with the diffraction order of interest can generate additional, unwanted interference patterns which degrade the recovered interference pattern formed by the diffraction order of interest. One method to eliminate diffraction order overlap as the diffraction gratings move closer to the beamsplitter is to increase diffraction grating groove density, which increases the angular distance between diffraction orders. The resolving power of the SHRS is limited by the number of grooves of the diffraction grating illuminated as indicated by Equation 4.2:

$$R = 2WD \qquad \text{Eqn. 4.2}$$

Where R is the resolving power, W is the width of the diffraction gratings, and D is the groove density of the diffraction gratings. As the diffraction grating width is decreased, higher groove density gratings must be used to maintain the same resolving power. Thus, as the diffraction diffraction gratings are moved closer to the beamsplitter and the widths

of the diffraction gratings and beamsplitter are decreased for miniaturization, diffraction grating groove density must increase to avoid order overlap which compensates for the resolving power that would be lost by using smaller gratings with constant groove density. The result is an exponential decrease in SHRS footprint as the size of the diffraction grating is decreased as shown in Figure 4.2. When the diffraction grating groove density increases to a point at which the angle of diffraction orders adjacent to the diffraction order of interest is 90°, allowing the diffraction gratings to be placed arbitrarily close to the beamsplitter. At this point the physical size of the beamsplitter and diffraction gratings is the limiting factor in the miniaturization of the SHRS. The inset of Figure 4.2 indicates the SHRS footprint for 90° adjacent diffraction order, however this is only the point at which the diffraction gratings can be placed arbitrarily close to the beamsplitter, not the theoretically smallest SHRS footprint. The SHRS described in this work has a footprint > 20 times smaller than our previously published SHRS.[1-5]

Although cell phone cameras have made great strides in sensor and optical quality, there are features, which degrade their function as a spectroscopic detector. Chief among these features is the color filter array (CFA) used in color detectors which allows the interpolation of the colors of the objects imaged. Briefly, the CFA is a grid of color filters overlaid on top of the sensor chip, each filter allowing only one range of wavelengths to pass to the pixel underneath. Each pixel then only detects light roughly correlating to the wavelength range corresponding to red, green, or blue. Figure 4.3 demonstrates a typical CFA arrangement on the left and the color-specific pattern observed by the sensor. Demosaicing algorithms are applied to the raw sensor output to interpolate the color detected by each group of pixels and an RGB value is assigned to

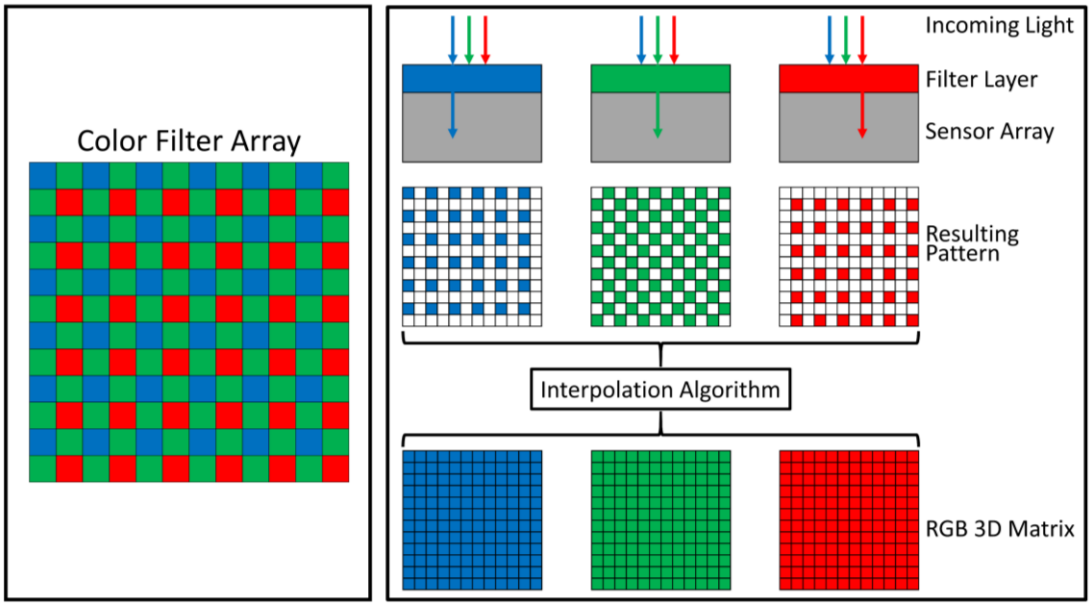

Figure 4.3: Left: one of the most common arrangements of filters within color filter arrays (CFA). Right: each color within the filter array transmits only wavelengths of light corresponding to red, green, or blue. The mosaic generated on the sensor by the CFA is then interpolated with a demosaicing algorithm, resulting in an RGB value for each pixel.

each pixel. While this process allows color images to be obtained, spatial resolution is reduced due to the interpolation process and sensitivity is reduced due to most of the light impingent upon a given pixel being filtered out. In the case of the SHRS, the spectral information of the light impingent upon the sensor is encoded in the Fourier domain of the spatial interference pattern. The light rejection of the CFA throws away light unnecessarily when used as a detector for the SHRS. CCDs commonly used as detectors for spectrometers, like the Pixis CCD used in this work, are monochrome detectors and do not have a CFA.

One of the primary reasons for choosing the particular cell phone used in these experiments is the ability to save images in the RAW file format. The RAW image format is digital negative (DNG), which saves the raw sensor output without applying any white balancing, smoothing, or sharpening algorithms. The DNG image, when properly processed, produces a more accurate representation of the sensor readout than the JPG format typically employed by most other cell phone cameras, which involves compression algorithms which discard data to minimize file size. The RAW format image output of the cell phone is 10-bit, providing a total of 1024 different possible values for each pixel. DNG images were imported and processed using a MATLAB program designed to extract relevant information from the file metadata, linearize the raw sensor data based on information extracted from the file metadata, apply color balance multipliers from the metadata in the appropriate RGB format corresponding to the CFA layout specific to the sensor, and apply the demosaicing algorithm.[23] Raman spectra were recovered by applying the FFT to each row of the image individually instead of summing all the rows and then applying the FFT. The individual row FFT outputs were then

summed to recover the final spectrum. This method of performing the FFT in a piecewise manner corrects for many imperfections in the fringe images.

Scientific-grade CCDs are typically cooled (-70 ºC with thermoelectrical coolers or -120 ºC with liquid nitrogen) which significantly reduces thermal noise within the sensor chip. Cell phone cameras operate at or above ambient temperature and thus have a significantly higher noise floor than a CCD. Furthermore, the readout electronics in CCDs have been designed specifically to be very low noise. Analogue-to-digital conversion in CCD sensors is a linescan process in which conversion to the digital domain is handled on a pixel-by-pixel basis which causes a bottleneck in data readout. Analogue-to-digital conversion in CMOS sensors, which are the most common sensor type in cell phones, is a parallel process in which each pixel is converted to the digital domain on-chip before readout. This fundamental difference in operation allows analogue-to-digital conversion in CMOS sensors to occur much faster than CCDs.

The miniature SHRS system described is far from optimal. The 25.4 mm diameter f/2 lens collection lens used produces a collimated beam 10 times larger than the size of the masked diffraction gratings and as a result ~ 99% of the light collected is lost. This can be avoided by using a 2.5 mm diameter, f/2 collection lens. Also, the grating masks were not cut with high precision or aligned precisely, and were punched using an Allen wrench, and the hexagonal shape lead to reduced spectral resolution. The use of a 2.5 mm rectangular grating mask would result in a resolving power of 1500, according to Equation 4.2. However, variations in width, and thus the number of illuminated grooves, results in a resolving power of ~ 1070, resulting in a theoretical resolution of 17.5 cm^{-1} for the hexagonal mask. Although the throughput and spectral resolution of the SHRS

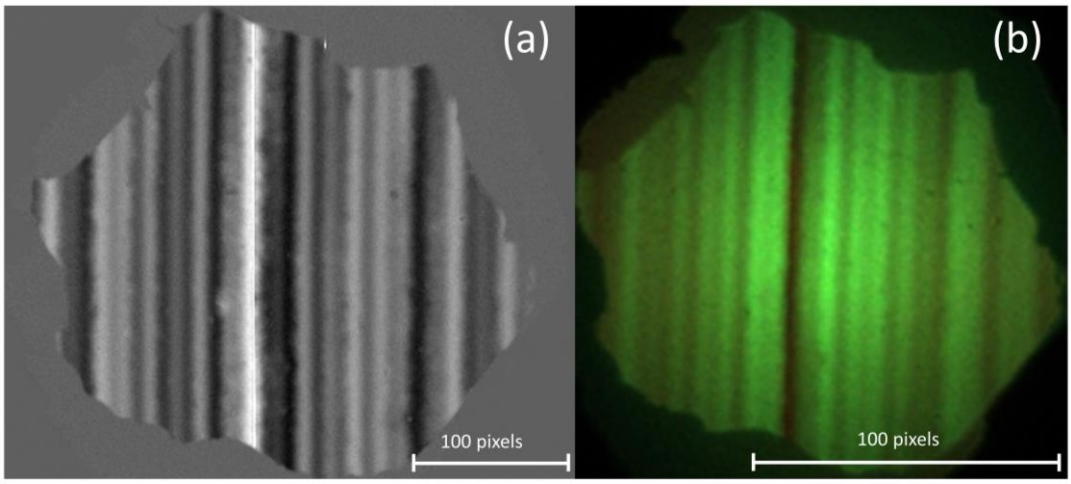

Figure 4.4: Comparison of sulfur fringe patterns captured by two different detectors. (a) Sulfur Raman fringe image collected with high quality imaging optics and a PI Pixis CCD, (b) sulfur Raman fringe image collected with the cell phone with no intermediate optics.

could be considerably improved, the performance of the system was still adequate to measure good quality Raman spectra of a variety of samples using a cell-phone camera.

Figure 4.4 shows fringe images of sulfur Raman captured by the CCD (Figure 4.4a) and the cell phone (Figure 4.4b). The shape of the images is due to the hexagonal diffraction grating masks used, one of which was slightly off-axis with respect to the other grating mask, leading to the irregular, non-hexagonal shape. Examination of the fringe images captured by the Pixis CCD, Figure 4.4a, and by the cell phone, Figure 4.4b, shows an identical fringe pattern, though the fringes captured by the CCD indicate a significantly higher fringe contrast. The Pixis CCD is a 16-bit sensor, which allows a significantly greater number of possible values for each pixel than the 10-bit sensor of the cell phone, which allows the CCD to register more precise intensity values for each pixel of the interference pattern. The CCD, unlike the cell phone, is thermoelectrically cooled and has electronic specifically designed to be low noise. This allows the CCD to produce a more accurate, much lower noise image than the cell phone, which leads to an improved interference pattern fringe contrast. Each image contains a scale bar, which indicates the size of 100 pixels for each detector. The number of pixels in the axis perpendicular to the fringes limits the spectral range. For the cell phone camera at the magnification used, ~ 180 pixels were illuminated in the horizontal direction when imaging the 2.5 mm diffraction gratings, whereas for the CCD ~ 320 pixels were illuminated giving the CCD a larger spectral range. The cell phone sensor has such a large number of pixels (5312 in the horizontal direction, providing 2656 resolvable fringes) that if the entire width of the chip were illuminated the highest spatial fringe frequency that could be recovered by the cell phone sensor, limited by the Nyquist

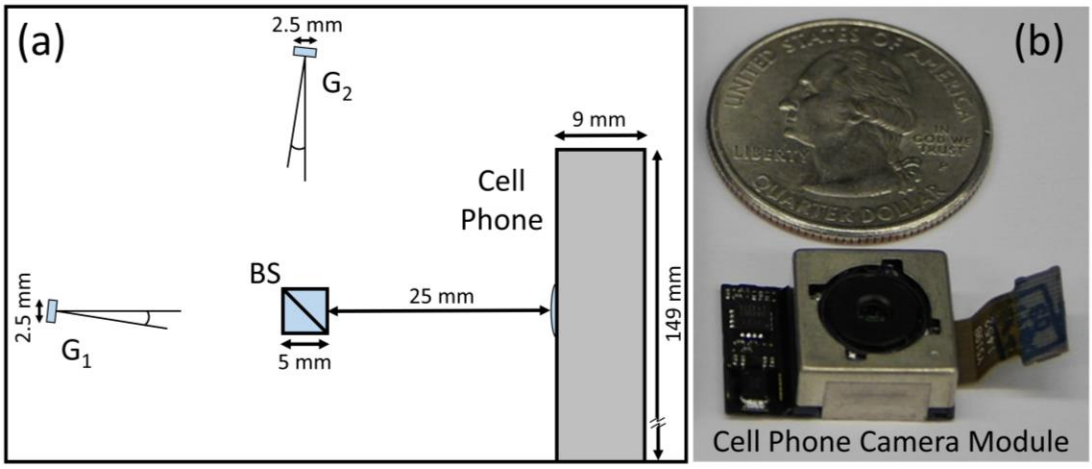

Figure 4.5: Demonstration of the size of the miniature SHRS. (a) a to-scale diagram of the SHS with the cell phone as a detector, (b) the cell phone camera module removed from the cell phone with a US quarter dollar for size comparison.

criterion and the pixel pitch, according to Equation 4.3 would provide a theoretical spectral range of ~ 14,000 cm^{-1}, far larger than is useful for Raman Spectroscopy.

$$f = 4(\sigma - \sigma_L)tan\theta \qquad \text{Eqn. 4.3}$$

Figure 4.5a shows a to-scale diagram of the SHRS with the cell phone as a detector. The cell phone, though orders of magnitude smaller than a typical scientific-quality CCD is still significantly larger than the SHRS. Figure 4.5b shows the cell phone camera module with the focusing lens, removed from the cell phone next to a US quarter for scale. Higher quality array detectors of such a small form factor would pair perfectly with a miniature SHRS.

Sulfur Raman spectra are shown in Figure 4.6, measured with the Pixis CCD with a 250 ms exposure time (Figure 4.6a) and with the cell phone with a 33 ms exposure time (Figure 4.6b). The insets show interferograms generated by summing all rows of the fringe images. Although the cell phone has a relatively large range of possible exposure times, the exposure time can only be chosen from a pre-defined list, and 33 ms was the longest exposure time available that could be used without saturating the sensor. The signal-to-noise ratio (SNR) of the 473 cm^{-1} band is 344 with the CCD and 18 with the cell phone, about a 20 fold difference. SNR was estimated as the ratio of the baseline subtracted intensity of the indicated peak to the standard deviation of a region of the spectrum where no peaks are present. However if the exposure time is taken into account the SNR of the CCD spectrum is about 7 times higher than the cell-phone camera spectrum. The resolution of the 473 cm^{-1} band is ~ 43 and 55 $cm^{-1}$for the CCD and cell-phone camera, respectively. This is about 2-3 times worse than the theoretical 17.5 cm^{-1} resolution, likely the result of imperfect focusing and non-overlapping images of the

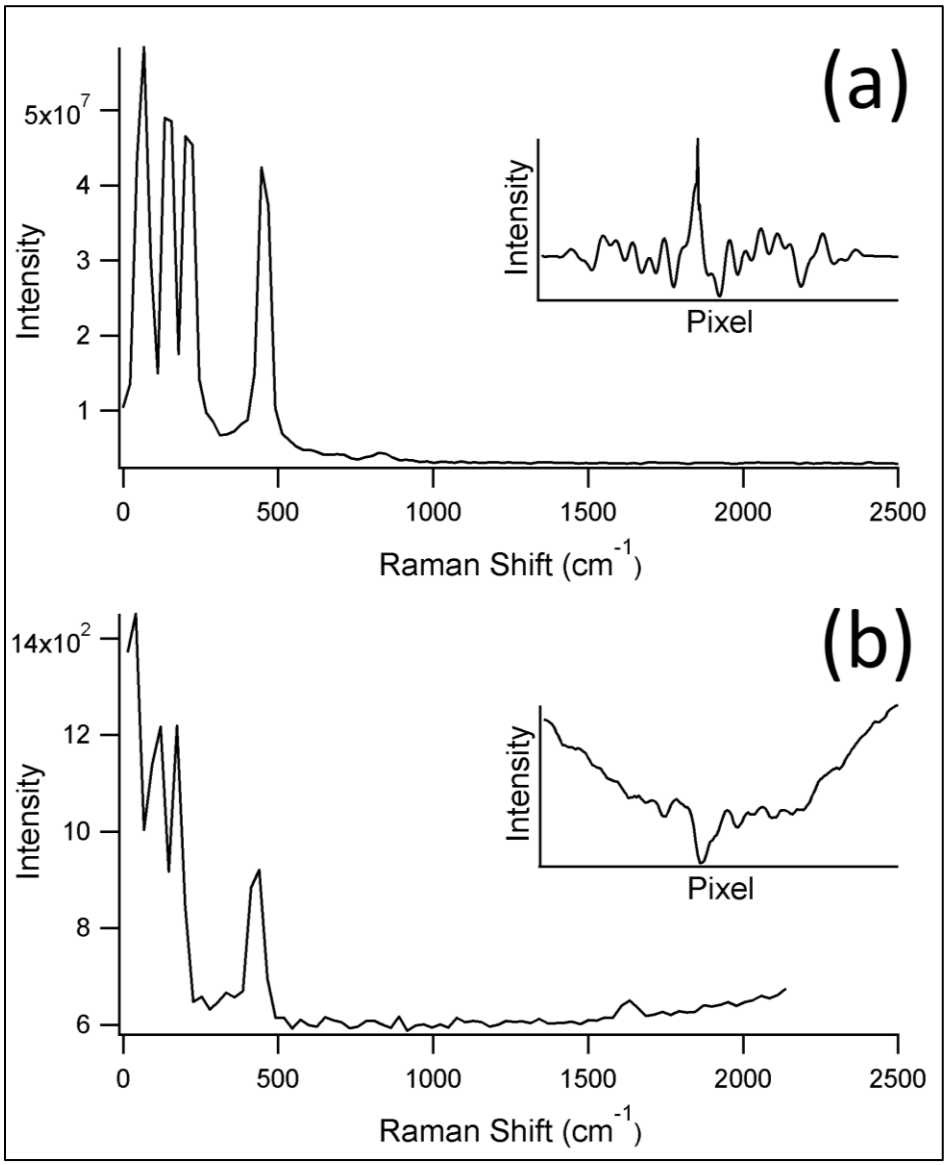

Figure 4.6: Sulfur Raman spectrum measured with (a) the PI Pixis CCD at 250 ms exposure time, signal to noise ratio of the 473 cm^{-1} sulfur band is 344 and (b) the cell phone at 33 ms exposure, signal to noise ratio of the 473 cm^{-1} sulfur band is 18. Inset in each spectrum is the corresponding interferogram, which is obtained by summing all of the rows of the fringe image.

grating masks. Focusing is more critical with the cell phone camera because with the very low magnification used (~ 0.08), interference fringes are sampled by fewer fringes. In fact, for a 1000 cm^{-1} band, the fringe spacing would be ~ 5 μm on the cell phone camera but ~ 160 μm on the CCD because of the much larger magnification used with the CCD optics. The biggest difference in the spectra is in the low wavenumber region where the 85 cm^{-1}, 154 cm^{-1}, and 219 cm^{-1} bands[24] sit on a sloped, low-wavenumber baseline. This could be due to the low number of pixels illuminated on the cell phone sensor which may inhibit the ability to discriminate the low spatial frequency fringes generated by these low wavenumber Raman bands. The significantly lower fringe contrast provided by the cell phone seen in Figure 4.4 may have blurred the low spatial frequency fringes together, lowering the low wavenumber resolution of the Fourier transform. The spatial resolution (line pairs/mm) and modulation transfer function (MTF) of the cell phone camera optics used in this work are unknown, however, it is likely that the optical quality is lower than the high quality imaging lens used with the CCD leading to reduced fringe contrast and reduced spectral resolution.

Potassium perchlorate spectra are shown in Figure 4.7, obtained with the CCD (Figure 4.7a) and the cell phone (Figure 4.7b). A 2 s exposure time was used for both detectors. The resolution of the 941 cm^{-1} band is 39 and 38 cm^{-1} for the CCD and cell phone camera, respectively. The signal-to-noise ratio of the 941 cm^{-1} band is 109 for the CCD and 37 for the cell phone. This SNR difference is only a factor of 3, unlike the case of sulfur where the SNR difference was a factor of 7. The relative intensities of the bands is noticeably different between the spectra. The relative intensities of the 461 cm^{-1} and 631 cm^{-1} band are approximately the same between the two spectra, however, the relative

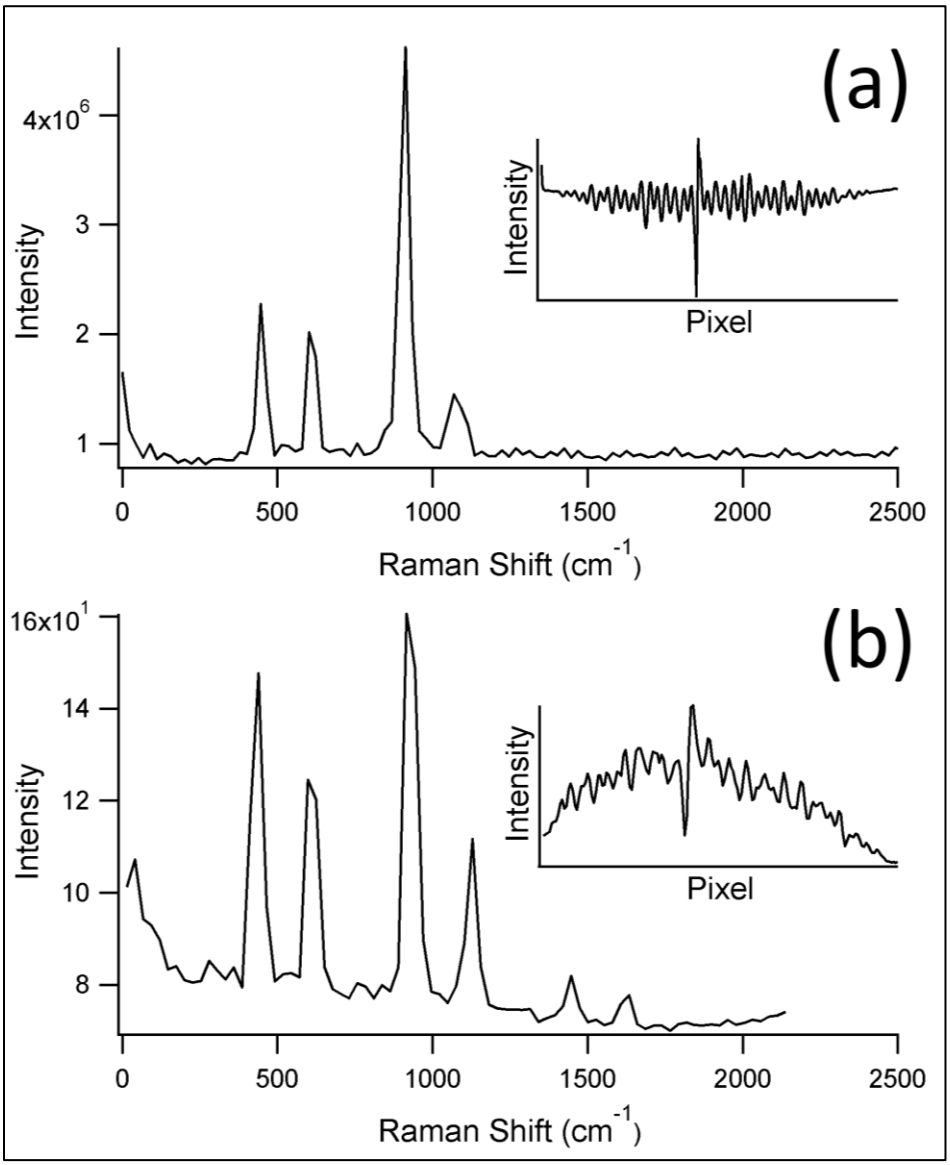

Figure 4.7: Potassium perchlorate Raman spectrum measured with (a) the PI Pixis CCD at 2 s exposure time, signal to noise ratio of the 941 cm^{-1} perchlorate band is 109 and (b) the cell phone at 2 s exposure, signal to noise ratio of the 941 cm^{-1} perchlorate band is 37. Inset in each spectrum is the corresponding interferogram, which is obtained by summing all of the rows of the fringe image.

intensities of the 941 cm^{-1} and 1085 cm^{-1} bands are considerably different. The spectrum produced by the CCD has the same relative peak intensity as has been previously reported for potassium perchlorate[25] whereas the cell phone spectrum has lower peak intensities around the 1000 cm^{-1} region relative to the lower wavenumber bands. This is likely due to the wavelength-dependent transmission efficiencies of the color filters of the CFA. The CFA, like any filter, does not have a perfectly square transmission profile for each "color" so it is likely that the bands around ~ 1000 cm^{-1} Raman shift, which would be ~ 560 nm for 532 nm excitation, have a lower transmission efficiency through the CFA than the lower Raman shift bands. At first glance this explains why the intense 941 cm^{-1} band has a significantly lower relative intensity with the cell phone, but it does not explain why the 1085 cm^{-1} has a higher relative intensity than seen in the CCD spectrum. However, it may be possible that while the 941 cm^{-1} band is at a wavelength with a lower transmission for the "green" pixels, the 1085 cm^{-1} band may be at a wavelength which is the overlap of the transmission profiles of the "green" and "red" pixels, thus appearing to have a higher relative intensity.

Figure 4.8a is the Raman spectrum of ammonium nitrate obtained with the CCD and Figure 4.8b is the same sample obtained with the cell phone, both with a 2 s exposure time. Ammonium nitrate has a strong, low wavenumber phonon band which can be seen in each spectrum due to the fact that the long pass filters used for laser rejection allow this phonon band to pass into the SHRS. The other prominent spectral feature is the 1040 cm^{-1} band. There appears to be a small band in both spectra where the 712 cm^{-1} band is expected,[26] however this is a very low intensity band and is likely to be swamped by the noise distribution effects of the two intense bands. As Figure 4.7 showed with potassium

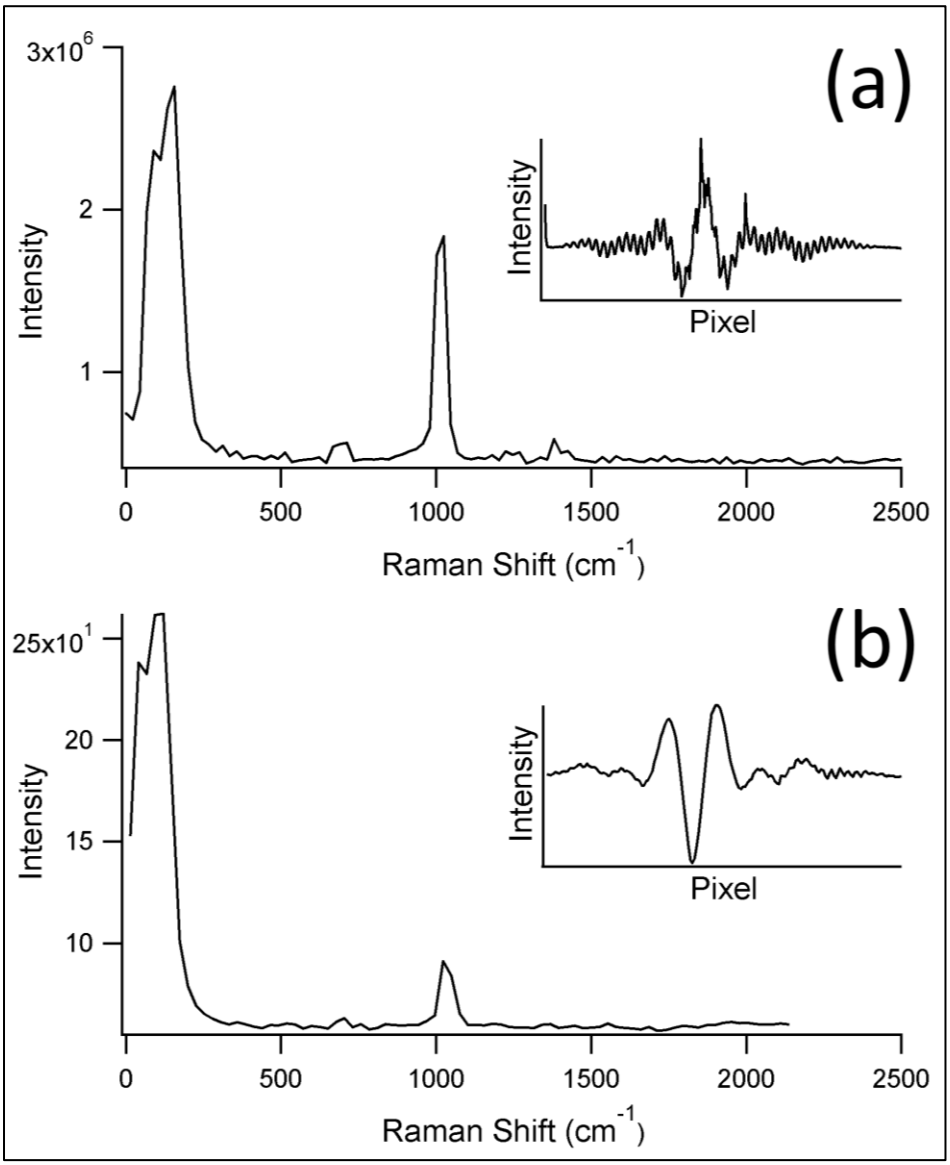

Figure 4.8: Ammonium nitrate Raman spectrum measured with (a) the PI Pixis CCD at 2 s exposure time, signal to noise ratio of the ~ 1000 cm^{-1} nitrate band is 117 and (b) the cell phone at 2 s exposure, signal to noise ratio of the ~ 1000 cm^{-1} nitrate band is 12. Inset in each spectrum is the corresponding interferogram, which is obtained by summing all of the rows of the fringe image.

perchlorate, ammonium nitrate shows a significant decrease in relative intensity for the band around 1000 cm^{-1}, likely due to a lower transmission efficiency of the CFA around this wavelength. The signal-to-noise ratio of the 1040 cm^{-1} band of the CCD spectrum is 117 and for the cell phone spectrum is 12, a factor of about 10 different. In this respect the SNR difference is more like the sulfur spectra than the perchlorate spectra.

The spectrum of sodium sulfate obtained with the CCD with a 2 s exposure time is shown in Figure 4.9a and with the cell phone with a 2 s exposure is shown in Figure 4.9b. The signal-to- noise ratio of the 992 cm^{-1} band for the CCD spectrum is 36 and for the cell phone spectrum is 16, only a factor of ~2 difference. As with Figures 4 and 5, a similar decrease in relative peak intensity around 1000 cm^{-1} can be seen with sodium sulfate. However, unlike other samples, with sodium sulfate it appears as though there are two bands in the 400-600 cm^{-1} range, which are prominent in the cell phone spectrum but are more or less buried in the noise of the CCD spectrum. For solid sodium sulfate we would expect to see bands at 449, 466, 620, 632, and 647 cm^{-1} in this region of the spectrum,[27] however the resolution of this miniature SHRS is so low that the 449 and 466 cm^{-1} are indistinguishable as are the 620, 632, and 647 cm^{-1} bands. In the SHRS, the noise of every spectral feature is distributed throughout the spectrum, known as the multiplex disadvantage,[8] which means that it is possible for the noise of a very intense spectral feature to overwhelm lower intensity spectral features. It is likely that, due to the wavelength specific transmission profiles of the cell phone CFA partially filtering the intense sulfate 992 cm^{-1} band, it contributes less noise to the weaker bands.

The large SNR difference for ammonium nitrate as opposed to the much smaller difference for perchlorate and sulfate can be explained by the spectral response of the

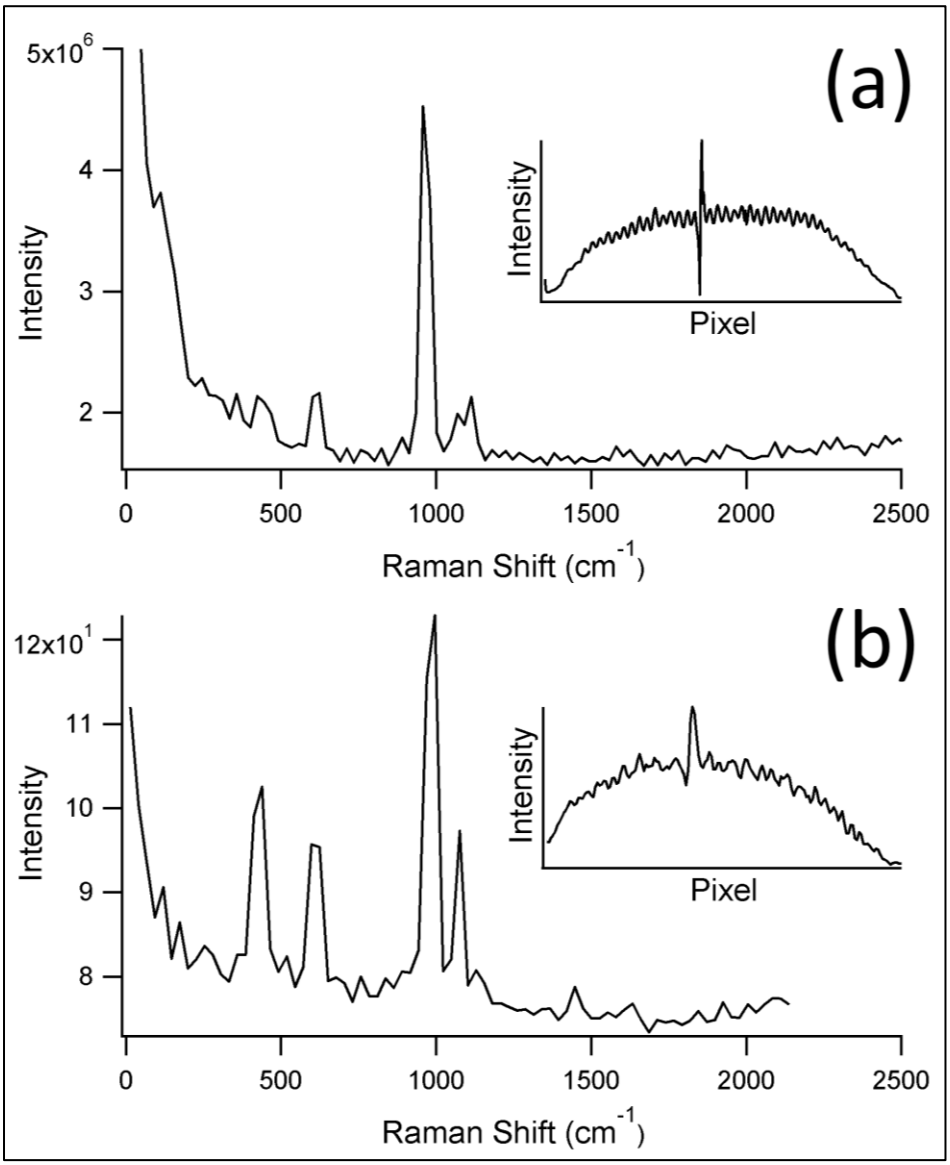

Figure 4.9: Sodium sulfate Raman spectrum measured with (a) the PI Pixis CCD at 2 s exposure time, signal to noise ratio of the ~ 1000 cm^{-1} sulfate band is 36 and (b) the cell phone at 2 s exposure, signal to noise ratio of the ~ 1000 cm^{-1} sulfate band is 16. Inset in each spectrum is the corresponding interferogram, which is obtained by summing all of the rows of the fringe image.

CFA on the cell phone camera. The total spectral response of the CFA changes rapidly in the 1000 cm^{-1} region as the green filter transmission rapidly decreases and the red filter increases.[28] The net effect is a dip in spectral response right around 1000 cm^{-1}, complicated by the fact that there are twice as many green filters as red. For perchlorate and sulfate, where the SNR was similar, the bands used were both below 1000 cm^{-1}, whereas for ammonium nitrate the band used to calculate SNR was above 1000 cm^{-1} in a region where the green filter transmission drops rapidly. The reason for the large difference in SNR for the sulfur spectra is not clear.

The fringe patterns captured by the cell phone camera in Figure 4.10 provides strong support for the explanation that the decreased spectral intensity ~ 1000 cm^{-1} Raman shift is due to the transmission profile of the CFA. Figure 4.10a shows the cell phone fringe pattern for sulfur. The green color of the fringe pattern is due to the 532 nm excitation laser, which is green, and the low wavenumber shifts of the sulfur Raman bands observed. The fringe pattern generated by perchlorate is shown in Figure 4.10b. The spectrum of perchlorate obtained with the CCD (Figure 4.7a) shows that the 941 cm^{-1} band is far stronger than all other Raman bands observed and the lower Raman shifted bands, although much weaker, appear at Raman shifts higher than the longest Raman shifted band of sulfur. The color image of the perchlorate fringe pattern shown in Figure 4.10b appears not as the bright green of the sulfur, but rather as a reddish-yellow, indicating that a large portion of the Raman bands are passing through the "red" portions of the CFA. The cell phone fringe image of sulfate is shown in Figure 4.10c. The spectrum of sulfate obtained with the CCD (Figure 4.9a) indicates the presence of a large Raman band ~ 1000 cm^{-1} and relatively high Raman shifted bands for even the lowest

wavenumber bands within the spectrum, much like perchlorate. The cell phone fringe image of sulfate in Figure 4.10c appears as a reddish-yellow, much like perchlorate, indicating a large portion of the Raman bands passing through the CFA. The problems associated with the transmission profiles of the CFA can, of course, be avoided by use of a monochromatic detector, such as the CCDs commonly used with spectrometers. However, if the use of stock cell phone components is desired, there are methods that can be employed to combat the effects of the CFA. The CFA can be removed from the surface of the sensor, however complete removal of the CFA can be difficult and the procedures involved have a high probability of permanently damaging the sensor. Alternatively, it may be possible to perform radiometric measurements to determine the spectral transmission profiles of a particular CFA and apply a corresponding weighted mask in post-processing during the demosaicing process to compensate for the relative peak intensity problem. However, this latter method does nothing to help the actual transmission of photons to the sensor surface which may prove to be problematic for low intensity bands that happen to fall in a low-transmission portion of the CFA transmission spectrum. Lastly, it is possible to change the excitation wavelength which would shift the Raman bands into a different region of the CFA transmission spectrum, allowing for measurement of low-intensity bands through a high-transmission portion of the CFA.

4.4 CONCLUSIONS

This chapter has demonstrated a standard cell phone camera as a detector for a millimeter-sized spatial heterodyne Raman spectrometer. A scientific-grade CCD with high-quality imaging optics was also used as a detector for the same SHRS as a comparison of a more traditional Raman spectrometer. Despite the significantly higher

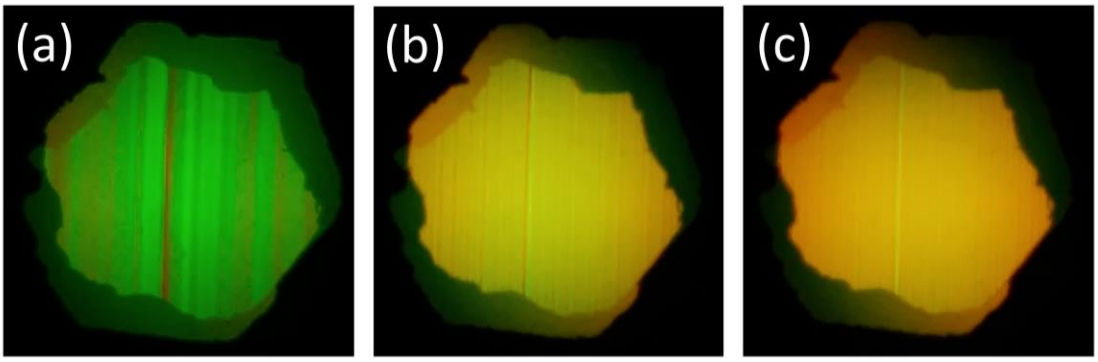

Figure 4.10: The color fringe patterns captured by the cell phone camera: (a) sulfur, (b) potassium perchlorate, and (c) sodium sulfate.

noise and lower sensitivity of the cell phone camera sensor, the high light throughput and multiplex advantage inherent to the SHRS design allowed Raman spectra to be measured, in some cases with SNR only 2-3 times worse than using a scientific grade CCD. The spectral resolution of the miniature SHRS was 2-3 times worse than predicted. This is likely due to a poor choice of imaging optics and low magnification (0.08 in the case of the cell phone camera), imperfect focusing, and low optical quality of the imaging lenses. These issues are easily addressed by more careful design choice of imaging optics. Combining this system with a diode laser excitation source could be a path toward miniature high throughput Raman spectrometers.

REFERENCES

(1) N.R. Gomer, C.M. Gordon, P. Lucey, S.K. Sharma, J.C. Carter, S.M. Angel. "Raman Spectroscopy Using a Spatial Heterodyne Spectrometer: Proof of Concept". Appl. Spectrosc. 2011. 65(8): 849–857.

(2) N. Lamsal, S.M. Angel. "Deep-Ultraviolet Raman Measurements Using a Spatial Heterodyne Raman Spectrometer (SHRS)". Appl. Spectrosc. 2015. 69(5): 525–534.

(3) N. Lamsal, S.M. Angel, S.K. Sharma, T.E. Acosta. "Visible and UV Standoff Raman Measurements in Ambient Light Conditions Using a Gated Spatial Heterodyne Raman Spectrometer". Paper presented at: LPSC 2015. Woodland TX; March 16-20.2015.

(4) N. Lamsal, S.K. Sharma, T.E. Acosta, S.M. Angel. "Stand-off UV and Visible Raman Measurements Using a Gated Spatial Heterodyne Raman Spectrometer". Appl. Spectrosc. 2016. 70(4): 666-675.

(5) K.A. Strange, K.C. Paul, S.M. Angel. "Transmission Raman Measurements using a Spatial Heterodyne Raman Spectrometer (SHRS)". Appl. Spectrosc. Published online before print June 30, 2016. doi: 10.1177/0003702816654156.

(6) I.B. Gornushkin, B.W. Smith, U. Panne, N. Omenetto. "Laser-Induced Breakdown Spectroscopy Combined with Spatial Heterodyne Spectroscopy". Appl. Spectrosc. 2014. 68(9): 1076-1084.

(7) P.D. Barnett, N. Lamsal, S.M. Angel. "Standoff LIBS using a Miniature Wide Field of View Spatial Heterodyne Spectrometer with Sub-Microsteradian Collection Optics". Appl. Spectrosc. Paper in press 2016.

(8) J.M. Harlander. Spatial Heterodyne Spectroscopy: Interferometric Performance at Any Wavelength without Scanning. [Ph.D. Dissertation]. Madison, Wisconsin: University of Wisconsin-Madison, 1991.

(9) J.M. Harlander, F.L. Roesler, R.J. Reynolds, K. Jaehnig, W.A. Sanders. "Differential, Field-Widened Spatial Heterodyne Spectrometer for Investigations at High Spectral Resolution of the Diffuse Far Ultraviolet 1548 Å Emission Line from the Interstellar Medium". Proc. SPIE. 1993. 2006: 139-148.

(10) J.M. Harlander, F.L. Roesler, S. Chakrabarti. "Spatial Heterodyne Spectroscopy: A Novel Interferometric Technique for the FUV". In: O. H. W. Siegmund; H. S. Hudson, editors. EUV, X-Ray, and Gamma-Ray Instrumentation for Astronomy. Proc. SPIE. 1990. 1344: 120-131.

(11) S. Ayas, A. Cupallari, O.O. Ekiz, Y. Kaya, A. Dana. "Counting Molecules with a Mobile Phone Camera Using Plasmonic Enhancement". ACS Photonics. 2014. 1: 17-26.

(12) Q. Wei, H. Qi, W. Luo, D. Tseng, S.J. Ki, Z. Wan, Z. Göröcs, L.A. Bentolila, T.T. Wu, R. Sun, A. Ozcan. " Fluorescent Imaging of Single Nanoparticles and Viruses on a Smart Phone". ACS Nano. 2013. 7(10): 9147-9155.

(13) S. Wang, X. Zhao, I. Khimji, R. Akbas, W. Qiu, D. Edwards, D.W. Cramer, B. Ye, U. Demirci. "Integration of Cell Phone Imaging with Microchip ELISA to Detect Ovarian Cancer HE4 Biomarker in Urine at the Point-of-Care". Lab Chip. 2011. 11(20): 3411-3418.

(14) A. Das, T. Swedish, A. Wahi, M. Moufarrej, M. Nolad, T. Gurry, E. Aranda-Michel, D. Aksel, S. Wagh, V. Sadashivaiah, X. Zhang, R. Raskar. Mobile phone based mini-spectrometer for rapid screening of skin cancer". In: M.A. Druy, R.A. Crocombe, D.P. Bannon, editors. Next-Generation Spectroscopic Technologies VIII. Proc. SPIE. 2015. 9482.

(15) Z.J. Smith, K. Chu, A.R. Espenson, M. Rahimzadeh, A. Gryshuk, M. Molinaro, D.M. Dwyre, S. Lane, D. Matthews, S. Wachsmann-Hogiu. "Cell-Phone-Based Platform for Biomedical Device Development and Education Applications". PLoS ONE. 2011. 6(3): e17150.

(16) K.D. Long, H.J. Yu, B.T. Cunningham. "Smartphone spectroscopy: three unique modalities for point-of-care testing". In: M.A. Druy, R.A. Crocombe, D.P. Bannon, editors. Next-Generation Spectroscopic Technologies VIII. Proc. SPIE. 2015. 9482.

(17) J. Jiang, X. Wang, R. Chao, Y. Ren, C. Hu, Z. Xu, G.L. Liu. "Smartphone based portable bacteria pre-concentrating microfluidic sensor and impedance sensing system". Sensors and Actuators B. 2014. 193: 653-659.

(18) M.W. Kadlec, D. You, J.C. Liao, P.K. Wong. "A Cell Phone-Based Microphotometric System for Rapid Antimicrobial Susceptibility Testing". J. Lab. Autom. 2014. 19(3): 258-266.

(19) T. Cao, J.E. Thompson. "Remote Sensing of Atmospheric Optical Depth Using a Smartphone Sun Photometer". PLoS ONE. 2014. 9(1): e84119.

(20) Z. Iqbal, R.B. Bjorklund. "Assessment of a mobile phone for use as a spectroscopic analytical tool for foods and beverages". Int. J. Food Sci. Tech. 2011. 46: 2428-2436.

(21) A.S. Finch, M. Coppock, J.R. Bickford, M.A. Conn, T.J. Proctor, D.N. Stratis-Cullum. "Smart phones: platform enabling modular, chemical, biological, and explosives sensing". In: A. W. Fountain, editor. Chemical, Biological, Radiological, Nuclear, and Explosives (CBRNE) Sensing XIV. Proc. SPIE. 2013. 8710: 87100D-1.

(22) M.A. Hossain, J. Canning, K. Cook, S. Ast, P.J. Rutledge, A. Jamalipour. "Absorption and fluorescence spectroscopy on a smartphone". In: B. Lee, S. B. Lee, Y. Rao, editors. Fifth Asia-Pacific Optical Sensors Conference. Proc. SPIE. 2015. 9655: 96551Z-1.

(23) R. Sumner. "Processing RAW Images in MATLAB". Department of Electrical Engineering, University of California Sata Cruz. May 19, 2014. Accessed online March 3, 2016. users.soe.ucsc.edu/~rcsumner/rawguide/RAWguide.pdf

(24) A.T. Ward. "Raman Spectroscopy of Sulfur, Sulfur-Selenium, and Sulfur-Arsenic Mixtures". J. Phys. Chem. 1968. 72(12): 4133-4139.

(25) N. Krishnamurthy. "Raman Spectrum of Crystalline Potassium Perchlorate". Proceedings of the Indian Academy of Sciences – Section A. 1965. 61(2): 118-121.

(26) E.M. A. Ali, H.G.M. Edwards, I.J. Scowen. "Raman spectroscopy and security applications: the detection of explosives and precursors on clothing". J. Raman Spectrosc. 2009. 40(12): 2009-2014.

(27) K.B. Mabrouk, T.H. Kauffmann, H. Aroui, M.D. Fontana. "Raman study of cation effect on sulfate vibration modes in solid state and in aqueous solutions". J. Raman Spectrosc. 2013. 44(11): 1603-1608.

(28) Eastman Kodak Company. Revisions 3.0 MTD/PS-0534. Application Note. August 13, 2008.

CHAPTER 5

ORDER-OVERLAP AND OUT-OF-BAND BACKGROUND REDUCTION IN THE SPATIAL HETERODYNE RAMAN SPECTROMETER WITH SPATIAL FILTERING

5.1 INTRODUCTION

The spatial heterodyne spectrometer (SHS) in a diffraction grating based interferometer originally developed for emission measurements of celestial bodies and flame-based emission measurements.[1-5] Recent development of the SHS resulted in adaptation for a variety of techniques including Raman spectroscopy, in the form of the spatial heterodyne Raman spectrometer (SHRS),[6-12] and laser-induced breakdown spectroscopy (LIBS).[13,14] The general SHS design is capable of having a large entrance aperture, and high spectral resolution as resolution is not strongly tied to entrance aperture size, as well as a large field of view, approximately 1°. The combination of the large entrance aperture and large field of view allows for high light throughput, up to 200 times that of a typical dispersive spectrometer.[1] The field of view of the SHS can be further expanded up to ~10° through the addition of field widening prisms.[15-17] Recent advancements of the SHS in Raman spectroscopy, which has very low signal intensity and high backgrounds due to a variety of sources (*e.g.,* fluorescence, ambient light), has brought to light problems with the SHS design that have a greater impact on Raman measurements than emission measurements due to the low signal intensities and

high backgrounds common in Raman spectroscopy.

The operation of the general SHS design has been elucidated in great detail elsewhere, however a brief explanation is necessary.[1-17] The SHRS, shown in Figure 5.1, consists of a beam splitter which splits incoming light into two arms with diffraction gratings in each arm. Light is diffracted by the gratings, inducing a wavelength-specific wavefront tilt, resulting in crossed wavefronts when the light recombines back through the beam splitter. The crossing of wavefronts from each arm of the interferometer results in a spatial phase shift along the dispersion plane of the diffraction gratings, allowing interference to occur, which generates an Fizeau fringe pattern. A high-quality imaging lens is used to image the plane of the face of the diffraction gratings onto an array detector. The Fourier transform of this fringe pattern recovers the spectrum. One wavelength of light will satisfy the Littrow condition based on the rotation angle of the diffraction grating, thus called the Littrow wavelength, and retro-reflect along the incident path, resulting in no wavefront tilt for that specific wavelength, and no interference pattern. The fringe patterns of all wavelengths other than the Littrow wavelength will be heterodyned about the Littrow wavelength, which allows the spectrum of the spectral window of the SHRS to be recovered with a relatively small number of detector elements in the array detector. None of the optical components must be moved or scanned during spectrum acquisition, however, the spectral window of the SHRS can be moved to a different spectral region by changing the rotation angle of the diffraction gratings.

Diffraction orders adjacent to the primary diffraction order being used to generate the interference pattern can overlap the primary diffraction order which increases

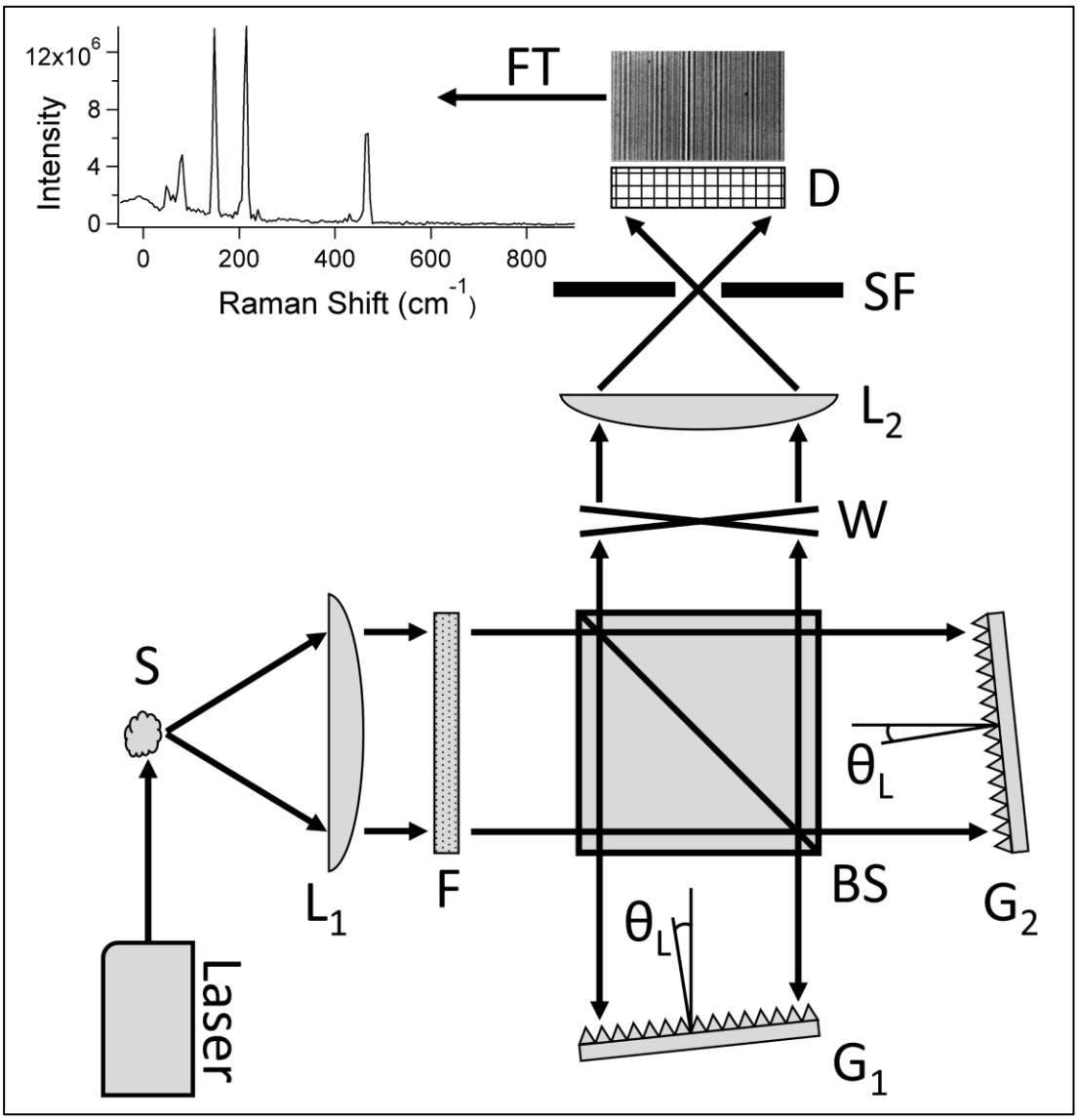

Figure 5.1: Schematic diagram of the SHRS. S is the sample of interest. L_1 is the collection lens which collimates sample light into the SHRS. F is a set of laser-rejection filters. BS is the cube beamsplitter. G_1 and G_2 are the diffraction gratings which are tilted to angle θ_L. W is the crossing wavefronts from each arm of the interferometer. L_2 is a high-quality imaging lens. SF is a spatial filter. D is an array detector.

background light within the interferogram and can result in the generation of additional interference patterns. This problem can degrade the interferogram, which negatively impacts spectral results. The problem of order-overlap becomes increasingly worse as lower groove-density diffraction gratings are employed, as the angular separation between diffraction orders becomes smaller, or as the diffractions gratings are moved closer to the beamsplitter in an attempt to miniaturize the system, which is of particular interest to our research group. The angular separation of adjacent diffraction orders can be determined using the generalized diffraction grating equation simplified for the SHS design:

$$md = 2\sigma_0 \sin\theta_L \qquad \text{Eqn. 5.1}$$

Where m is the diffraction order, d is the diffraction grating groove density, σ_0 is the wavenumber corresponding to the Littrow wavelength, and θ_L is the tilt of the diffraction gratings which satisfies the Littrow condition for σ_0. For example, if we set the Littrow wavelength to 532 nm and the diffraction grating density to 150 grooves/mm with the first diffraction order used to generate the interferogram, the angle formed between the first and second diffraction orders is only ~ 2.3°. This small angle is further complicated by the fact that we must consider the incoming light as a collimated beam and not a single ray traveling on the optical axis. The consequence is that light diffracted into the first order at one side of the input beam (*e.g.,* the far left side of the grating) can overlap with light diffracted into the second order at the opposite side of the input beam (*e.g.,* the far right side of the grating). The minimum separation distance between the diffraction grating and the imaging optic to avoid transmission of the second diffraction to the detector can be expressed with the equation:

$$D = \frac{W}{\tan\left[\sin^{-1}\left(\frac{d}{\sigma_0}\right) - \sin^{-1}\left(\frac{d}{2\sigma_0}\right)\right]} \qquad \text{Eqn. 5.2}$$

Where D is the grating-imaging-optic separation distance and W is the width of the imaging optic. Using the above de fined Littrow wavelength and diffraction grating groove density with 25.4 mm diameter for all optical components results in a diffraction grating to imaging optic separation of 635 mm. If we assume 1:1 imaging onto the detector this results in a footprint of the SHRS, not including the size of the detector of 635x1270 mm, quite large for a Raman spectrometer.

The large acceptance angle and large entrance aperture of the SHS results in a geometric bandpass, the range of wavelengths that can pass through the system and reach the detector, that can be much larger than the spectral bandpass, the range of wavelengths that can be resolved by the system in a particular configuration. The spectral range needed to recover most Raman bands of interest is ~ 3000 cm^{-1} which results in a spectral bandpass of ~ 100 nm with 532 nm excitation or ~ 20 nm with 244 nm excitation. The geometric bandpass of the SHRS can be several hundred nanometers, often limited by the transmission limitations of the optical materials used. This is a distinct contrast to the slit-based dispersive spectrometers more commonly used for Raman spectroscopy in which the geometric bandpass is equivalent to the spectral bandpass. Furthermore, because light is collimated before entering the SHRS, light of all wavelengths is distributed evenly onto the diffraction gratings and background light is distributed throughout the interferogram. Thus, even if background light is spectrally separated from the spectral bands of interest, the intensity and noise of the background light is distributed throughout the interferogram which negatively impacts the recovered spectrum. With a dispersive spectrometer, if the

background light is spectrally separated from the spectral bands of interest, the background light will not negatively affect the recovery of the bands of interest. Typically, SHRS experiments have employed optical filters (*e.g.,* long-pass, short-pass, and band-pass filters) to eliminate light outside of the spectral region of interest,[6-12] and pulsed lasers have been used with gated detection to reduce background light in ambient-light conditions.[8] However, as this paper will demonstrate, both the problem of order-overlap and the problem of out-of-band light can be overcome by placing a small spatial filter at the focal point of the imaging lens between the imaging lens and the detector, which eliminates diffraction order-overlap and significantly limits the geometric bandpass of the SHRS.

5.2 EXPERIMENTAL

The SHRS was constructed using a 25.4 mm 50:50 non-polarizing cube beamsplitter (CM1-BS013, Thorlabs) and two 25.4 mm 150 groove/mm diffraction gratings blazed for 500 nm (10RG150-500-1, Newport) which were placed ~ 22 mm from the nearest face of the beamsplitter. The output of the SHRS was imaged onto a Princeton Instruments PI-MAX 256x1024 ICCD using a Nikon 80-200 mm f/4.5-5.6 lens. Spatial filtering was achieved by placing a mechanical razor-edge slit (variable from 0 mm to 8 mm) between the imaging lens and the camera at the focal point of the lens. Raman excitation was achieved with a 0.2-2 W 532 nm CW laser (Millennia Pro, Spectra-Physics). Raman scattered sample light was collected and collimated into the SHRS with a 25.4 mm diameter f/2 plano-convex lens (LA1131, Thorlabs). Out-of-band light was introduced to the system for some experiments by passing a collimated beam of white light through a 650 nm long-pass filter (FEL0650, Thorlabs). The fast Fourier

transform was applied to the interferogram in Matlab to recover the spectrum. Powdered samples of > 99% purity sulfur and potassium perchlorate were pressed into compact pellets with a 10 ton pellet press. The experimental setup was modeled in the ray-tracing program Zemax with the only significant difference being that the imaging lens was approximated as a single plano-convex lens of the same diameter as the front optic in the Nikon imaging lens used and the same focal length as the Nikon imaging lens, to simplify the model.

5.3 RESULTS & DISCUSSION

The optical setup of the SHRS described above was replicated in the ray-tracing program Zemax with the only significant difference being that the imaging lens simulated as a simple plano-convex lens of the same focal length and front diameter diameter to reduce complexity. Figure 5.2a shows a diagram of the optical setup generated in Zemax with only the 1st diffraction order, the order used to generate the fringe pattern, traced and all other diffraction orders not traced. The large collimated beam of light incoming to the SHRS has been reduced to two small beams placed towards the extremes of the entrance aperture so that the reader can more easily see how the rays are split into the various diffraction orders and pass through the imaging lens. It can be seen that the light diffracted into the 1st diffraction order passes through the focal point of the imaging lens, where the spatial filter is placed. Figure 5.2b shows the same Zemax model but with only the 0th and 2nd diffraction orders traced and all other diffraction orders not traced. These two diffraction orders are adjacent to the 1st diffraction order and thus are the culprits for order overlap. It can be seen that, unlike the 1st diffraction order, the 0th and 2nd diffraction orders are diverted from the optical axis and do not pass through the focal

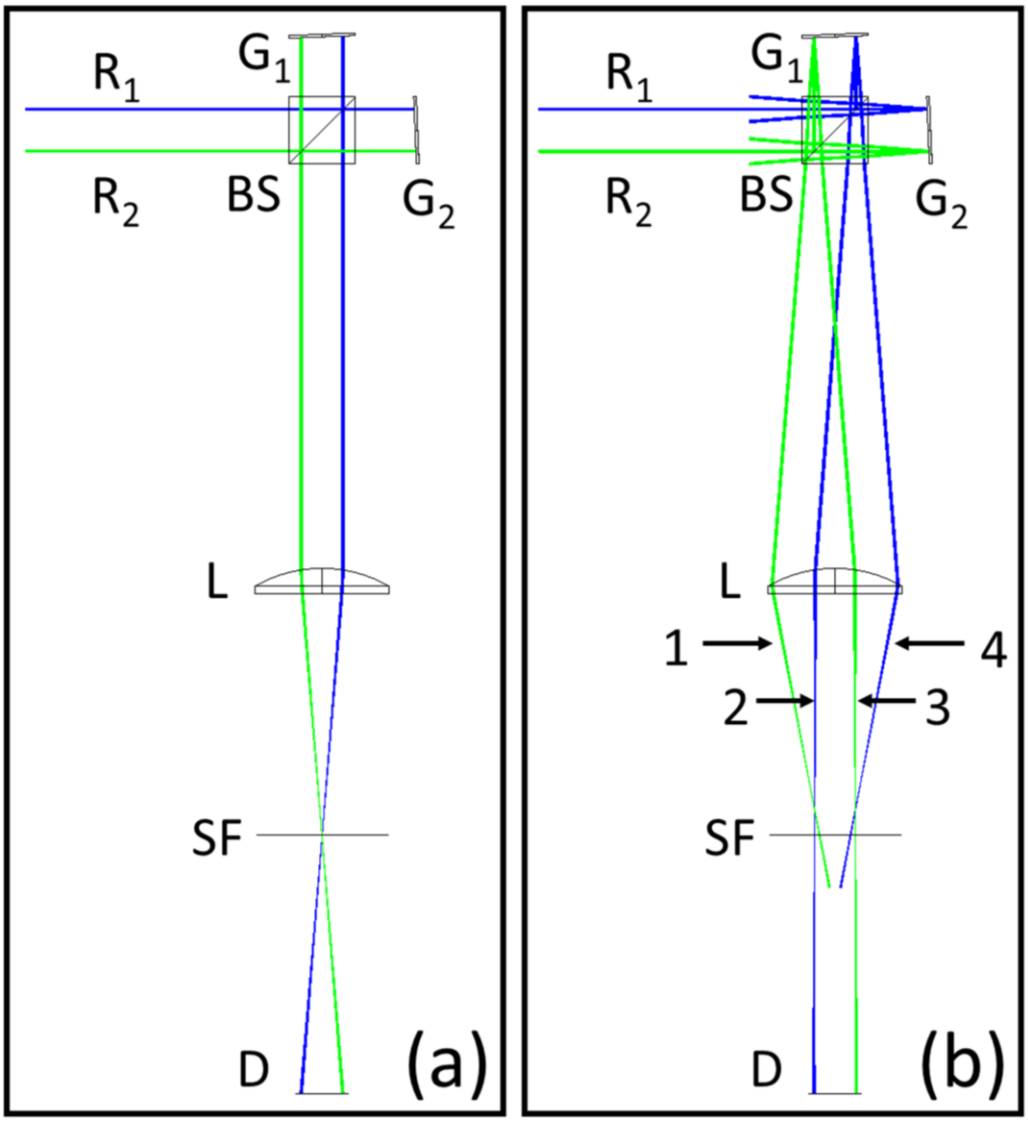

Figure 5.2: Zemax modeling of the spatial filter. (a) A model of the SHRS described in the experimental section generated in Zemax with only the 1st diffraction order of each grating shown. R_1 and R_2 are the input rays, placed towards the edge of the entrance aperture. G_1 and G_2 are the diffraction gratings. BS is the cube beamsplitter. L is the imaging lens, modeled as a single plano-convex lens for to reduce complexity. D is the array detector. (b) The same Zemax model shown in (a) but with only the 0^{th} and 2^{nd} diffraction order of each grating shown. 1 results from order 0 of G_1 and order 2 of G_2. 2 results from order 0 of G_1 and order 2 of G_2. 3 results from order 2 of G_1 and order 0 of G_2. 4 results from order 2 of G_1 and order 0 of G_2.

point of the imaging lens. These adjacent diffraction orders are instead spatially separated at the spatial filter such that a relatively large spatial filter aperture diameter will allow the 1st diffraction order will pass through and continue to the detector but the 0th and 2nd diffraction orders will not be able to pass the aperture. To demonstrate the problem of order-overlap experimentally, a collimated beam of 532 nm laser light was introduced into the entrance aperture of the real SHRS, the laser blocking filters were removed, a paper target was placed at the imaging plane of the imaging lens, and a camera was used to capture the image of the fringe pattern formed on the paper target, shown in Figure 5.3a. The image shows a bright, central, vertical fringe pattern, due to the 1st diffraction order, and dimmer, rotated fringe patterns to either side of the central fringe patter, due to the adjacent diffraction orders. Each adjacent fringe pattern is formed by the interference generated between the 0th diffraction order of one grating and the 2nd diffraction order of the other grating. The image also shows a faint, halo-like ring at the edges of the image, likely caused by light scattering randomly off the apertures of the cage containing the beamsplitter which have threads so that lens tubes can be attached to the beam splitter cage. The regions of overlap between the 1st order fringe pattern and the adjacent orders fringe patterns have a higher baseline than the un-overlapped region. The order-overlapped region can also generate additional, unwanted fringe patterns as the adjacent diffraction orders contain the same wavelengths of light as the 1st diffraction order but significantly different wavefront tilts, which results in different spatial phase-shifts. Figure 5.3b shows the same setup as described for Figure 5.3a but with a 3.5 mm diameter circular spatial filter aperture placed at the focal point of the imaging lens. As the image shows, the spatial filter completely removes the fringe patterns generated by

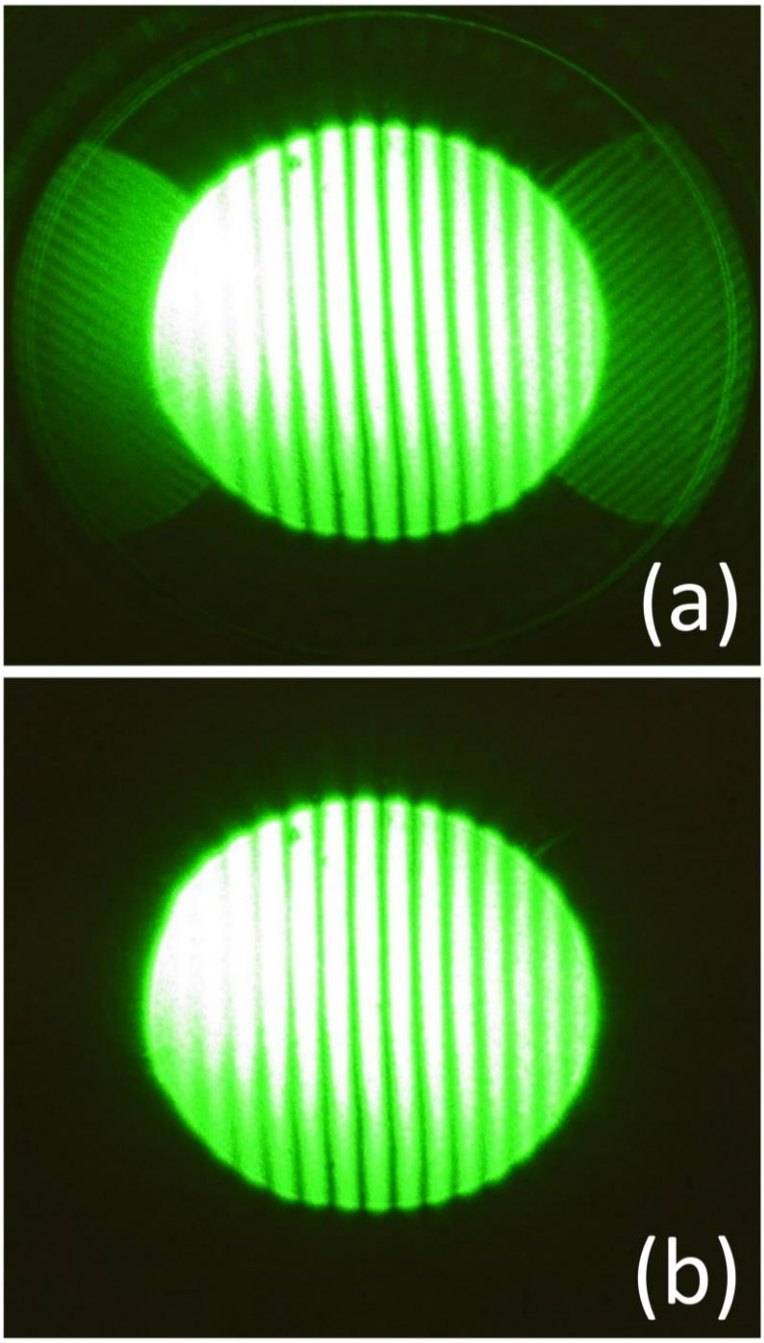

Figure 5.3: Demonstration of the effect of spatial filtering on the fringe pattern. (a) A picture of 532 nm laser fringes formed at the image plane of the high-quality imaging lens of the SHRS. Interference patterns generated by diffraction orders 0 and 2 can be seen to either side of the central fringe image. (b) A picture of the same conditions as (a) but with a 3.5 mm spatial filter placed at the focal point of the high-quality imaging lens.

the adjacent diffraction orders and the ring around the image.

The geometric bandpass of the SHRS, as described briefly above, can be several times larger than the spectrally resolvable bandpass. This means that there is a very large region of the light spectrum which can pass through the system and reach the detector but only a relatively small region of the light spectrum can contribute to the interference pattern in a manner which the detector can successfully resolve. Although it is possible for all wavelengths of light passing through the SHRS to form interference patterns, the Nyquist criterion dictates that at minimum 2 pixels of the detector are required to resolve a single fringe, which sets the limit for the range of wavelengths that can generate fringe patterns that can be resolved by the detector. The spatial fringe frequency formed by the SHRS is:

$$f(x) = 4(\sigma - \sigma_0)\tan\theta_L \qquad \text{Eqn. 5.3}$$

Where $f(x)$ is the spatial fringe frequency, σ is the wavenumber of the wavelength forming the fringe pattern, σ_0 is the wavenumber of the Littrow wavelength, and θ_L is the diffraction grating tilt for that Littrow wavelength.

If we combine Equations 5.1 and 5.3 with the pixel pitch of the PI-MAX ICCD used, 26 μm, a 532 nm Littrow wavelength, and the 150 gr/mm diffraction gratings we can determine that the maximum wavenumber shift from Littrow that can be resolved by this particular SHRS configuration is ~ 1200 cm^{-1}. Any wavelengths entering the system beyond this spectral region will not form interference patterns that can be resolved by the system. However, because diffraction at the gratings induces a wavelength-specific angular component to light leaving the gratings, wavelengths further from the Littrow wavelength will leave the gratings at a greater angle and enter the imaging lens at a

greater angle to the optical axis which results in a wavelength-dependent spatial separation at the focal point of the imaging lens. Thus a spatial filter aperture at the focal point of the imaging lens can allow wavelengths close to the Littrow wavelength to pass while blocking wavelengths further from Littrow. To demonstrate this, the Zemax model of the SHRS was used with two input light sources, one source corresponding to a monochromatic 219 cm^{-1} shift from the 532 nm Littrow to simulate a single band within the spectrally resolvable region and one source corresponding to a pseudo-broadband composed of 10 wavelengths in the 650-800 nm region (~ 3400-6300 cm^{-1} shift from Littrow) to simulate background light that is unresolvable by the system. Each source was composed of 100 million rays. Non-sequential ray-tracing was used to generate interferograms which were captured by the 250x1000 pixel detector sized to match the 26 μm pixel pitch of the PI-MAX ICCD used for experimental results. The spatial filter at the focal point of the imaging lens was varied from 0 mm to 8 mm width in 0.5 mm increments per ray-trace and each spatial filter width was ray-traced in triplicate. The resulting fringe patterns were Fourier transformed in Matlab to recover the spectrum and the signal-to-noise ratio (SNR) was calculated as the baseline-subtracted peak intensity divided by the standard deviation of a region of the spectrum in which no peaks were present. The results of this Zemax simulation are shown in Figure 5.4. As the plot shows, with small spatial filter apertures the SNR is very high but as the spatial filter aperture is widened further the SNR drops significantly. This trend corresponds to degradation of the interferogram by the pseudo-broadband light that is unresolvable by the SHRS which is prevented from reaching the detector at smaller spatial filter aperture widths.

The Zemax simulation described above was replicated experimentally with a

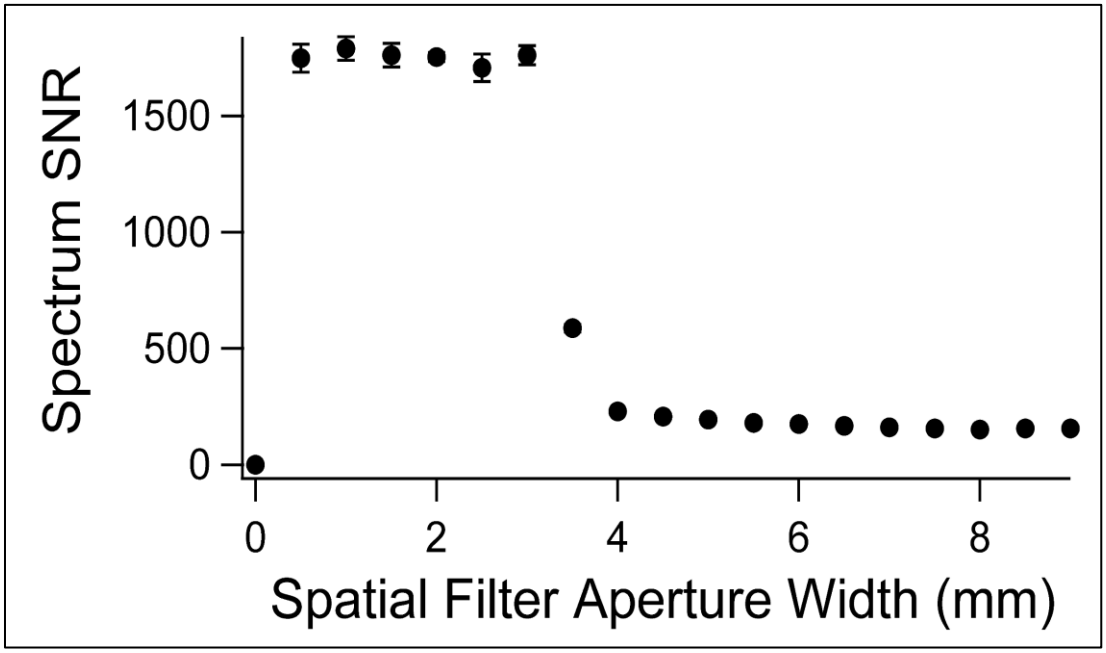

Figure 5.4: The result of a series of Zemax simulations of the SHRS described in the experimental section with a monochromatic light source corresponding to a 219 cm^{-1} shift from the Littrow wavelength and a pseudo-broadband light source composed of 10 wavelengths in the 650-800 nm region which are outside of the spectrally resolvable bandpass of this particular SHRS configuration. Ray traces were performed with 100 million rays each to the monochromatic source and the pseudo-broadband source at a particular spatial filter aperture width. The fringe image formed on the 250x1000 pixel array detector was Fourier transformed and the signal-to-noise ratio was calculated.

mechanically-variable slit, taken from a monochromator, placed at the focal point of the imaging lens to precisely control the width of the spatial filter aperture. A compact pellet of sulfur was illuminated with 200 mW of 532nm laser and the scattered light was collimated into the SHRS by the f/2 collection lens to provide spectrally resolvable fringe patterns. Light from a tungsten lamp was collimated to a 1" diameter beam, passed through a 650 nm long-pass filter, and shined onto the sulfur pellet so that the collection lens could transmit the light into the SHRS to provide broadband light outside of the spectrally resolvable region of this SHRS configuration. Images collected with the laser on and white light source off were compared to images collected with the laser off and white light source on to determine that the broadband light passing through the SHRS and reaching the detector was > 3x more intense than the Raman light impingent upon the detector. The spatial filter width was varied from 0 mm to 8 mm width in 0.5 mm increments with 1 second exposures captured at each spatial filter width. The series of spatial filter widths was collected in triplicate with the order of spatial filter widths within each series randomized. The SNR of each sulfur Raman spectrum was calculated, as described above, using the 219 cm^{-1} sulfur band with the results shown in Figure 5.5. As seen in Figure 5.4, a small spatial filter aperture provides a high SNR in Figure 5.5 but as the spatial filter aperture width is further widened the SNR decreases significantly. A notable difference between Figure 5.4 and Figure 5.5 is the shape of the SNR as a function of spatial filter aperture width. In Figure 5.4 we see an almost square profile whereas in Figure 5.5 we see curved profile. This difference in curves between the two plots is due to the fact that the imaging lens in the Zemax model achieves a diffraction-limited spot-size on the order of 10's of μm and so the smallest, non-zero spatial filter

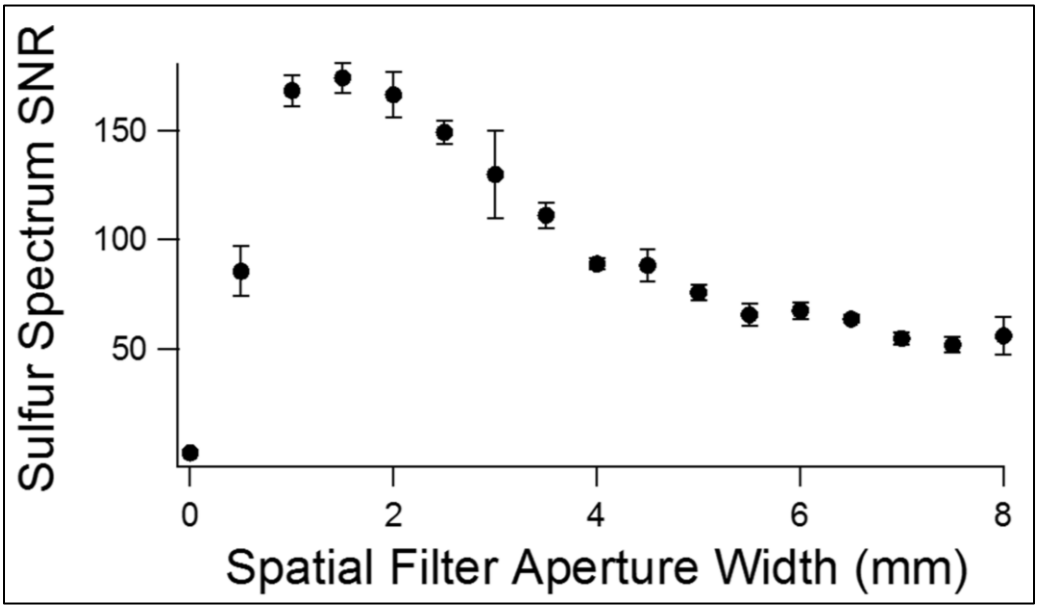

Figure 5.5: The signal-to-noise ratio for sulfur Raman measurements made with different spatial filter aperture widths with white light passed through a 650 nm long-pass filter to introduce light that is outside of the spectrally resolvable bandpass of this particular SHRS configuration. The > 650 nm light was > 3x higher intensity at the detector than the Raman light.

aperture width used passes all of the 219 cm^{-1} band light. Conversely, light at the focal point of the real imaging lens does not achieve a diffraction-limited spot-size and the smallest, non-zero spatial filter aperture width used is slightly smaller than the focused light so full transmission of the Raman scattered light does not occur until a larger spatial filter aperture. Similarly, the broadband light in the real experiment does not achieve a diffraction-limited spot-size at the spatial filter and thus is able to begin passing the spatial filter at a lower spatial filter aperture width, thus decreasing SNR at a lower width than the Zemax model. Figure 5.6a shows the Raman spectrum of sulfur, recovered at the widest spatial filter aperture width and Figure 5.6b shows the Raman spectrum of sulfur recovered at the spatial filter aperture width corresponding to the highest SNR as indicated by Figure 5.5, 1.5 mm. The spectra in Figure 5.6a and Figure 5.6b show the same group of sulfur Raman bands we would expect to obtain, and the band intensity is relatively the same between the two spectra but the noise at the widest spatial filter aperture is significantly higher, resulting in a decrease in SNR by ~ 3x.[18] This increase in noise is due to the increased background in the interferogram caused by more light that cannot be resolved by the SHRS being present in the interferogram.

The sulfur Raman experiment described above was repeated with a potassium perchlorate pellet with 500 mW 532 nm excitation, and all other experimental parameters the same. While the sulfur pellet was fairly opaque to the laser light, the potassium perchlorate pellet was much more transmissive to the laser, evidenced by the fact that the entire pellet appeared to light up upon illumination by the laser and observation of the side of the pellet orthogonal to the laser path revealed that scattered light could be observed several millimeters into the pellet. The difference in penetration depth of the

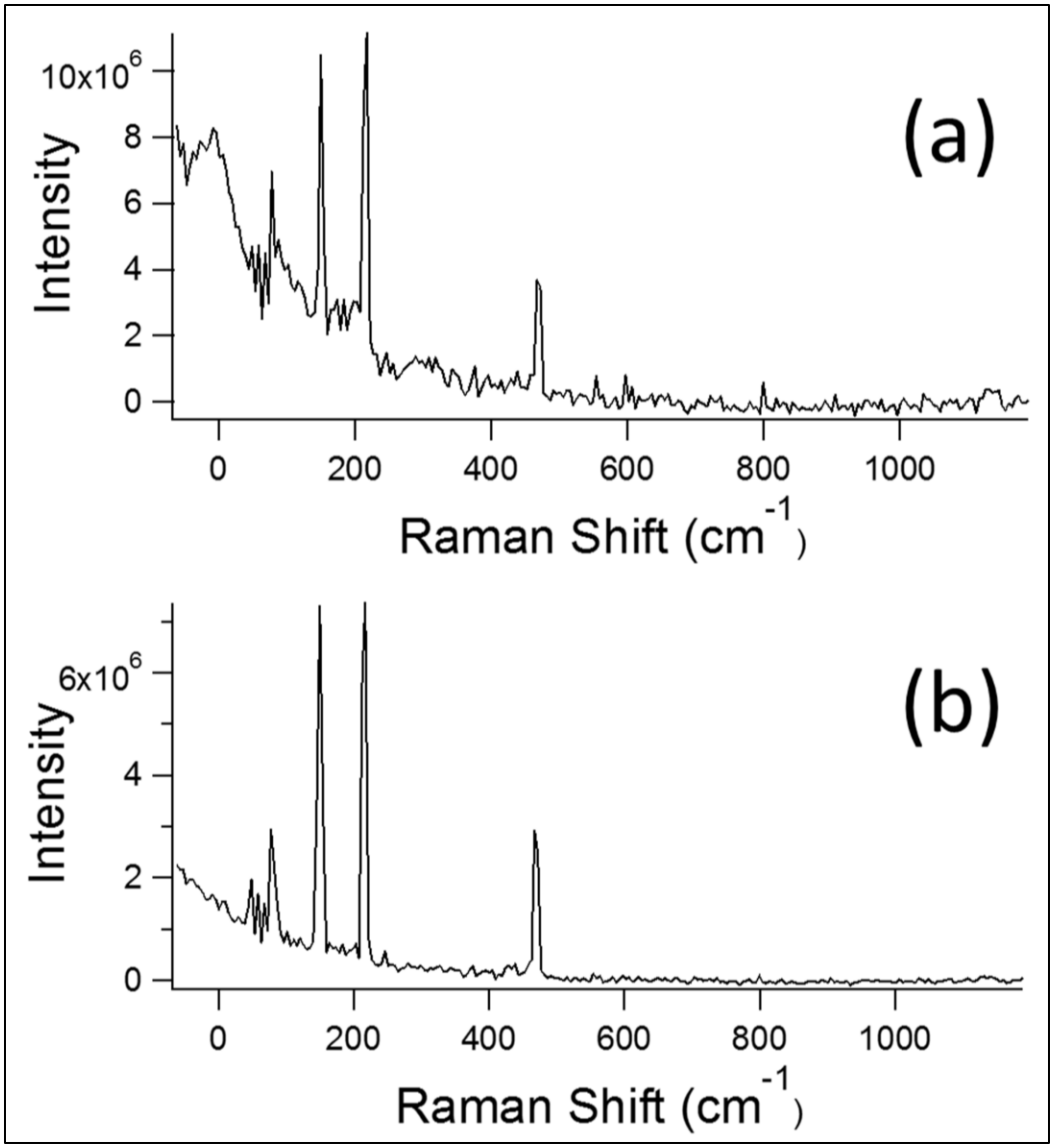

Figure 5.6: Comparison of spectral results with spatial filtering. (a) A sulfur Raman spectrum collected with the widest spatial filter aperture. (b) A sulfur Raman spectrum collected with a 1.5 mm wide spatial filter aperture, which provided the highest SNR.

laser between the two pellets affects the ability of the collection lens to collimate the scattered into the SHRS, resulting in both collimated and slightly-uncollimated sample light entering the system. The effect of this can be seen in Figure 5.7 in which the maximum SNR for perchlorate Raman, calculated with the ~ 900 cm^{-1} band, occurs at a slightly wider spatial filter aperture width, 2.5 mm. The maximum SNR of perchlorate occurs at a spatial filter aperture width 2/3 larger than the spatial filter aperture width for maximum SNR of sulfur. The higher penetration depth in perchlorate results in some of the incoming light being slightly uncollimated which results in a larger focused point at the focal point of the imaging lens. Figure 5.8a shows the potassium perchlorate spectrum recovered at the widest spatial filter aperture width and Figure 5.8b shows the perchlorate spectrum recovered at the spatial filter aperture width corresponding to the highest SNR as indicated by Figure 5.7. Both spectra show the same Raman bands that we would expect to see and the peak intensity is essentially the same, however the noise of Figure 5.8a is significantly higher due to the out-of-band light present in the interferogram, resulting in a decrease of SNR by ~ 3x.[19]

5.4 CONCLUSIONS

Diffraction orders adjacent to the primary diffraction order of interest in the SHRS are capable of being transmitted through the imaging lens and onto to the detector, generating unwanted interference patterns which are capable of degrading the primary interference pattern. A strategically placed aperture between the imaging lens and detector at the focal point of the imaging lens has been shown to be capable of blocking unwanted light from adjacent diffraction. Out-of-band light which is unresolvable by the SHRS is capable of decreasing fringe contrast in the interference patterns generated by

spectrally resolvable light, which in turn reduces the signal-to-noise of the recovered spectrum. The implementation of a spatial filter between the imaging lens and detector of the SHRS has been shown capable of reducing the intensity of light which is outside the spectrally resolvable region at the detector, thus improving the signal-to-noise ratio of the recovered spectrum.

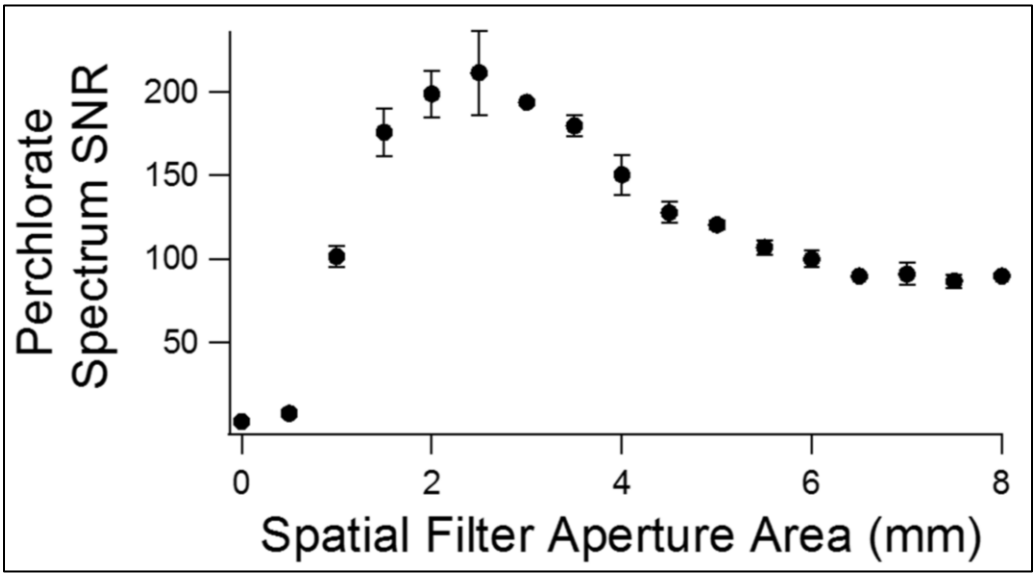

Figure 5.7: The signal-to-noise ratio for potassium perchlorate Raman measurements made with different spatial filter aperture widths with white light passed through a 650 nm long-pass filter to introduce light that is outside of the spectrally resolvable bandpass of this particular SHRS configuration. The > 650 nm light was > 3x higher intensity at the detector than the Raman light.

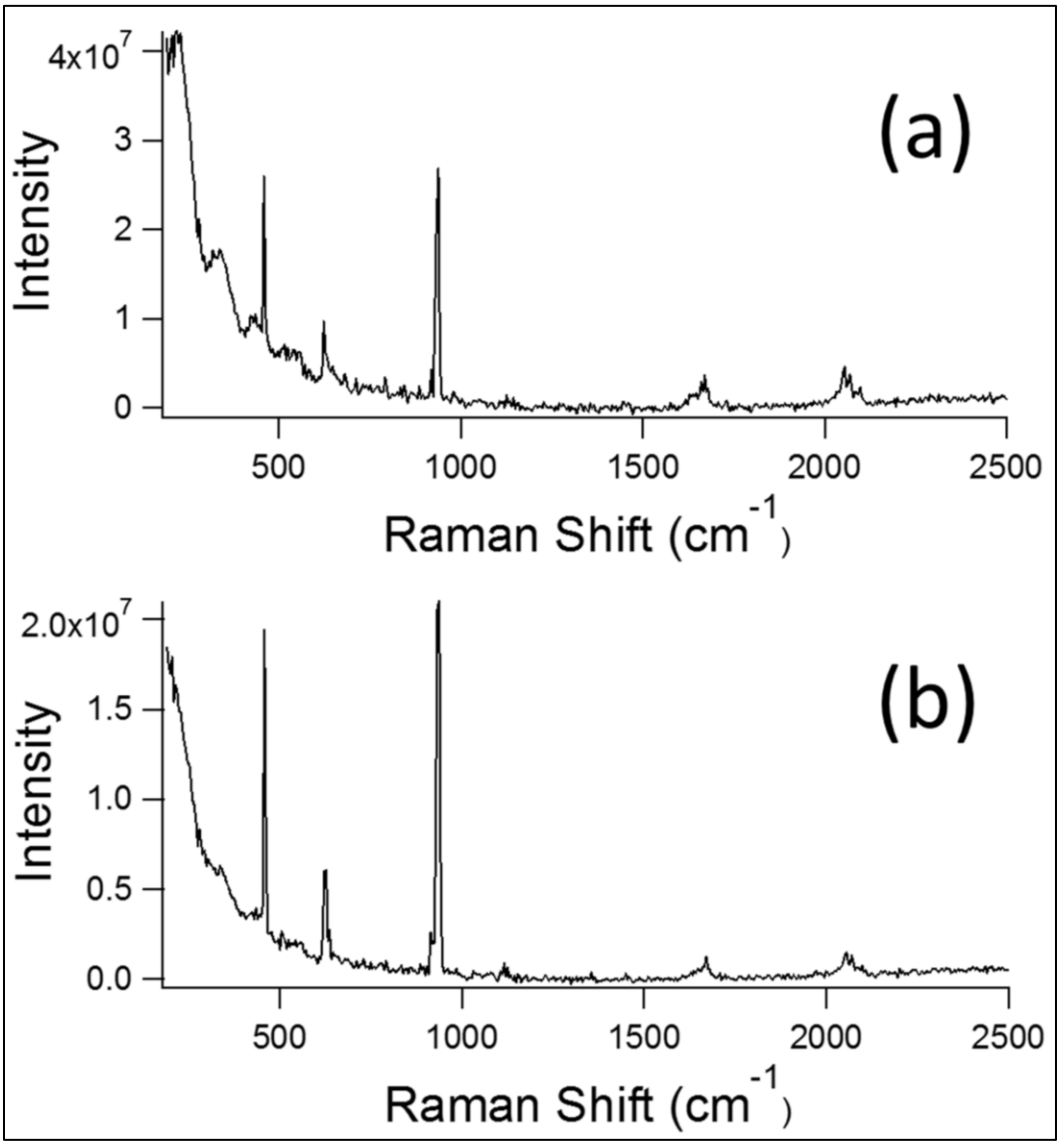

Figure 5.8: Comparison of spectral results with spatial filtering. (a) A potassium perchlorate Raman spectrum collected with the widest spatial filter aperture. (b) A potassium perchlorate Raman spectrum collected with a 2.5 mm wide spatial filter aperture, which provided the highest SNR.

REFERENCES

(1) J.M. Harlander, Spatial Heterodyne Spectroscopy: Interferometric Performance at Any Wavelength without Scanning. [Ph.D. Dissertation]. Madison, WI: University of Wisconsin-Madison, 1991.

(2) J.M. Harlander, F.L. Roesler. "Spatial heterodyne spectroscopy: a novel interferometric technique for ground-based and space astronomy". Proc. SPIE. 1990. 1235: 622-633.

(3) J.M. Harlander, R.J. Reynolds, F.L. Roesler. "Spatial Heterodyne Spectroscopy for the Exploration of Diffuse Interstellar Emission Lines at Far-UV Wavelengths". Astrophys. J. 1992. 396: 730-740.

(4) J.M. Harlander, H.T. Tran, F.L. Roesler, K. Jaehnig, S.M. Seo, W. Sanders, R.J. Reynolds. "Field-Widened Spatial Heterodyne Spectroscopy: Correcting for Optical Defects and New Vacuum Ultraviolet Performance Tests". Proc. SPIE. 1994. 2280: 310-319.

(5) R.J. Bartula, J.B. Ghandhi, S.T. Sanders, E.J. Mierkiewicz, F.L. Roesler, J.M. Harlander. "OH absorption spectroscopy in a flame using spatial heterodyne spectroscopy". Appl. Opt. 2007. 46(36): 8635-8640.

(6) N.R. Gomer, C.M. Gordon, P. Lucey, S.K. Sharma, J.C. Carter, S.M. Angel. "Raman Spectroscopy Using a Spatial Heterodyne Spectrometer: Proof of Concept". Appl. Spectrosc. 2011. 65(8): 849-857.

(7) N. Lamsal, S.M. Angel. "Deep-Ultraviolet Raman Measurements Using a Spatial Heterodyne Raman Spectrometere (SHRS)". Appl. Spectrosc. 2015. 69(5): 525-534.

(8) N. Lamsal, S.M. Angel, S.K. Sharma, T.E. Acosta. "Visible and UV Standoff Raman Measurements in Ambient Light Conditions Using a Gated Spatial Heterodyne Raman Spectrometer". 46th Lunar and Planetary Science Conference. The Woodlands, Texas, March 16-20, 2015.

(9) K.A. Strange, K.C. Paul, S.M. Angel. "Transmission Raman Measurements using a Spatial Heterodyne Raman Spectrometer (SHRS)". Appl. Spectrosc. Published online before print June 30, 2016. doi: 10.1177/0003702816654156.

(10) P.D. Barnett, S.M. Angel. "Miniature Spatial Heterodyne Raman Spectrometer with a Cell Phone Camera Detector". Appl. Spectrosc. Published online before print August 29, 2016. doi: 10.1177/0003702816665127

(11) G. Hu, W. Xiong, H. Shi, Z. Li, J. Shen, X. Fang. “Raman spectroscopic detection using a two-dimensional spatial heterodyne spectrometer”. Opt. Eng. 2015. 54(11): 114101.

(12) G. Hu, W. Xiong, H. Shi, Z. Li, J. Shen, X. Fang. “Raman spectroscopic detection for liquid and solid targets using a spatial heterodyne spectrometer”. J. Raman Spectrosc. 2016. 47: 289-298.

(13) I.B. Gornushkin, B.W. Smith, U. Panne, N. Omenetto, “Laser-Induced Breakdown Spectroscopy Combined with Spatial Heterodyne Spectroscopy”. Appl. Spectrosc. 2014. 68(9): 1076-1084.

(14) P.D. Barnett, N. Lamsal, S.M. Angel. “Standoff LIBS using a Miniature Wide Field of View Spatial Heterodyne Spectrometer with Sub-Microsteradian Collection Optics”. Appl. Spectrosc. Paper in press 2016.

(15) J.M. Harlander, R.J. Reynolds, F.L. Roesler, G. Li. “Spatial Heterodyne Spectroscopy: Laboratory Tests of Field Widened, Multiple Order, and Vacuum Ultraviolet Systems”. Proc. SPIE. 1992. 1743: 48-59.

(16) J.M. Harlander, F.L. Roesler, R.J. Reynolds, K. Jaehnig, W. Sanders. “A Differential, Field-Widened Spatial Heterodyne Spectrometer for Investigations at High Spectral Resolution of the Diffuse Far Ultraviolet 1548 Å Emission Line from the Interstellar Medium”. Proc. SPIE. 1993. 2006: 141-148.

(17) J.M. Harlander, F.L. Roesler, K. Jaehnig, S.M. Seo, W. Sanders, R.J. Reynolds. “Field-Widened Spatial Heterodyne Spectroscopy: Correcting Optical Defects and New Vacuum Ultraviolet Performance Tests”. Proc. SPIE. 1994. 2280: 310-319.

(18) A.T. Ward. “Raman Spectroscopy of Sulfur, Sulfur-Selenium, and Sulfur-Arsenic Mixtures”. J. Phys. Chem. 1968. 72(12): 4133-4139.

(19) N. Krishnamurthy. “Raman Spectrum of Crystalline Potassium Perchlorate”. Proceedings of the Indian Academy of Sciences – Section A. 1965. 61(2): 118-121.

CHAPTER 6

STANDOFF LIBS USING A MINIATURE WIDE FIELD OF VIEW SPATIAL HETERODYNE SPECTROMETER WITH SUB-MICROSTERADIAN COLLECTION OPTICS

6.1 INTRODUCTION

Laser-induced breakdown spectroscopy (LIBS) was first reported by Brech and Cross in 1962[1] and is a relatively simple spectroscopic technique that allows rapid multi-elemental analysis of solids, liquids and gases with little or no sample preparation. LIBS is well suited for *in situ*, non-contact and remote elemental analysis because, in principle, only optical access to the sample is required for analysis.[2-20] This has lead to the development of remote (or standoff) LIBS where measurements are made on samples many tens of meters distant from the spectrometer. Remote LIBS has been used for applications as diverse as explosives detection,[20,21,22] underwater exploration and mining, and planetary exploration.[23,24] as well as assessment of damage to historical monuments,[25] Remote LIBS has been shown to be useful at distances up to many tens of meters and has also been combined with remote Raman.[26,27]

Measuring samples remotely using LIBS introduces two problems, both related to signal level. The collection solid angle for remote measurements is inherently low, thus reducing the LIBS signal level. To overcome this issue telescopes are usually used for light collection. However, the amount of light collected is limited by the throughput of the spectrometer, which is typically very low because of the need for small slits and large

f/# systems to achieve the spectral resolution needed for LIBS. Another problem unique to remote LIBS is movement of the laser on the sample. The field of view of a typical telescope coupled LIBS system is small, limited by the slit width of the spectrometer. For samples at 10's of meters distance it can be difficult maintaining the laser focus within the field of view of the spectrometer. The latter is particularly a problem for remote LIBS where the laser spot on the sample must be as small as possible for efficient plasma formation, and laser pointing stability issues can make spectrometer alignment issues more severe.

The spatial heterodyne spectrometer (SHS) is an interferometer that has some characteristics that are well suited for remote LIBS. Like other interferometers, the SHS has a very high light throughput and a wide field of view but also has very high spectral resolution. In addition, the SHS design has no moving parts making it compatible with a gated detector, necessary for remote LIBS. The SHS, first described by Harlandar,[28,29] is similar to a Michelson interferometer but the interference pattern is formed on an imaging detector using stationary, tilted diffraction gratings, thus there are no moving parts. The grating tilt angle determines the Littrow wavelength, which is the wavelength about which all others are heterodyned. Heterodyning allows high spectral resolution to be achieved with a relatively small number of samples, fixed by the number of horizontal pixels on the imaging detector. The large entrance aperture and wide acceptance angle of the SHS provides high light throughput, at least two orders of magnitude higher than a conventional dispersive spectrometer. In the case of standoff LIBS, this also makes the SHS relatively easy to couple with telescopic optics and minimizes laser pointing stability issues, because small movements of the laser spot on the target do not reduce the

amount of light collected by the spectrometer slit, unlike the case of a dispersive spectrometer where the output of the telescope has to be held in focus on a narrow input slit. In addition, all wavelengths are measured simultaneously in the SHS, making it compatible with pulsed lasers and gated detection, necessary in LIBS. The first description of a laser based gated SHS spectrometer was for visible Raman spectroscopy[30], and later for UV Raman[31,32] and remote Raman[32,33]. The SHS was also recently described for LIBS[34] but it has not been described for remote LIBS.

6.2 EXPERIMENTAL

The LIBS plasma was generated using a Continuum Surelite III 10Hz (Continuum, San Jose, CA, USA) pulsed laser doubled to 532 nm at ~ 50 mJ/pulse for benchtop measurements and ~ 130 mJ/pulse for standoff measurements. The laser was focused onto the sample using a high power, 5x beam expander. Fine tuning of the focus was done by monitoring the shock wave intensity of the LIBS spark using an amplified electret microphone element (Radio Shack, Model 270-092) and Tektronix TDS 1002 oscilloscope (Tektronix, Beaverton, OR, USA) . The SHS was constructed according to Figure 6.1 using 25x25 mm 300 groove/mm 500 nm blazed diffraction gratings masked with black anodized aluminum foil to expose only 10x10 mm to reduce the effective area of the gratings. As mentioned above, the lack of dependence of resolution on entrance width allowed the SHS to be constructed with a ~ 15 mm diameter circular entrance aperture to prevent the 10 mm wide exposed section of the diffraction gratings from being obscured. A Nikon AF-S Nikkor 70-200 mm f/2.8G ED VR II lens (Nikon, Tokyo, Japan) was used to image the plane of the diffraction gratings onto a Princeton Instruments PI-MAX 25 mm wide, 1024x256 ICCD (Princeton Instruments, Trenton, NJ,

USA). The gain of the ICCD was set to 100 for benchtop measurements and 250 for all standoff measurements. The imaging lens was set up to provid a ~ 2.2 times magnification so that the image of the 10 mm diffraction grating on the detector was ~ 22 mm, almost filling the detector in the horizontal direction and greatly overfilling it in the vertical direction. The SHS was built on a non-floating optical table with only a piece of common, soft foam between the SHS optical breadboard and the table for vibration isolation. Samples included copper plates obtained from an industrial supply company and are of unknown purity, magnesium rods (99.9+%, item number: 299405, Sigma-Aldrich, St. Louis, MO, USA), calcium metal (99%, item number: 327387, Sigma-Aldrich, St. Louis, MO, USA), and manganese chips (99%, item number: 266167, Sigma-Aldrich, St. Louis, MO, USA). ICCD gating parameters were optimized to produce the greatest interferogram depth of modulation for each sample. ICCD gate delay and width were 1.25 and 10.25 μs, respectively, for copper and magnesium, 2.3 and 2 μs for calcium, and 0.6 and 8 μs for manganese.

6.3 RESULTS & DISCUSSION

The SHLS, depicted in Figure 6.1, is similar in construction to a Michelson interferometer with the mirrors replaced by stationary reflective diffraction gratings**.** The diffraction gratings are tilted such that one particular wavelength, the Littrow wavelength, is retro-reflected along the incident light path and recombines at the beamsplitter**.** Heterodyning in the interferometer occurs at the Littrow wavelength, λ_L, corresponding to the wavelength of light that is exactly retro-reflected back along the same path, and hence recombines at the beamsplitter without interference. For any wavelength (λ) other than Littrow, the diffracted light leaves the gratings at an angle to

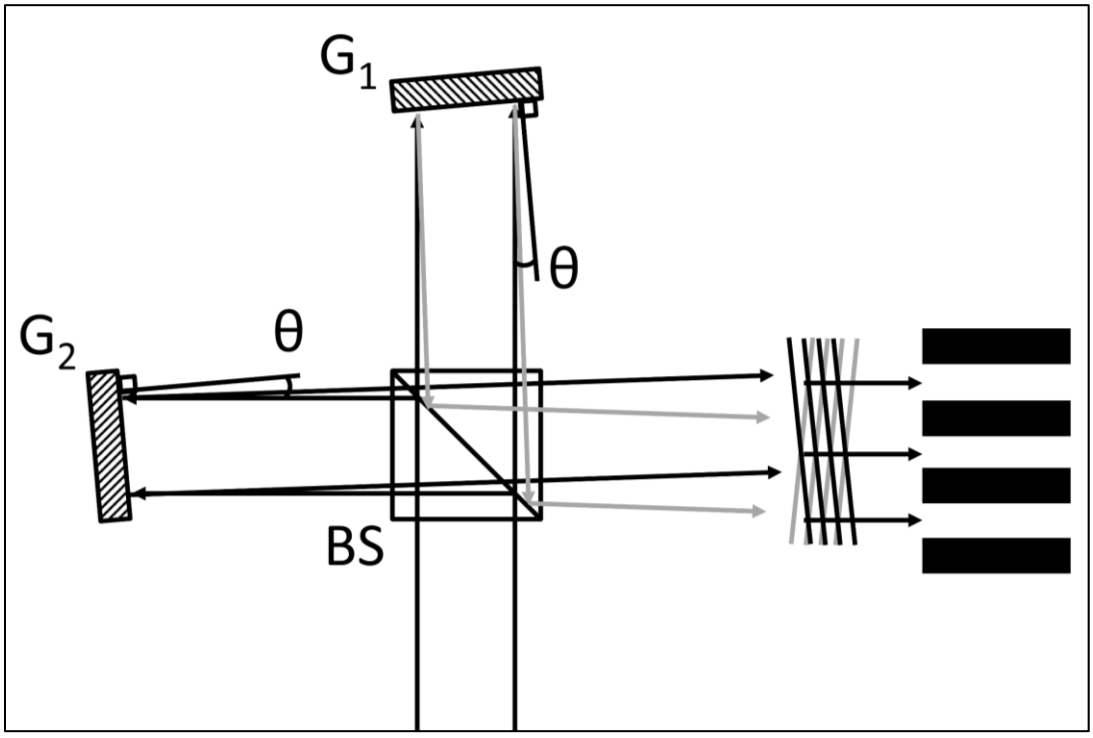

Figure 6.1: Block diagram of the SHLS. G_1 and G_2 are diffraction gratings placed equidistant from the beam splitter (BS) and tilted such that one wavelength, the Littrow wavelength, is retroreflected back along the optical axis. The faces of the diffraction gratings are imaged onto an array detector by a high quality imaging lens (not shown).

the optical axis, resulting in crossed wavefronts, inducing a spatial phase shift, and generating an interference pattern, which produces a series of wavelength dependent fringes on the array detector. The fringe frequency on the detector is given by Equation 1, where *f* is in fringes/cm and σ is the wavelength expressed in wavenumbers.[9, 35] A Fourier transform of the interferogram recovers the spectrum. According to Equation 6.1, emission lines above or below the Littrow wavelength may show identical fringe patterns and can lead to degenerate lines (i.e., line overlap).

$$f = 4(\sigma - \sigma_0)\tan\theta_L \qquad \text{Eqn. 6.1}$$

The SHS, like other Fourier transform interferometers, does not require a narrow slit to achieve high resolution as is common with dispersive spectrometers because there is no dependence of resolution upon entrance aperture width. This allows the SHS to employ very large entrance apertures, greatly increasing the throughput of the system, which is advantageous when signal strength is low such as when the source is very far from the detector in a standoff configuration.

The resolving power is equal to the number of grooves illuminated so in this case R = 6,000, giving a theoretical resolution of ~ 0.1 nm at 500 nm. For these studies about 900 ICCD pixels were illuminated horizontally, thus about 450 wavelength elements can be measured. Thus the theoretical ICCD-limited spectral range would be ~ 45 nm, on either side of the Littrow wavelength. This range is doubled if wavelengths above and below Littrow are considered. The maximum, resolution-limited solid angle field of view (FOV) of the SHRS is related to the resolving power by Equation 6.2.[20] Thus the solid angle FOV for this spectrometer is $1.0\text{x}10^{-3}$ sr, and the full acceptance angle is ~ 1.8°.

$$\Omega = \frac{2\pi}{R} \qquad \text{Eqn. 6.2}$$

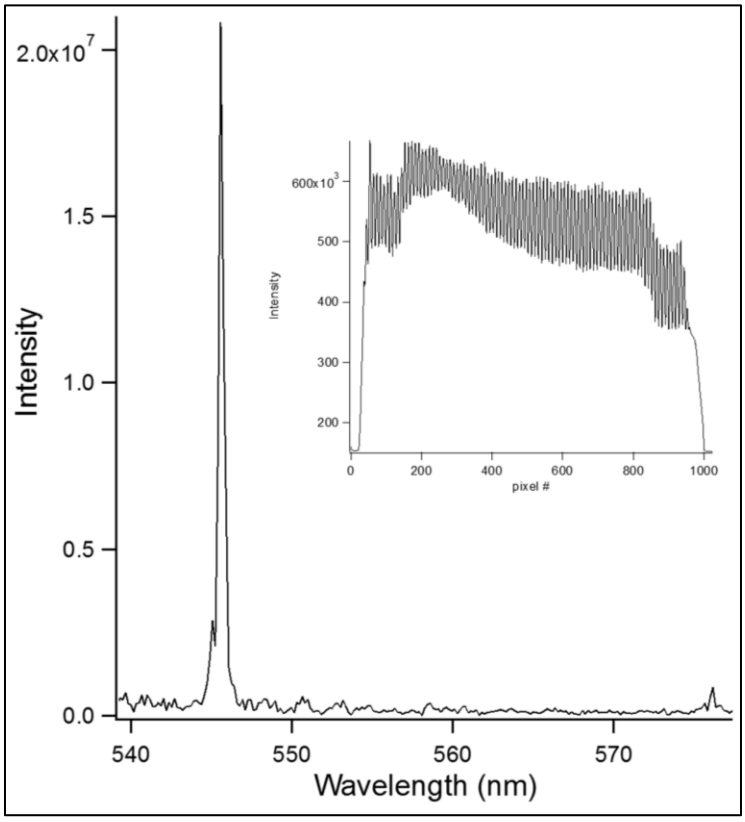

Figure 6.2: The emission spectrum of a low-pressure Hg discharge lamp measured with the SHLS, with the Littrow wavelength set to 532 nm.

Figure 6.2 shows the emission spectrum of a low-pressure mercury lamp measured with the SHLS with the Littrow wavelength set to ~ 532 nm, using a 1-mm diameter optical fiber whose end was placed 1.5 m from the entrance aperture of the SHLS, without any collimating optics. The measured full width half maximum (FWHM) line width of the 546.0 nm mercury emission line was 0.3 nm, about 3 times worse than the theoretical value for the SHLS. This indicates the SHLS alignment could probably have been improved. This is consistent with the fringe image cross section (inset in Figure 6.2) which shows a fringe visibility (FV, Equation 6.3) of about 0.2. The theoretical FV for a monochromatic source is 1.0. The asymmetry in the fringe cross section is also consistent with the interferometer arms not being identically aligned.

$$FV = \frac{(I_{max} - I_{min})}{(I_{max} + I_{min})} \qquad \text{Eqn. 6.3}$$

Additionally, as mentioned in the experimental section, the SHLS system was not used on a floating optical table, instead foam rubber was used for vibration isolation. Interferometric systems are extremely sensitive to low frequency vibrations commonly found in most buildings. Because the SHLS relies on wavefront tilt-induced phase shifts on the order of the wavelength of light being analyzed, low frequency vibrations are detrimental to the quality of the interferogram produced. This low-tech, foam-rubber vibration isolation system reduced vibrations in the fringe image to the point of being visually imperceptible, but may have contributed to the slightly lower resolution and fringe visibility.

The theoretical spectral bandpass of the SHLS is a function of the resolving power and the number of detector elements on the ICCD in the horizontal, spectral,

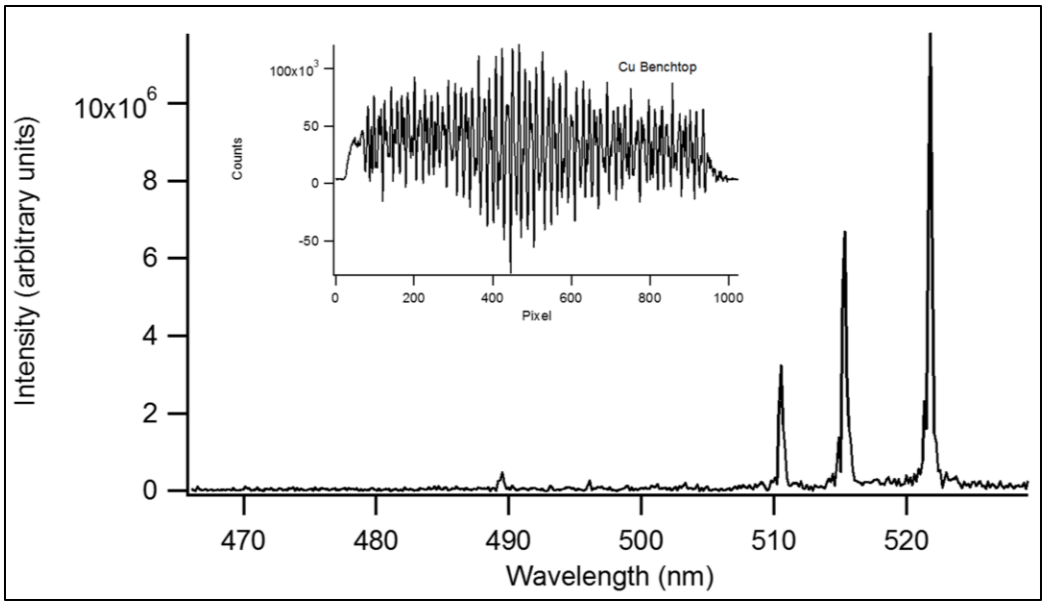

Figure 6.3: Benchtop spectrum of copper metal by an accumulation of 500 LIBS sparks. Inset shows the interferogram cross-section. The gate delay was 1.25μs with a 10.25 μs gate width.

direction. The spectral range of the SHLS is limited by the Nyquist limit as shown in Equation 6.4:

$$\Delta\lambda = \frac{N\lambda}{2R} \qquad \text{Eqn. 6.4}$$

Where $\Delta\lambda$ is the bandwidth, λ is the central wavelength, N is the number of detector elements in the dispersion plane of the diffraction gratings, and R is the resolving power.[28] For the system described the theoretical spectral range was 45 nm both above and below the Littrow wavelength.

Benchtop LIBS measurements of copper, magnesium, calcium, and manganese were taken by placing solid samples on the optical axis, 1.5 m from the SHLS entrance aperture. No collection optics were used to couple the LIBS emission into the system; light was collected only by the 10 mm diffraction gratings. At 1.5 m, this corresponds to a collection solid angle of ~ 4.6×10^{-5} sr at the gratings. Laser pulses were ~ 50 mJ/pulse with a 0.4 mm diameter spot size at the target and each sample spectrum was acquired using 500 laser shots. Figure 6.3 and 6.4 shows LIBS emission spectra of Cu and Mg metal samples, respectively. Both spectra are measured at wavelengths below the 532 nm Littrow but close to the laser wavelength. These elements show relatively strong emission lines in this spectral range with good signal to noise ratio. The FWHM of the strongest emission lines for both elements is about 0.3 nm. The insets show the interference fringe patterns, background subtracted. The FV is 0.20 for Cu and 0.26 for Mg. This low value is likely due to optical imperfections in the interferometer.

The three strong Cu lines at ~ 510, 515 and 522 nm match Cu emission lines listed in the NIST spectral data base.[36] The Cu spectrum was calibrated in wavelength using a least squares fit to the spectrum and the known wavelengths of the three strong

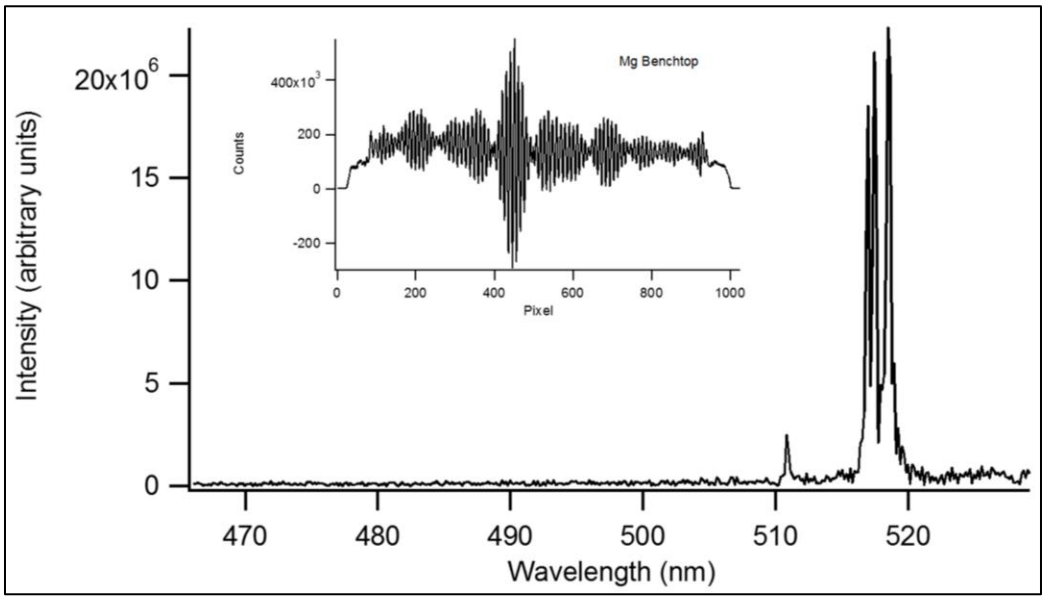

Figure 6.4: Benchtop spectrum of magnesium metal by an accumulation of 500 LIBS sparks. Inset shows the interferogram cross-section. The gate delay was 1.25μs with a 10.25 μs gate width.

Cu I lines. This calibration curve was useful in identifying lines in other spectra as well as locating lines at wavelengths above the Littrow wavelength that overlapped the spectral region shown. Two very weak lines, at ~ 490 and 496 nm match Cu I emission lines that appear above the Littrow wavelength at 573.2 and 570.0 nm, respectively. The three strongest Mg lines at 516.7, 517.3 and 518.4 match known Mg I emission lines that are listed in the NIST spectral data base.[17] The very weak line at ~ 510 nm matches a Mg I emission line that appears above the Littrow wavelength at 552.8 nm. In previous work we described how the degeneracy of lines above and below the Littrow wavelength can be removed, and the spectral range doubled, by tilting one diffraction grating vertically and using a 2D FFT. For the spectra shown here this is not necessary because the lines are sufficiently resolved and the calibration is good enough to determine which lines are above or below the Littrow wavelength, without ambiguity.

Figure 6.5 and 6.6 shows emission spectra of Ca and Mn metal samples, respectively, measured at 1.5 m with no collection optics other than the 10 mm gratings. Note that the Ca emission spectrum is shown below the Littrow wavelength, where the Ca I lines at ~ 504, 519, 526, and 527 nm are prominent. The spectrum is complicated though by Ca I lines at wavelengths above Littrow, overlapping lines in the region shown, especially around 504 nm where there are 7 Ca I lines from ~ 558 to ~ 560 nm that would overlap the 504 nm spectral range. The Mn spectrum shows lines in a spectral range above the Littrow wavelength. The main group of lines between ~ 538 and ~ 552 nm are Mn I lines. However, the line that appears at 547 nm does not match any line in this spectral region. It does match a known weak 515 nm Mn I line which would be folded into this spectral region. However, the 571 nm bandpass filter would be expected

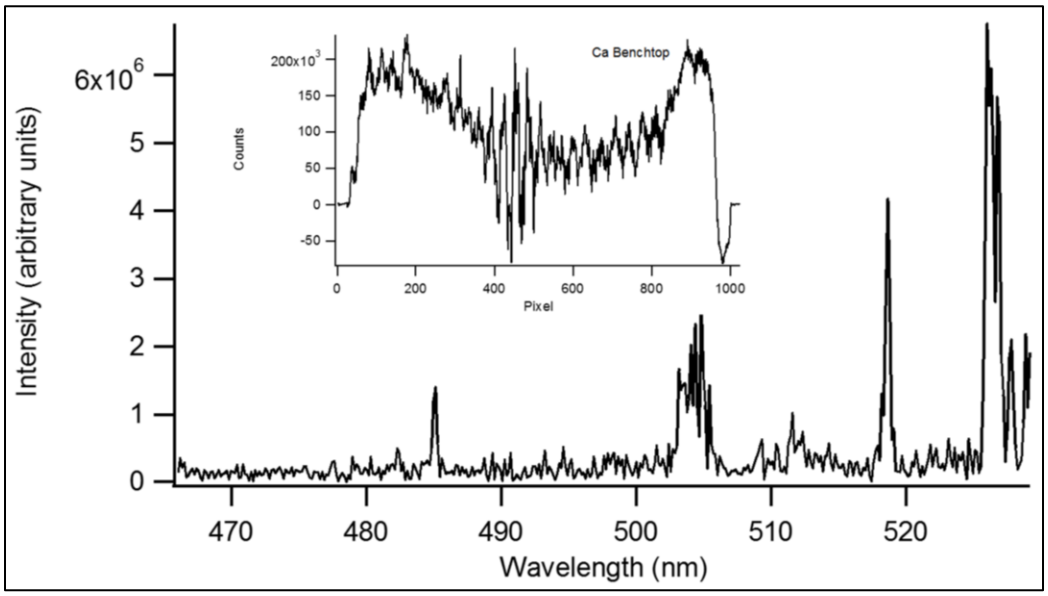

Figure 6.5: Benchtop spectrum of calcium metal by an accumulation of 500 LIBS sparks. Inset shows the interferogram cross-section. The gate delay was 2.3 μs, with a 2 μs gate width.

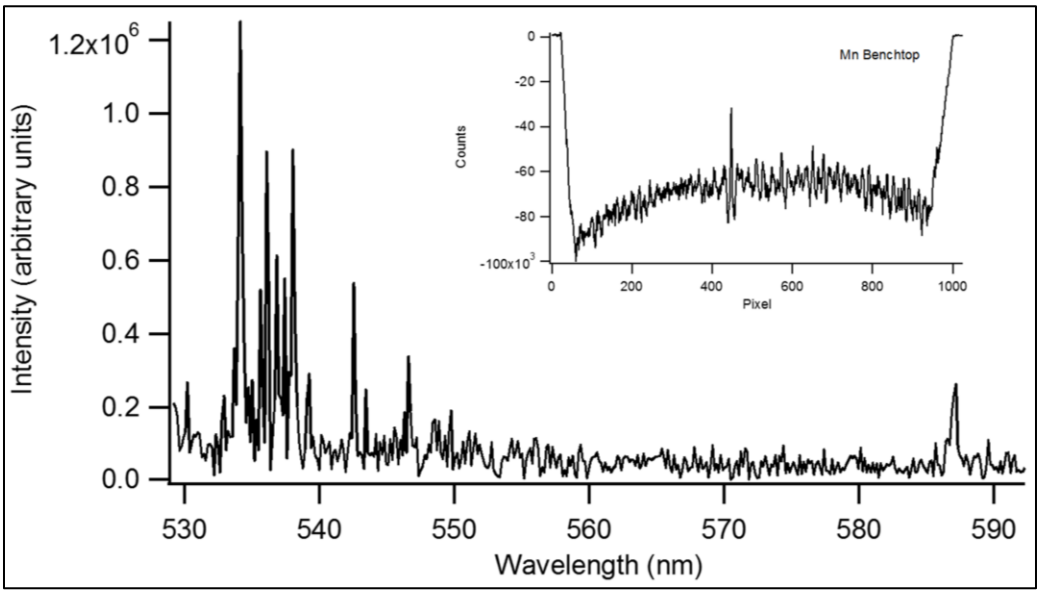

Figure 6.6: Benchtop spectrum of manganese metal by an accumulation of 500 LIBS sparks. Inset shows the interferogram cross-section. The gate delay was 0.6 μs with a 8 μs gate width.

to block the 515 nm line, so the identity of this line is not known. Similarly, the line that appears at ~ 597 nm appears to be a Mn I line in the ~ 467 to ~ 470 nm range as there is no Mn I line at ~ 597 nm.

The field of view for the SHS is the maximum acceptance angle for which the widest angle light does not produce an interferogram which differs from the interferogram produced by on-axis light by more than one fringe.[9] As shown above, without using any collection optics the acceptance angle of the SHLS is 1.8°, corresponding to a FOV at 4.5 m of ~ 140 mm. Thus, light originating from greater than ~ 0.9° on either side of the optical axis should degrade the quality of the interferogram. To test this, the FOV was measured by placing a 66 cm wide strip of Cu, 4.5 m from the front of the spectrometer with the center of the Cu strip aligned with the optical axis of the spectrometer. Spectra were collected in triplicate with the laser directed in random order to positions along the Cu strip. Figure 6.7 shows that the baseline-subtracted intensity of the 522 nm Cu line, plotted as a function of angle from the optical axis, is relatively constant within +/- one degree from the optical axis, then drops off quickly at larger angles. This result agrees well with the expected theoretical acceptance angle of the SHLS. The rapid decrease in intensity at angles greater than ~ 1° is because the light travels through the SHLS at such an extreme angle that part of the beam completely misses the ICCD. The relatively wide acceptance angle and large entrance aperture afforded by the SHLS design helps to alleviate many issues associated with stand-off LIBS measurements, namely relaxed laser pointing and alignment requirements. The fact that light can enter the system up to 1° off axis through a large aperture without detriment

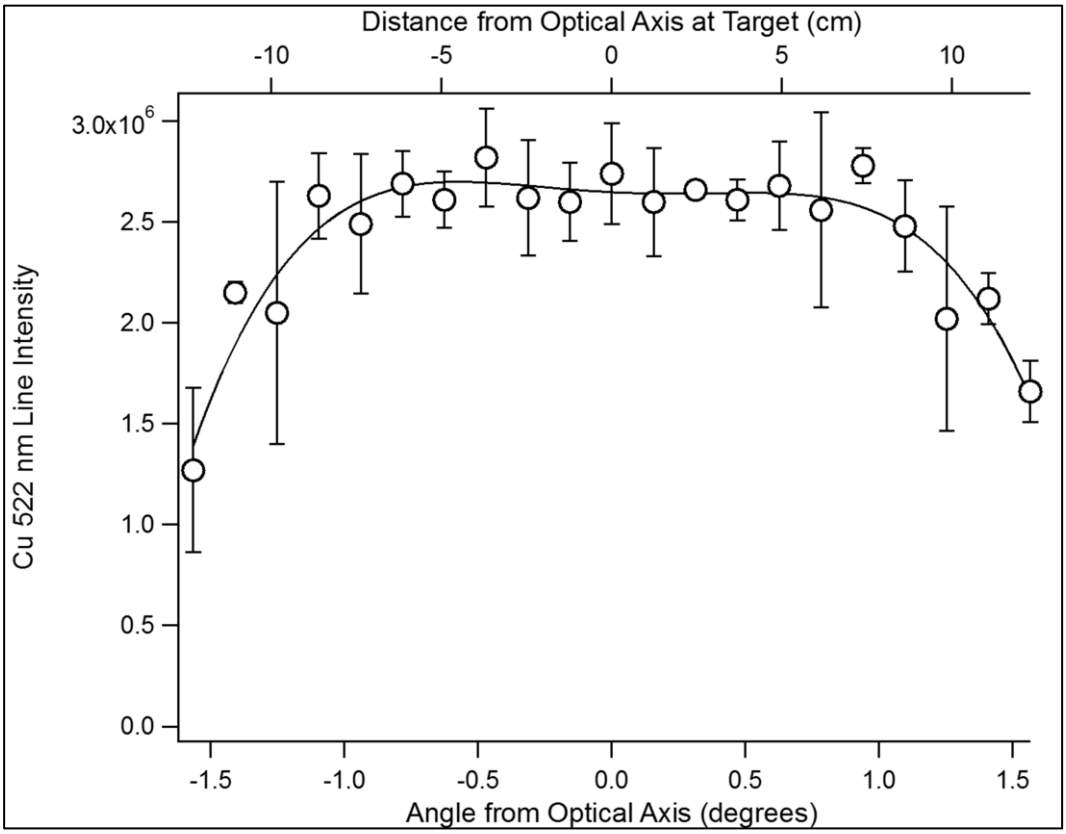

Figure 6.7: Field of view of the SHS was investigated by placing the samples 4.5m from the SHS at various distances perpendicular to the optical axis. Each position was repeated in triplicate. The 522 nm copper line intensity was baseline subtracted for each spectrum and averaged across replicates.

to the interferogram also allows for relaxed alignment requirements for coupling collection optics to the SHLS. This makes it relatively easy to introduce a telescope to improve light collection, since it is much easier to align to the large aperture of the SHLS than with the small slit on a common dispersive spectrometer.

For the 20 m standoff measurements, optimizing the laser focus was accomplished by monitoring the sound from the shock wave induced by the laser spark, with a microphone connected to an oscilloscope. Over certain regions of laser power we found that the LIBS spectral intensity and the intensity of the shock wave produced by the LIBS plasma are proportional to the laser irradiance impingent upon the sample. Figure 6.8 shows the microphone signal (dashed fit line) produced by forming a laser spark on a copper sample 20 m from the SHLS, as the focus of the laser was changed in small increments from approximately 1 m in front of the sample surface to approximately 1 m past the sample surface. The emission intensity of the 522 nm copper line (solid fit line) was also measured at each focal position, with the SHLS 20 m from the sample, using no collection optics other than the 10 mm diffraction grating. Both signals are plotted versus laser irradiance at the sample. The laser irradiance at the sample was calculated by measuring the laser power at the sample and estimating the laser spot size using laser burn paper, and measuring the diameter of the burn spot. The microphone focusing approach was simple and allowed optimal focusing at standoff distances to be achieved without approaching the sample. Figure 6.9 shows how the emission intensity and acoustic signals change as a function of the position of the laser focus, relative to the surface of the sample. As the focal point is brought closer to the surface of the sample both the microphone signal and the Cu emission intensity increase to a maximum and

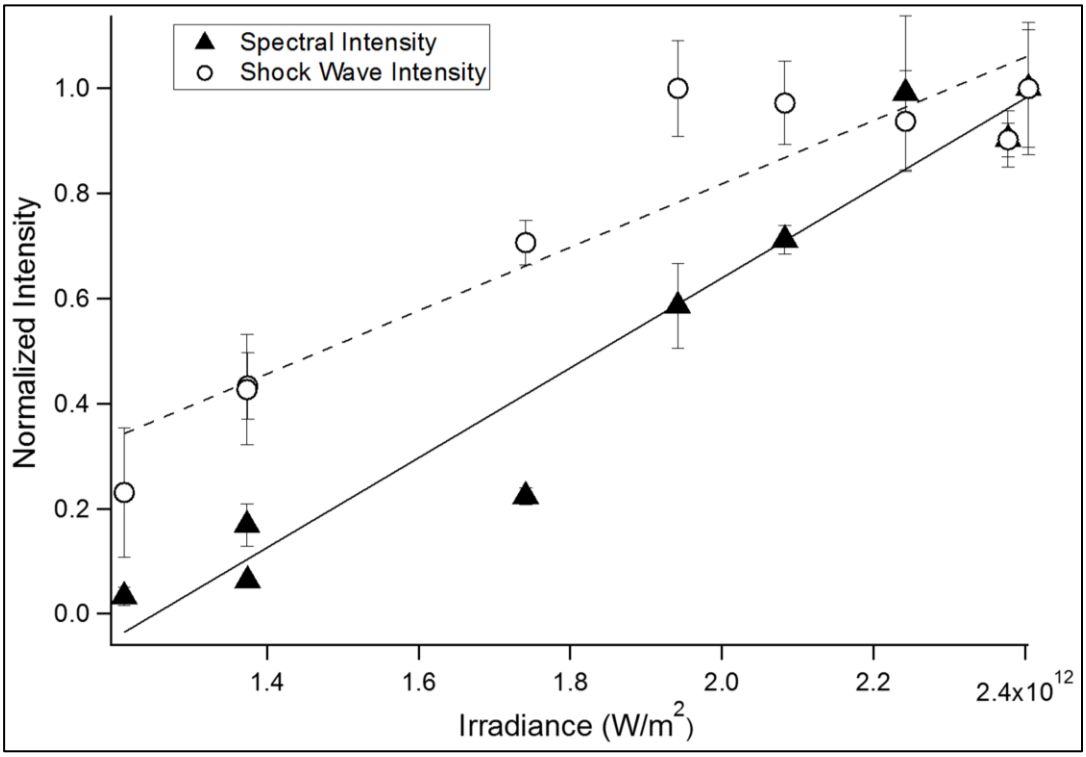

Figure 6.8: Shock wave and spectral intensity as a function of laser irradiance at the sample.

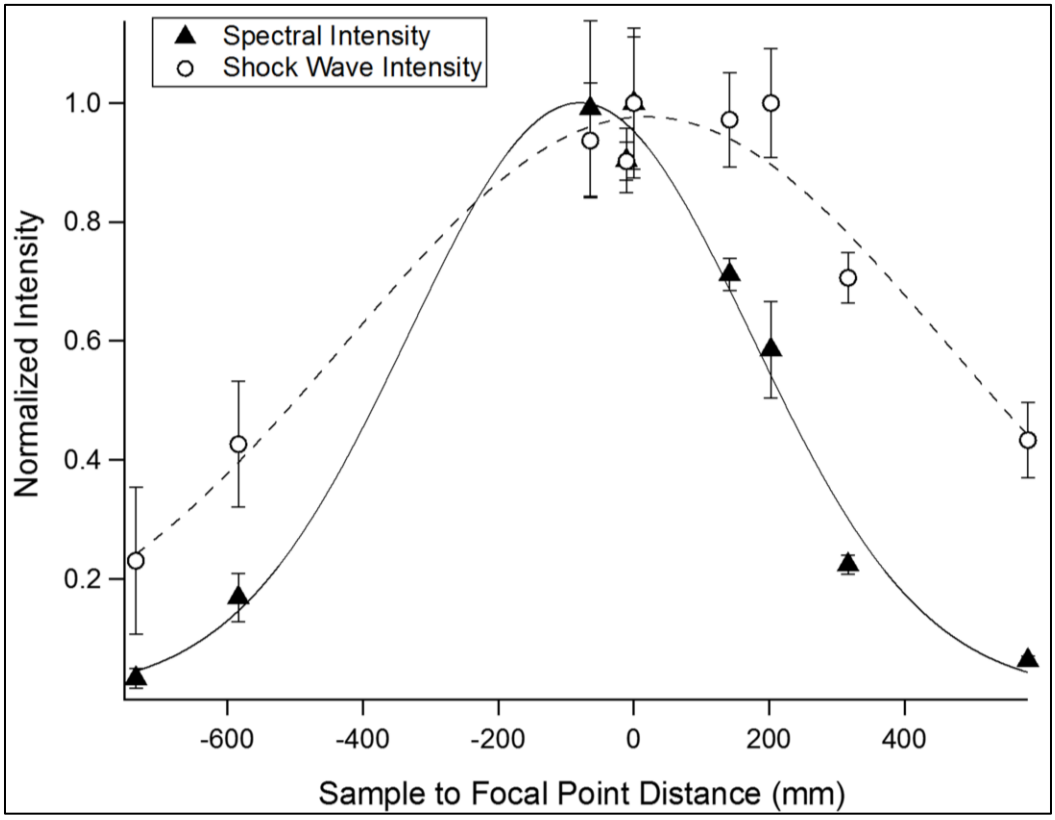

Figure 6.9: Plot of shock wave and spectral intensity as a function of focal point distance to sample surface. Negative values on the x-axis indicate that the focal point is between the SHS and the sample surface, while positive values indicate that the focal point is beyond the surface of the sample.

drop off as the focal point moves past the sample. Thus, monitoring the acoustic signal was found to be useful for optimizing the LIBS signal remotely.

The 40 m round-trip of the laser pulse from the laser to the sample, and the resulting LIBS emission returning to the SHS takes about 133 ns, an order of magnitude smaller than the gate delay used in the benchtop configuration. Thus the gate timing used in the benchtop measurements was also used for standoff measurements. However, because the signal was weaker, the number of summed laser shots was increased from 500 to 1000 and the gain of the detector was increased from 100 to 250. For the 20 m measurements the laser was focused to a ~ 1.2 mm diameter spot on the target using a beam expander.

Figure 6.10 shows LIBS spectra of Cu and Mg measured at 20 m with no collection optics other than the SHLS 10 mm gratings and beam splitter. The remarkable thing about these spectra is that you can measure the emission at all. The collection solid angle of the SHLS using 10 mm diffraction gratings and no collection optics, for samples at a 20 m sample distance is 0.2 μsr. Thus, the solid angle of collection was ~ 180 fold less than the benchtop measurements. The 515 and 522 Cu lines are clear in the top spectrum though the SNR is not high. In the case of Mg, the 516.7, 517.3, and 518.4 lines are clear, well above the noise level. The resolution is ~ 0.3 nm for all the lines shown.

The emission intensity for the Cu 522 nm line is only about 7 times less for the 20 m measurements ($1.7x10^6$) than for the 1.5 m distance, benchtop measurements ($1.2x10^7$). This may appear surprising given the ~ 180 fold reduction in collection efficiency at 20 m. For the 1.5 m measurements, the laser irradiance at the sample was

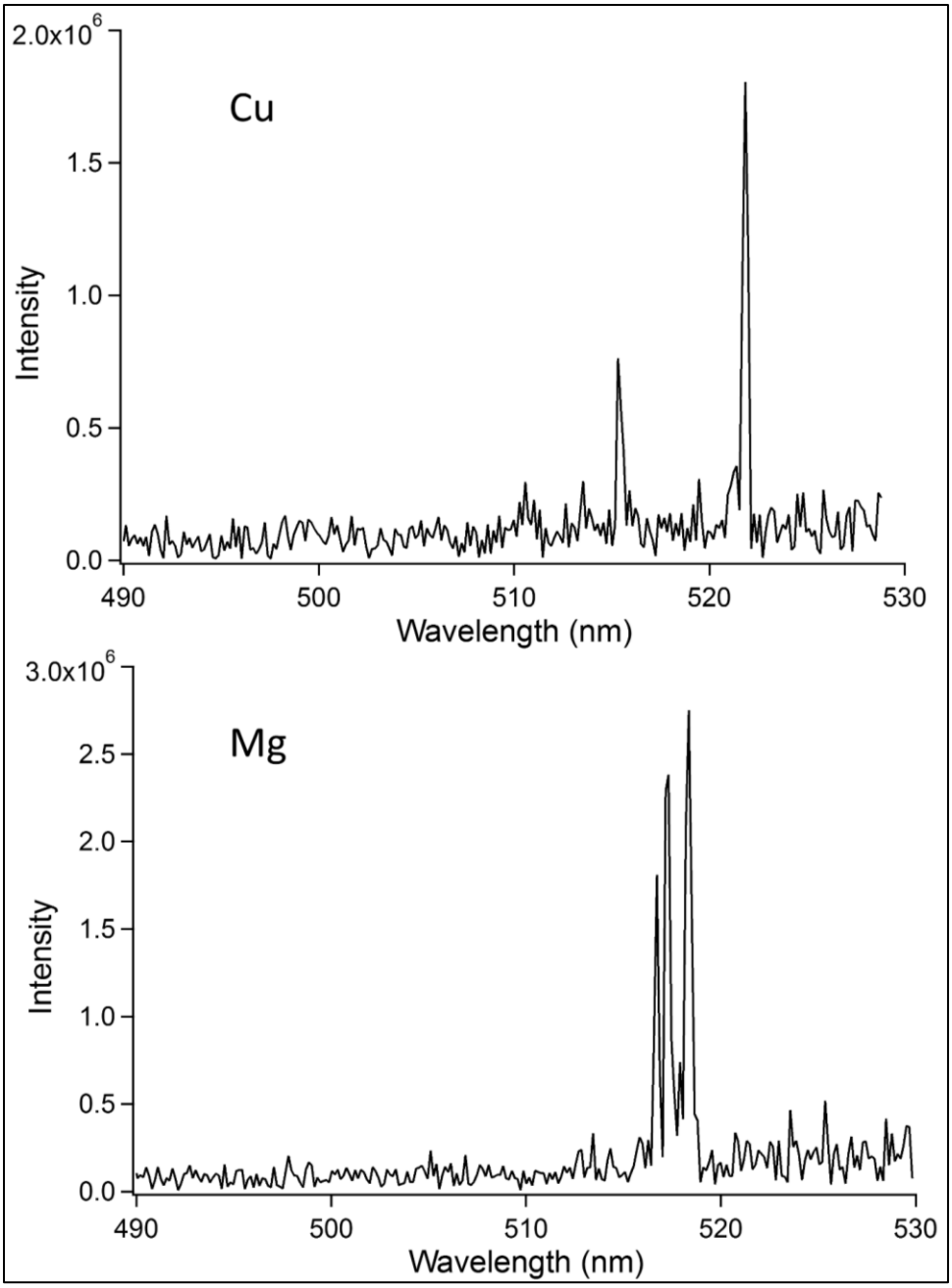

Figure 6.10: Standoff measurements with no collection optics other than the 10 mm diffraction gratings of copper metal (top) and magnesium metal (bottom). Each spectrum is an accumulation of 1000 LIBS sparks.

~ $4x10^{13}$ W m^{-2} and at 20 m the laser irradiance was ~ $1.2x10^{13}$ W m^{-2}. This should result in a further ~ 3 fold decrease in the LIBS emission if the LIBS emission scales as laser irradiance, though this is not necessarily always the case. However, the detector gain was increased from 100 at 1.5 m to 250 at 20 m, which, given the nonlinearity of ICCD gain, can explain the Cu 522 nm line intensity being greater than may initially be expected given the decrease in collection efficiency and laser irradiance at 20 m.

Although 20 m standoff measurements were demonstrated without the use of additional collection optics, realistically, collection optics are used for standoff measurements. A 127 mm diameter f/12.1 Schmidt-Cassegrain telescope was introduced on-axis with the SHS and a re-collimating lens used to direct a 10 mm diameter beam into the spectrometer. This increased the collection solid angle to ~ $5x10^{-5}$ sr, almost exactly the same as the benchtop measurements. Figure 6.11 shows LIBS spectra of Cu, Mg, Ca and Mn using this setup. For these measurements only 100 laser shots were accumulated for each spectrum and detector gain remained at 250. The 522 nm copper line intensity collected at 20 m standoff with 100 laser shots accumulated (Figure 6.11 top) was approximately 20% greater than the line intensity recovered in the benchtop configuration using 500 laser shots accumulated (Figure 6.3) due to the greater detector gain used for standoff configurations. The intensity for the 522 nm copper line using the telescope was ~ 8 times greater than the intensity measured using no collection optics (Figure 6.10 top), but consistent with the intensity of the benchtop measurements.

6.4 CONCLUSIONS

Standoff LIBS with the spatial heterodyne spectrometer has been demonstrated for the first time. The wide field of view of the SHS, shown to successfully recover

spectra with LIBS plasma deviating from the optical axis of the spectrometer by ~ 1°, and high throughput of the SHS allow LIBS spectra to be collected at distances up to 20 m with no collection optics. Monitoring the shock wave intensity of the LIBS plasma with a microphone and oscilloscope provided a convenient method to optimize laser focus at standoff distances without approaching the target. The addition of a small telescope for light collection increased the amount of signal light collected by an order of magnitude, even while accumulating 900 fewer laser shots per spectrum.

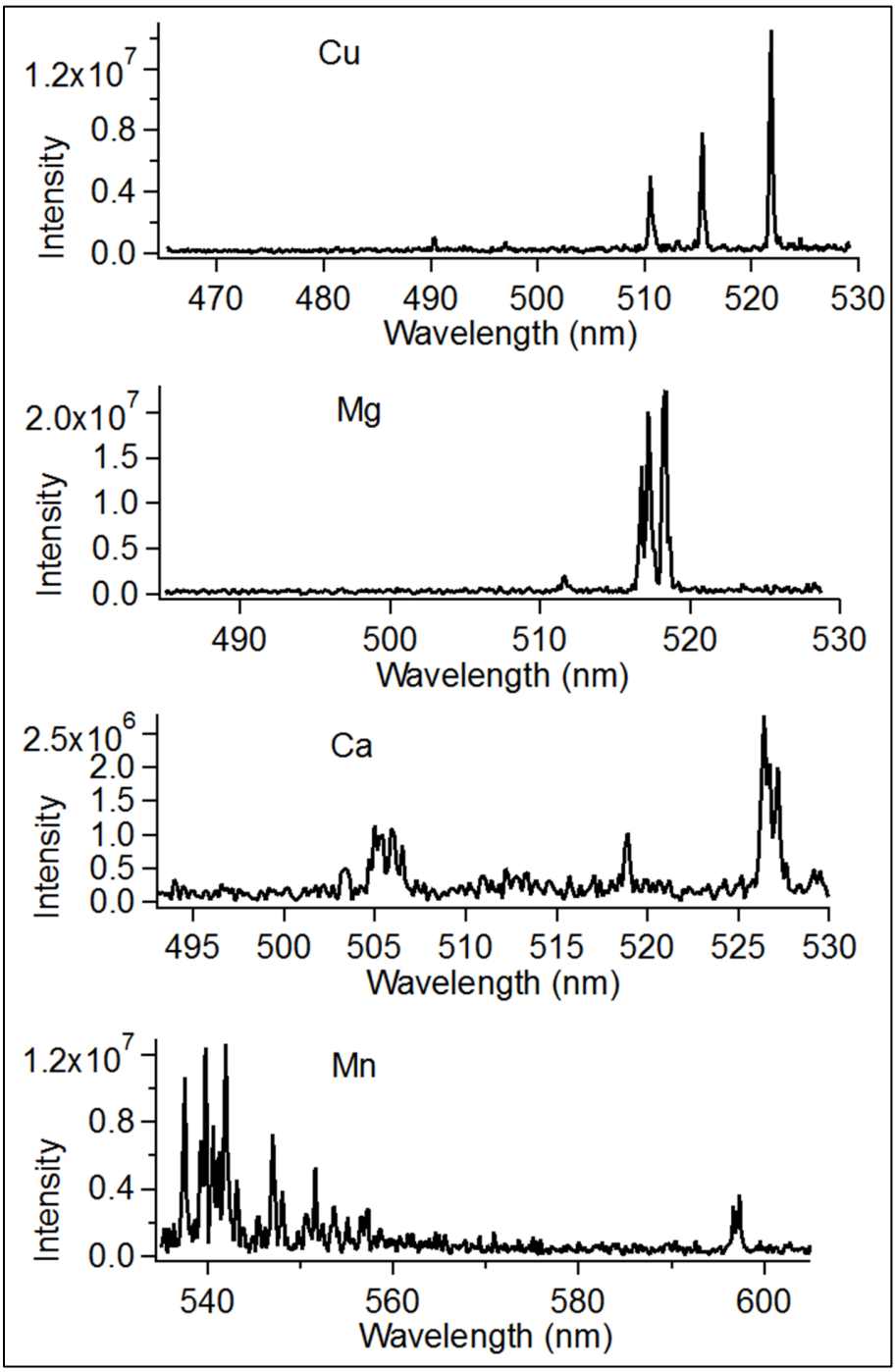

Figure 6.11: Standoff measurements with a 127mm Schmidt-Cassegrain telescope of various elements: upper most is copper metal, second from the top is magnesium metal, second from the bottom is calcium metal, and bottom most is manganese metal.

REFERENCES

(1) F. Brech, L. Cross. “Optical Microemission Stimulated by a Ruby MASER”. Appl. Spectrosc. 1962. 16: 59.

(2) J.R. Wachter, D.A. Cremers. “Determination of Uranium in Solution Using Laser-Induced Breakdown Spectroscopy”. Appl. Spectrosc. 1987. 41(6): 1042-1048.

(3) C.M. Davies, H.H. Telle, D.J. Montgomery, R.E. Corbett. “Quantitative analysis using remote laser-induced breakdown spectroscopy (LIBS)”. Spectrochim. Acta Part B. 1995. 50(9): 1059-1075.

(4) B.J. Marquardt, S.R. Goode, S.M. Angel. “In situ determination of lead in paint by laser-induced breakdown spectroscopy using a fiber-optic probe”. Anal. Chem. 1996. 68: 977-981.

(5) B.J. Marquardt, D.N. Stratis, D.A. Cremers, S.M. Angel. “Novel probe for laser-induced breakdown spectroscopy and Raman measurements using an imaging optical fiber”. Appl. Spectrosc. 1998. 52: 1148-1153.

(6) O. Samek, D.C.S. Beddows, J. Kaiser, S.V. Kukhlevsky, M. Liška, H.H. Telle, J. Young. “The application of laser induced breakdown spectroscopy to in situ analysis of liquid samples”. Opt. Eng. 2000. 39: 2248-2262.

(7) H.H. Telle, D.C.S. Beddows, G.W. Morris, O. Samek. “Sensitive and selective spectrochemical analysis of metallic samples: the combination of laser-induced breakdown spectroscopy and laser-induced fluorescence spectroscopy”. Spectrochim. Acta Part B. 2001. 56(6): 947-960.

(8) S. Palanco, J.M. Baena, J.J. Laserna. “Open-path laser-induced plasma spectrometry for remote analytical measurements on solid surfaces”. Spectrochim. Acta Part B. 2002. 57(3): 591-599.

(9) R.C. Wiens, S.K. Sharma, J. Thompson, A. Misra, P.G. Lucey. “Joint Analyses by Laser Induced Breakdown Spectroscopy (LIBS) and Raman Spectroscopy at Stand-Off Distances”. Spectrochim. Acta Part A. 2005. 61: 2324-2334.

(10) J.D. Blacic, D.R. Pettit, D.A. Cremers, N. Roessler. “Laser-Induced Breakdown Spectroscopy for Remote Elemental Analysis of Planetary Surfaces”. Proceedings of the International Symposium on Spectral Sensing Research. Maui, Hawaii, 15-20 November 1992.

(11) C.M. Davies, H.H. Telle, A.W. Williams. “Remote in situ analytical spectroscopy and its applications in the nuclear industry”. Fres. J. Anal. Chem. 1996. 355: 895-899.

(12) X.D. Hou, B.T. Jones. “Field instrumentation in atomic spectroscopy”. Microchem. J. 2000. 66: 115-145.

(13) A.K. Knight, N.L. Scherbarth, D.A. Cremers, M.J. Ferris. “Characterization of Laser-Induced Breakdown Spectroscopy (LIBS) for Application to Space Exploration”. Appl. Spectrosc. 2000. 54(3): 331-340.

(14) J. Gruber, J. Heitz, H. Strasser, D. Bäuerle, N. Ramaseder. “Rapid in-situ analysis of liquid steel by laser-induced breakdown spectroscopy”. Spectrochim. Acta Part B. 2001. 56(6): 685-693.

(15) A.I. Whitehouse, J. Young, I.M. Botheroyd, S. Lawson, C.P. Evans, J. Wright. “Remote material analysis of nuclear power station steam generator tubes by laser-induced breakdown spectroscopy”. Spectrochim. Acta Part B. 2001. 56(6): 821-830.

(16) Z.A. Arp, D.A. Cremers, R.D. Harris, D.M. Oschwald, G.R. Parker Jr., D.M. Wayne. “Feasibility of Generating a Useful Laser-Induced Breakdown Spectroscopy Plasma on Rocks at High Preassure: Preliminary Study for a Venus Mission”. Spectrochim. Acta Part B. 2004. 59: 987-999.

(17) C. López-Moreno, S. Palanco, J.J. Laserna. “Quantitative analysis of samples at high temperature with remote laser-induced breakdown spectrometry using a room-temperature calibration plot”. Spectrochim. Acta Part B. 2005. 60(7-8): 1034-1039.

(18) B. Sallé, J.L. Lacour, P. Mauchien, P. Fichet, S. Maurice, G. Manhés. “Comparative study of different methodologies for quantitative rock analysis by Laser-Induced Breakdown Spectroscopy in a simulated Martian atmosphere”. Spectrochim. Acta Part B. 2006. 61(3): 301-313.

(19) S. Palanco, C. López-Moreno, J.J. Laserna. “Design, construction and assessment of a field-deployable laser-induced breakdown spectrometer for remote elemental sensing”. Spectrochim. Acta Part B. 2006. 61(1): 88-95.

(20) C. López-Moreno, S. Palanco, J.J. Laserna, F. DeLucia Jr., A.W. Miziolek, J. Rose, R.A. Walters, A.I. Whitehouse. “Test of a stand-off laser-induced-breakdown spectroscopy sensor for the detection of explosive residues on solid surfaces”. J. Anal. At. Spectrom. 2006. 21: 55-60.

(21) R. González, P. Lucena, L.M. Tobaria, J.J. Laserna. “Standoff LIBS detection of explosive residues behind a barrier”. J. Anal. At. Spectrom. 2009. 24(8): 1123–1126.

(22) V. Lazic, A. Palucci, S. Jovicevic, M. Carapanese, C. Poggi, E. Buono. “Detection of explosives at trace levels by Laser Induced Breakdown

Spectroscopy (LIBS)". Chemical, Biological, Radiological, Nuclear, and Explosives (CBRNE) Sensing XI, vol. 7665 of Proceedings of SPIE, April 2010.

(23) S.K. Sharma, A.K. Misra, P.G. Lucey, R.C.F. Lentz. "A combined remote Raman and LIBS instrument for characterizing minerals with 532 nm laser excitation". Spectrochim. Acta, A. 2009. 73: 468-476.

(24) J. Moros, J.J. Laserna. "New Raman-Laser-Induced Breakdown Spectroscopy Identity of Explosives Using Parametric Data Fusion on an Integrated Sensing Platform". Anal. Chem. 83(16): 6275-6285.

(25) R. Grönlund, M. Lundqvist, S. Svanberg. "Remote imaging laser-induced breakdown spectroscopy and remote cultural heritage ablative cleaning". Opt. Lett. 2005. 30(21): 2882-2884.

(26) S.K. Sharma, A.K. Misra, P.G. Lucey, R.C. Wiens, S.M. Clegg. "Combined remote LIBS and Raman spectroscopy at 8.6 m of sulfur-containing minerals, and minerals coated with hematite or covered with basaltic dust". Spectrochim. Acta, A. 2007. 68(4): 1036-1045.

(27) J. Moros, J.A. Lorenzo, P. Lucena, L.M. Tobaria, J.J. Laserna. "Simultaneous Raman Spectroscopy-Laser-Induced Breakdown Spectroscopy for Instant Standoff Analysis of Explosives Using a Mobile Integrated Sensor Platform". Anal. Chem. 2010. 82: 1389–1400.

(28) J.M. Harlander. Spatial Heterodyne Spectroscopy: Interferometric Performance at Any Wavelength without Scanning. [Ph.D. Dissertation]. Madison, Wisconsin: University of Wisconsin-Madison, 1991.

(29) J.M. Harlander, F.L. Roesler, R.J. Reynolds, K. Jaehnig, W.A. Sanders. "Differential, Field-Widened Spatial Heterodyne Spectrometer for Investigations at High Spectral Resolution of the Diffuse Far Ultraviolet 1548 Å Emission Line from the Interstellar Medium". Proc. SPIE. 1993. 2006: 139-148.

(30) N.R. Gomer, C.M. Gordon, P. Lucey, S.K. Sharma, J.C. Carter, S.M. Angel. "Raman Spectroscopy Using a Spatial Heterodyne Spectrometer: Proof of Concept". Appl. Spectrosc. 2011. 65(8): 849–857.

(31) N. Lamsal, S.M. Angel. "Deep-Ultraviolet Raman Measurements Using a Spatial Heterodyne Raman Spectrometer (SHRS)". Appl. Spectrosc. 2015. 69(5): 525–534.

(32) N. Lamsal, S.M. Angel, S.K. Sharma, T.E. Acosta. "Visible and UV Standoff Raman Measurements in Ambient Light Conditions Using a Gated Spatial Heterodyne Raman Spectrometer". Paper presented at: LPSC 2015. Woodland TX; March 16-20.2015.

(33) N. Lamsal, S.K. Sharma, T.E. Acosta, S.M. Angel. “Stand-off UV and Visible Raman Measurements Using a Gated Spatial Heterodyne Raman Spectrometer”. Appl. Spectrosc. Paper in press 2016. DOI: 10.1177/0003702816631304.

(34) I.B. Gornushkin, B.W. Smith, U. Panne, N. Omenetto. “Laser-Induced Breakdown Spectroscopy Combined with Spatial Heterodyne Spectroscopy”. Appl. Spectrosc. 2014. 68(9): 1076-1084.

(35) J.M. Harlander, F.L. Roesler, S. Chakrabarti. “Spatial Heterodyne Spectroscopy: A Novel Interferometric Technique for the FUV”. In: O. H. W. Siegmund; H. S. Hudson, editors. EUV, X-Ray, and Gamma-Ray Instrumentation for Astronomy. Proc. SPIE. 1990. 1344: 120-131.

(36) A. Kramida, Y. Ralchenko, J. Reader, NIST ASD Team. “NIST Atomic Spectra Database (version 5.3).” National Institute of Standards and Technology, Gaithersburg, MD. http://physics.nist.gov/asd [accessed Feb 02 2016].